Graz University of Technology

20th International IGTE Symposium

on Computational Methods in Electrical Engineering and Multiphysics

IGTE '22

Proceedings

Sept. 18 - 21, 2022

Hotel Novapark, Graz, Austria

Alice Reinbacher-Köstinger (editor)

Institute for Fundamentals and Theory in Electrical Engineering

IGTE

The 20th International IGTE Symposium on Computational Methods in Electrical Engineering and Multiphysics was sponsored and supported by:

Imprint

Organisation: Christian Magele, Alice Reinbacher-Köstinger and Thomas Bauernfeind
Graz University of Technology, Institute of Fundamentals and Theory in
Electrical Engineering (IGTE)

Editor: Alice Reinbacher-Köstinger
Layout: Eniz Mušeljić
Cover: Alice Reinbacher-Köstinger

2025 Verlag der Technischen Universität Graz
www.tugraz-verlag.at

Proceedings of the 20th International IGTE Symposium on Computational Methods
in Electrical Engineering and Multiphysics, Graz, Novapark, 18-21.9.2022

ISBN (e-book): 978-3-85125-980-3
DOI: 10.3217/978-3-85125-980-3

List of Proceedings

Simulation of Permittivity and Conductivity Graded Materials for HVDC GIL for Different Voltage Forms

Hendrik Hensel, Christoph Jörgens and Markus Clemens
University of Wuppertal, Chair of Electromagnetic Theory, Rainer-Gruenter-Straße 21, 42119 Wuppertal, Germany

Abstract— **Functionally graded materials (FGM) are applied in HVDC gas insulated lines (GIL) to control the electric field within the DC insulation system. In HVDC GIL, FGM with a spatial distribution of the electric conductivity (σ-FGM) is applied to control the electric field under DC steady state condition. However, besides DC steady state, different DC conditions occur, e.g. DC-on process, polarity reversal and lightning impulse. Under these conditions σ-FGM is not sufficient to control the electric field, since these conditions result in transient capacitive fields, where the permittivity is decisive for the electric field. In this paper, we suggest combining σ-FGM and a spatial distribution of permittivity (ε-FGM) in the spacer material to control the electric field around DC-GIL spacer for various DC-conditions, considering nonlinear material models for the insulating gas and the epoxy spacer. A variation of the spatial distribution of permittivity and conductivity in the spacer is investigated in this paper for an effective field reduction. The results show a reduction of the electric field intensity up to 65.8 %, when σ/ε-FGM is applied.**

Index Terms—**electric conductivity, functionally graded materials (FGM), gas insulated lines (GIL), permittivity**

I. INTRODUCTION

High voltage direct current (HVDC) has become more relevant in recent years, since HVDC is the key technology to transmit electrical energy over long distances [1]. Due to the transition to renewable electric energy, electrical energy has to be transmitted e.g. from offshore windparks to urban areas, where space efficient devices are required, since space is limited. A possible solution are gas insulated systems, which use compressed gas to gain higher breakdown voltages, to scale down the dimension of the electrical device. Gas insulated transmission lines (GIL) are used to transmit electrical energy in a space efficient way. The insulating gas used is mainly sulfur hexalfluoride (SF_6), which is compressed to values in the order of 1-6 bar, to obtain a dielectric strength which is up to ten times higher compared to that of air [2]. Thus, GIL require considerably less space, compared to conventional transmission devices, e.g. overhead lines. However, electric field stress distributions may occur in GIL, which can lead to partial discharge or system failure. Especially the interfaces between the insulating gas and the massive insulators in GIL, the spacers between conductor and enclosure, are sensitive to electric field stress [3]. Functionally graded materials (FGM) are used as a technique to control the electric field stress. A spatial distribution of the electric conductivity (DC) or permittivity (AC) in the spacer (σ-FGM/ε-FGM) have been proposed in previous works to reduce the electric field stress within the GIL [4, 5, 11, 12, 13, 14, 15, 16]. The electric conductivity is decisive for the electric field under DC steady state condition. However, transient capacitive field stress, resulting from alternating current (AC), may also appear within HVDC GIL due to e.g. polarity reversal, lightning impulse or when DC voltage is turned on/off. Under these conditions, the permittivity ε of the insulating material is decisive for the electric field [5]. Hence, a combination of electric conductivity and permittivity (σ/ε-FGM) for HVDC GIL is investigated in this work, by numerical simulations. Following this introduction, the concept of σ/ε-FGM, the computation of the electric and thermal field and the nonlinear electric conductivity models of the insulating materials are presented in the next

section. The numerical simulation results for DC-on process, polarity reversal and lightning impulse with the application of σ/ε-FGM are given in section 3, followed by the conclusions in section 4.

II. APPROACH

A. *Concept of σ/ε-FGM*

The electric field within GIL consists of capacitive and resistive fields. Derived from Maxwell's equations, the electro-quasistatic complex amplitude of the potential φ is generally determined by

$$\nabla \cdot \left(\left(\varepsilon - j \frac{\sigma}{2\pi f} \right) \nabla \varphi \right) = 0, \tag{1}$$

where $\varepsilon = \varepsilon_0 \cdot \varepsilon_r$ is the permittivity, with the dielectric constant $\varepsilon_0 = 8{,}854 \cdot 10^{-12}$ As/Vm and the relative permittivtiy ε_r, σ the electric conductivity and f the frequency. Depending on the voltage condition, either the electric conductivity or the permittivity is decisive for the electric field. For DC (resistive) electric fields ($f = 0$ Hz) (1) can be converted to

$$\nabla \cdot (\sigma \nabla \varphi) = 0, \tag{2}$$

where the electric conductivity is dominant [6]. Under DC-operation condition, a slowly time varying electro-quasistatic field results in a GIL, due to space charge accumulation within the spacer and the insulating gas. The accumulation of charges causes an additional electric field, which adds to the externally applied electric field from the conductors [7]. For transient capacitive electric fields ($\varepsilon \gg \sigma/f$) the permittivity is dominant and (1) can be rewritten to

$$\nabla \cdot (\varepsilon \nabla \varphi) = 0. \tag{3}$$

However, under DC voltage capacitive and resistive fields both occur. During a DC voltage on process, the voltage level rises and results in a capacitive field, which is equivalent to the field under AC conditions. When the voltage level reaches a constant value, the slowly time varying electric fields results in a DC steady state condition, hence in a resistive field. This also occurs under

DC polarity reversal and when a lighting impulse appears under DC steady state [6]. These conditions are examined in this work, since under these conditions both ε-FGM and σ-FGM are required to control the electric field. The concept of FGM is to vary the permittivity and/or electric conductivity of the spacer material spatially [4, 5, 11, 12, 13, 14, 15, 16]. The areas where the spacer is under high electric fields have a higher value of permittivity/electric conductivity to reduce the electric field stress, compared to spacer parts, where high electric fields do not occur. The fabrication of FGM is realized by a controlled distribution of fillers in the spacer material, which mainly consists of epoxy resin. These fillers have a different value of permittivity/electric conductivity compared to epoxy resin to differentiate these parameters over space [3], [6].

B. *Nonlinear electric conductivity models*

Under DC operation condition, the electric conductivity depends on the temperature and the electric field [6]. The heat transfer in the spacer is given by heat conduction and for the gas it can be described by convective heat transfer and heat radiation. In actual operation, the current in the conductor leads to a temperature gradient between conductor and ground. Since fixed temperature gradients are defined in the simulations, it is sufficient to solve the stationary heat conduction equation [6], [8]

$$\nabla \cdot (\lambda \nabla T) + \kappa \left|\vec{\mathrm{E}}\right|^2 = 0. \qquad (4)$$

Here, T is the temperature, λ is the thermal conductivity and $\kappa\left|\vec{\mathrm{E}}\right|^2$ describes the heat sources in both insulation materials. Equation (1) and (4) are solved in a coupled simulation. For this, the electric conductivity needs to be determined precisely. In general, the electric conductivity of the epoxy resin material of the spacer, without considering FGM, has a nonlinear dependency on the temperature T and the electric field $\left|\vec{\mathrm{E}}\right|$, according to [4], [5], [6]. The equation to describe the electric conductivity of the spacer is given by

$$\kappa\left(T, \left|\vec{E}\right|\right) = \kappa_0 \exp\left(-\frac{W_A}{k_B T}\right) \exp\left(\vartheta\left|\vec{E}\right|\right), \qquad (5)$$

where $k_B = 8.617 \cdot 10^{-5}$ eV/K is the Boltzmann constant, $W_A = 0.095$ eV the activation energy and κ_0 and ϑ are constants [5], [6]. In most works the electric conductivity of the SF_6 is assumed to be constant. Here, the electric conductivity is described by a model to obtain precise simulation results, which is developed in [9]. According to [9], the electric conductivity of the SF_6 gas depends on the electric field $\left|\vec{\mathrm{E}}\right|$, the temperature T and the gas pressure P. The equation which describes the electric conductivity of SF_6 is given by

$$\kappa\left(\left|\vec{E}\right|, P, T\right) = \kappa_{\mathrm{SF6}} \cdot (\alpha + \beta \cdot (\gamma + \left|\vec{E}\right|/E_x)^{\varsigma}) \cdot (1/(\varrho + \epsilon \cdot \left|\vec{E}\right|/E_y)^{\iota}) \cdot \exp(\zeta \cdot P) \cdot \exp(\nu \cdot T), \qquad (6)$$

where κ_{SF6}, α, β, γ, E_x, ς, ϱ, ϵ, E_y, ι, ν and ζ are constants. The model allows to consider the effect different parameters have on the electric conductivity of the insulating gas, which would be neglected, if the electric conductivity was set constant.

III. ELECTRIC FIELD SIMULATION RESULTS WITH APPLIED σ/ε-FGM

The geometry model used for the simulations is a 2D model of an axisymmetric 320 kV DC GIL with a cone-type spacer and can be depicted in Figure 1. The temperature at the ground is set at 300 K. For all simulations in this work a temperature gradient of 40 K between conductor and ground is given, to consider the influence of the temperature on the electric conductivity of the insulators and the electric field within the GIL. The gas pressure is set at 0.6 MPa for all following results. The electric conductivity models (5) and (6) are each applied for the spacer and the SF_6 gas. The voltage distribution within the 320 kV GIL is shown in Figure 2.

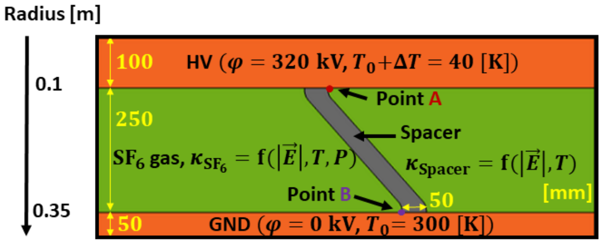

Figure 1: 2D axisymmetric geometry model of the GIL.

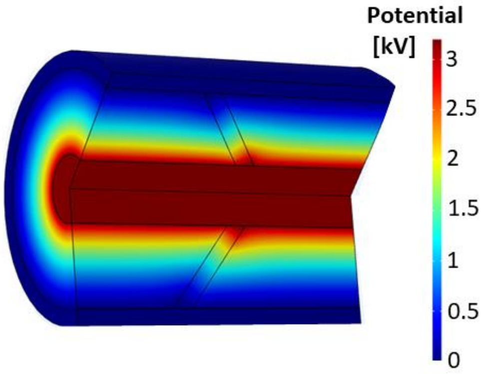

Figure 2: Potential distribution in the 320 kV GIL.

Three different DC conditions are investigated in this work: DC-on process, polarity reversal of the DC voltage and the appearance of a lightning impulse on a DC steady-state condition. Under these conditions both transient and DC fields occur and are hence convenient to investigate the benefit of σ/ε-FGM. In the following subchapters the simulation results for these conditions are presented.

A. *DC-on*

The DC-on process is performed by applying the 320 kV DC voltage at the conductor within 0.01 s switching time.

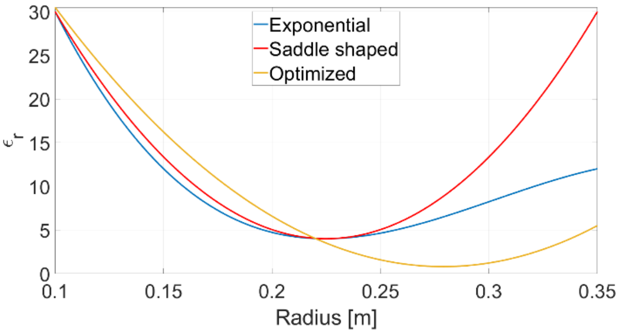

Figure 3: Three distributions of the permittivity in the spacer.

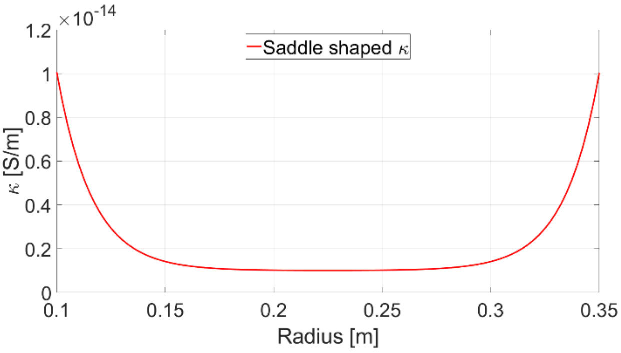

Figure 4: Distribution of the electric conductivity in the spacer.

To obtain the electric field over time, the analysis is executed by a time-domain simulation, until DC steady-state condition is reached. Three different distributions of the permittivity in the spacer material are investigated, as presented in Figure 3. These distributions are combined with a saddle shaped distribution of the electric conductivity in the spacer, depicted in Figure 4. The three different σ/ε-FGM approaches are applied on the spacer and the simulations results are compared with each other and with no application of σ/ε-FGM. Graded permittivity and electric conductivity are applied radially, which results in higher values of σ/ε at the electrodes, where the electric field stress appears.

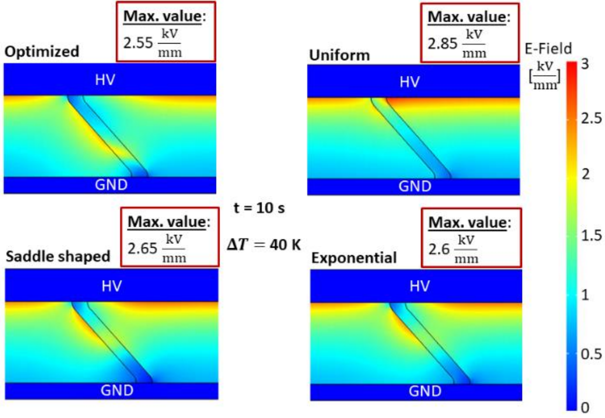

Figure 5: Distribution of the capacitive electric field under DC-on.

In Figure 5 the electric field distribution in the GIL is depicted, 10 s after the 320 kV are applied. Here, the transient capacitive field is shown with different electric field distributions, depending on the distribution of ε-FGM. In the case of a constant permittivity (uniform), an electric field peak occurs at the triple point between conductor, the insulating gas and the spacer. With the application of ε-FGM it can be seen that the electric field peak is relaxed for all different ε-FGM distributions. In case of ε-FGM, the maximum electric field is also lower, compared to the uniform case. The optimized ε distribution shows the lowest maximum electric field with 2.55 kV/mm, a reduction of 10.5 % compared to the maximum electric field of 2.85 kV/mm in the uniform case.

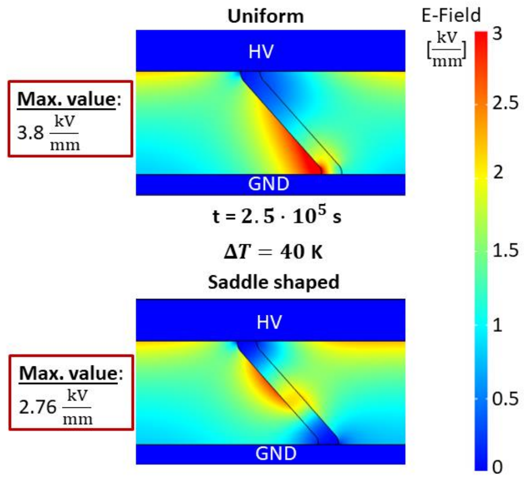

Figure 6: Distribution of the resistive electric field under DC-on.

Apart from the ε-FGM distributions, σ-FGM is also applied, which shows its effect after DC steady state is reached. In Figure 6 the electric field distribution is shown for t = $2.5 \cdot 10^5$ s for the uniform case and for one of the three cases where σ/ε-FGM is applied. The electric field distribution for DC steady state condition is the same in all three cases since the same electric conductivity (Figure 4) is applied. The electric field distribution in the uniform case is inversed due to the slow charge accumulation, which occurs under DC voltage. An electric field peak is seen at the triple point between the ground, the spacer and the insulating gas. With the application of σ-FGM the electric field inversion is prevented and in general is the electric field distribution relaxed. This can be also seen if the maximum electric field is examined. The maximum electric field in case of σ-FGM is 2.76 kV/mm, with a reduction of 27.3 % compared to the 3.8 kV/mm in the uniform case.

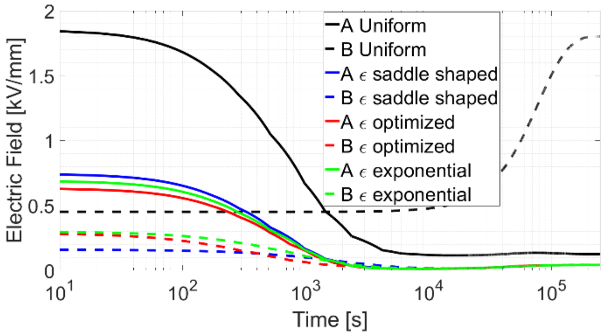

Figure 7: Electric field at the points A and B over time for different σ/ε-FGMs and a configuration without application of σ/ε-FGM (uniform).

For the illustration of the effect of a combined σ/ε-FGM, the electric field is depicted at the triple points A and B over time until DC steady state is reached, for the regarded cases in Figure 7. For all cases of application of σ/ε-FGM, during the whole process the electric field is lower at both points A (solid line) and B (dotted line) compared to the uniform spacer. Especially at point B, when DC steady state is reached, the electric field is considerably lower, since for the uniform spacer the electric field is getting inversed. Also at point A shortly after the application of the voltage the electric field is considerably higher in the uniform case. Figure 7 allows to compare the performance of the different σ/ε-FGM distributions. It can be seen that at point A the optimized ε-FGM shows the lowest electric field over time. At point B the optimized ε-FGM also indicates a very low electric field. Only for the first time period the saddle shaped ε-FGM shows a slightly lower electric field. It can be concluded that the optimized ε-FGM shows the best results. Hence, the optimized ε-FGM is used for further results and is compared to the uniform spacer.

B. Polarity Reversal

When under DC voltage the polarity gets reversed, the voltage is suddently changed, in this case from positive 320 kV to negative 320 kV in a very short switching time. Hence, both the permittivity and the electric conductivity are decisive for the electric field distribution in this process. According to (7), the electric field under polaritiy reversal $\left|\vec{E}_{\mathrm{PR}}\right|$ can be calculated by

$$\left|\vec{E}_{\mathrm{PR}}\right| = \left|2\cdot\left|\vec{E}_{\mathrm{AC}}\right| - \left|\vec{E}_{\mathrm{DC}}\right|\right|, \tag{7}$$

where $\vec{E}_{\mathrm{AC}}$ is the capacitive electric field under AC steady state and $\vec{E}_{\mathrm{DC}}$ is the resistive electric field under positive DC steady state [10]. The electric field distribution in the vicinity of the spacer at polarity reversal is depicted in Figure 8. The electric field is shown for a uniform spacer and for the σ/ε-FGM with the optimized permittivity distribution. In the uniform case it can be depicted that high electric field stress occurs at the triple point between spacer, gas and conductor. Compared to the σ/ε-FGM spacer, the electric field stress is highly reduced. The maximum electric field is 3.64 kV/mm and is 32.8 % reduced, compared to the maximum value of the uniform spacer, which is 5.43 kV/mm. The results indicate that the σ/ε-FGM field control technique is very useful to reduce the electric field distribution and to lower high electric field peaks, which occur under DC polarity reversal. Since both capacitive and resistive fields influence the electric field at polarity reversal, a combination of permittivity and electric conductivity FGM is necessary to control the electric field effectively.

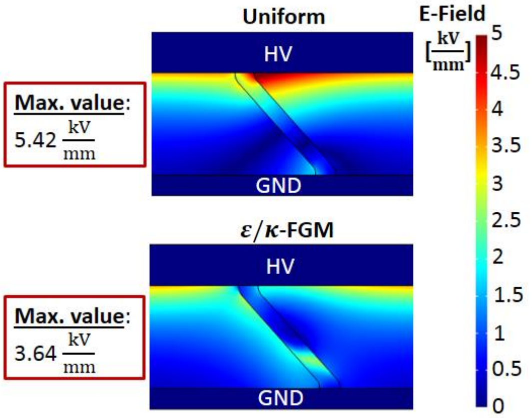

Figure 8: Electric field distribution at DC polarity reversal for a uniform spacer and a σ/ε-FGM spacer.

C. Lightning Impulse

The 1175 kV positive lightning impulse is superimposed on 320 kV DC steady state condition. The simulation is executed through a time-domain simulation. The standard lightning impulse has a front/tail time of 1.2/50 µs, which can be seen in Figure 9, where the voltage at the conductor is illustrated over time.

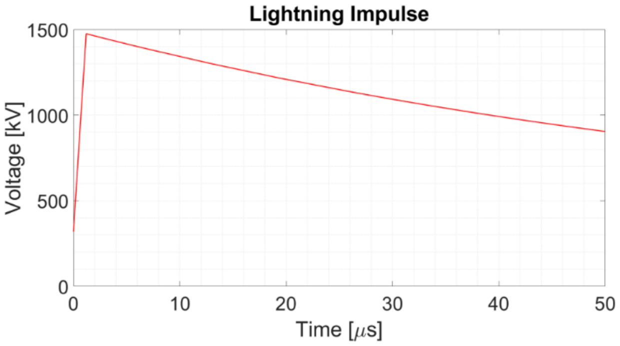

Figure 9: Superimposed 1175 kV lightning impulse on the 320 kV DC steady state.

Figure 10 shows the electric field over time after the lightning impulse was applied at point A and B for an uniform spacer and the σ/ε-FGM spacer. The electric field at point A is in case of the uniform spacer constantly higher, compared to the results for the σ/ε-FGM spacer. The electric field has its highest value right after the lightning impulse was applied, since the lightning impulse voltage decreases rapidly. The maximum value at point A for the uniform spacer is ca. 6.85 kV/mm. In terms of electric field stress, the σ/ε-FGM spacer performs clearly better. The maximum value for the σ/ε-FGM spacer is ca. 2.3 kV/mm, which is a reduction of 66.4 %, compared to the uniform case. The electric field at point B shows similar results, where the electric field is permanently lower when σ/ε-FGM is used. The maximum value of the electric field is 3.5 kV/mm and is decreased for the σ/ε-FGM spacer to 1.05 kV/mm, hence a reduction of 70 %. It can be concluded that the application of σ/ε-FGM highly reduces electric field stress under a lightning impulse.

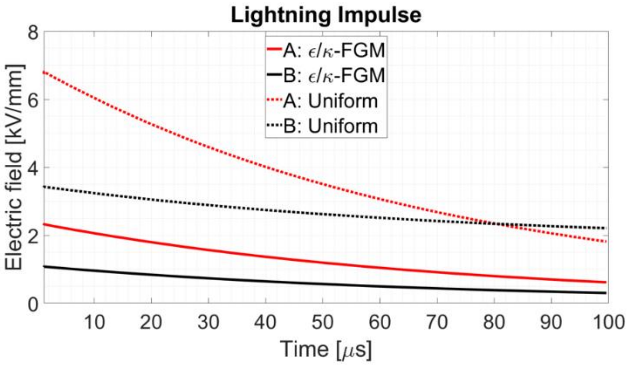

Figure 10: Electric field at point A and B for superimposed 1175 kV lightning impulse on the 320 kV DC steady state for a uniform spacer and a σ/ε-FGM spacer.

D. Discussion of Results

In DC-on process σ/ε-FGM proved a considerably reduced electric field intensity, especially at the triple points between gas, spacer and electrodes. The saddle shaped distribution of the electric conductivity and the optimized distribution of the permittivity in the spacer indicated the best results under the investigated distributions. The electric field stress at triple point A for the transient fields is with the application of σ/ε-FGM heavily reduced. When the electric fields develop into DC steady state, the uniform spacers shows a strongly inversed field, where the triple point B is intensely stressed. When σ/ε-FGM is applied, the inversion of the electric field is prevented, hence the electric field stress at the triple point B. Analog results are obtained for polarity reversal, where the maximum electric field within GIL is 32.8 %. When a lightning impulse overlaps with the operation DC voltage of the GIL, the GIL gets heavily stressed by the electric field, which the simulation results of the configuration without application of σ/ε-FGM show. The application of the optimized σ/ε-FGM spacer depicted excellent results, where the electric field at both sensitive triple points was considerably reduced up to 65.8 %.

IV. CONCLUSION

An investigation of a combination of permittivity and electric conductivity FGM in GIL for different DC conditions was performed using transient electro-quasistatic 2D field simulation. The distribution of σ/ε-FGM in the spacer was varied to find a suitable distribution to control the electric field intensity within the GIL. To obtain precise numerical results, models for the electric conductivity for the epoxy spacer and the SF_6 gas were applied. Examined were DC conditions such as DC-on process, polaritiy reversal and lightning impulse.

It can be concluded that a combination of σ/ε-FGM shows very good results terms of field control techniques and could reduce the electric field significantly.

REFERENCES

[1] A. Küchler, “High voltage engineering: Fundamentals, Technology, Applications”, 5^{th} ed., Springer-Verlag, Germany, 2018.

[2] J. Kindesberger, C. Lederle, “Surface charge decay on Insulators in air and sulfurhexalfluoride – Part I: Simulation”, IEEE Trans. Dielectr. Electr. Insul., Vol. 15, No. 4, 2008.

[3] N. Hayakawa, Y. Niyaji, H. Kojima, “Simulation on discharge inception voltage improvement of GIS spacer with permittivity graded materials (ε-FGM) using flexible mixture casting method”, IEEE Transactions on Dielectric and Electrical Insulation, Vol. 25, No. 4, 2018, pp. 1318-1323.

[4] C. Jörgens, H. Hensel, M. Clemens, „Modeling of the electric field in high voltage direct current gas insulated transmission lines“, International Conference on Dielectrics, 2022, submitted for publication.

[5] N. Hayakawa et al., “Electric field grading by functionally graded materials (FGM) for HVDC gas insulated power apparatus”, IEEE Conference on Electrical Insulation and Dielectric Phenomena, Cancun, Mexico, 2018.

[6] Rachmawati et al., „Electric field simulation of permittivity and conductivity graded materials (ε/κ-FGM) for HVDC GIS spacers“, IEEE Transactions on Dielectrics and Electrical Insulation, Vol. 28, No. 2, April 2022, pp. 736-744

[7] Y. Luo, et al., “Transition of the dominant charge accumulation mechanism at a Gas-solid interface under DC voltage” IET Gener. Transm. Distrib., Vol. 14, No. 15, pp. 3078-3088, 2020.

[8] H. Li, N. Zebouchi, and A. Haddad, “Theoretical and practical investigations of spacer models for future HVDC GIL/GIS applications,” Proc. 21st Int. Symp. High Voltage Engineering (ISH), Vol. 2, pp. 1538–1549, 2019.

[9] H. Hensel, C. Jörgens, M. Clemens, „Numerical simulation of electric field distribution in HVDC gas insulated lines considering a novel nonlinear conductivity model for SF6”, VDE Hochspannungstechnik, 2022, abstract accepted.

[10] R. Nakane et al., “Electrical insulation performance of HVDC-GIS spacer under various testing conditions”, IEEE Conf. Electr. Insul. Dielect. Phenom. (CEIDP), 2017, 7-6, pp. 621-624.

[11] R. N. Hayakawa et al., „Fabrication and simulation of permittivity graded materials for electric field grading of gas insulated power apparatus”, IEEE Transactions on Dielectric and Electrical Insulation, Vol. 23, No. 1, 2016, pp. 547-553.

[12] M. Kurimoto et al., “Application of functionally graded material for reducing electric field on electrode and spacer interface,” IEEE Transactions on Dielectric and Electrical Insulation, Vol.17, No.1, 2010, pp. 256-263.

[13] A. Al-Gheilani, Y. Li, K. L. Wong, W. S. T. Rowe, “Electric field reduction by multi-layer functionally graded material with controlled permittivity and conductivity distribution”, IEEE Conf. Electr. Insul. Dielect. Phenom., 2019, pp. 86-89.

[14] Z. Ran, “Electric field regulation of insulator interface by FGM with conductivity for superconducting-GIL”, IEEE Transactions on Applied Superconductivity, Vol. 29, No. 2, 2019.

[15] B. X. Du, Z. Y. Ran, J. Li, H. C. Liang, „Novel Insulator with interfacial σ-FGM for DC compact gaseous insulated pipeline“, IEEE Transactions on Dielectric and Electrical Insulation, Vol. 26, No. 3, 2019, pp. 818-825.

[16] B. X. Du, Z. Y. Ran, J. Li, H. C. Liang, H. Yao, „Fluorinated epoxy insulator with interfacial conductivity graded material for HVDC gaseous insulated pipeline“, IEEE Transactions on Dielectric and Electrical Insulation, Vol. 27, No. 4, 2020, pp. 1305-1312.

Sensitivity Analysis of Metamaterial-Inspired SIW Focusing on Resonator Misalignment

Stamatios Amanatiadis*, Vasileios Salonikios*, Michalis Nitas*, Theodoros Zygiridis†,
Nikolaos Kantartzis*, and Traianos Yioultsis*

*Dept. of Electrical & Computer Eng., Aristotle University of Thessaloniki, Thessaloniki, Greece
† Dept. of Electrical & Computer Eng., University of Western Macedonia, Kozani, Greece
E-mail: samanati@auth.gr

***Abstract*—The performance of the metamaterial-inspired substrate-integrated waveguide is discussed in this work, concerning a resonator misalignment potentially caused by the fabrication process. Initially, the design parameters of the aforementioned waveguide at the X-band are presented, while its optimal operation is validated to prove the effectiveness of the apparatus. Then, various significant aspects of the polynomial chaos expansion theory are briefly introduced to facilitate the sensitivity analysis due to fabrication errors. The direction of misalignment is, firstly, investigated, while the general case is, also, considered, highlighting a notable immunity, especially at lower frequencies. Additionally, a parametric examination is conducted in terms of the fabrication tolerance, measured as a percentage of the resonator unit cell. All the required simulations are conducted utilizing the non-intrusive approach of the polynomial chaos methodology via the popular Finite-Difference Time-Domain scheme.**

***Index Terms*—FDTD, planar waveguide, SRR, statistics.**

I. INTRODUCTION

The breakthrough of 5G communications requires the establishment of novel technologies, particularly in the millimeter-wave (mm-wave) regime. In particular, frequency augmentation leads to devices with finer geometrical characteristics; thus, the fabrication procedure becomes more challenging. Moreover, the material losses at this part of the spectrum are, also, increased and the appropriate design of transmission line systems is critical. Towards this aim, the substrate-integrated waveguide (SIW) concept has been proposed as a low-cost and easy-to-fabricate planar waveguiding apparatus [1]. It is composed of two dense series of metallic-coated via holes integrated into a conductor-covered substrate. Therefore, the propagating wave is successfully confined interior of the conductive via hole series. Essentially, the SIW shares various advantages of the conventional hollow metallic waveguides, such as the high Q-factor and power handling capability [2], [3]. At the same time, it enables the possibility to integrate various passive and active components at the mm-wave regime, such as couplers [4], dividers [5], filters [6] and antennas [7]–[9].

Despite the multiple advantages of the SIW, its fabrication can be cumbersome and costly, considering the drilling and the metallization injection for its large number of via holes. For this reason, a metamaterial-inspired extension to this technology has been introduced recently, where the via holes are replaced by a series of broadside-coupled complementary split-ring resonators (BC-CSRR) [10]. The operation of this waveguiding system, identified as BC-CSRR SIW, relies on the application of a virtual electric wall, in contrast to the conductive one of the conventional SIW, to confine the propagating wave. Consequently, this implementation facilitates the fabrication process, since only the appropriate imprinting of the resonators is required on both metallic sides of the substrate. Additionally, it retains the ability to integrate components into a single substrate-integrated platform. Specifically, several antenna configurations have been proposed such as a leaky-wave antenna with adjustable main-lobe angle [10], an H-plane sectoral-horn antenna [11] and a broadband bow-tie antenna [12].

Nevertheless, the proper alignment of the resonators is critical for the device's optimized functionality, since a misalignment may result in a weaker coupling between the CSRRs and the virtual electric wall. A preliminary analysis has been conducted in the original paper of the BC-CSRR SIW [10], where the misalignment towards the transverse, to the propagation, axis has been studied. Here, the transmission performance is extracted for a couple of misalignment absolute values, concluding that a reasonable degradation is observed, although a careful alignment should be guaranteed. However, a thorough sensitivity analysis is necessary for the immunity determination due to fabrication errors.

In this paper, this sensitivity analysis is performed via the extraction of the major statistical values, i.e., the mean value and the standard deviation, concerning the transmission coefficient for misaligned resonators. This is achieved utilizing the polynomial chaos (PC) expansion theory in a non-intrusive manner [13]. The latter ensures that a conventional deterministic solver is employed, particularly the Finite-Difference Time-Domain (FDTD) scheme. Moreover, the fabrication tolerance is expressed as a percentage of the unit cell, rather than an absolute value, to facilitate a generalized characterization.

II. MATERIALS AND METHODS

A. Design of the BC-CSRR SIW

The concept of the BC-CSRR has been described thoroughly in [10] and the setup includes two series of

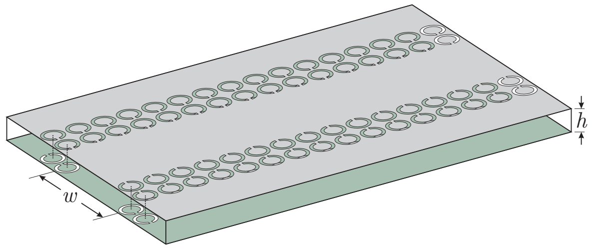

Fig. 1. The BC-CSRR SIW setup.

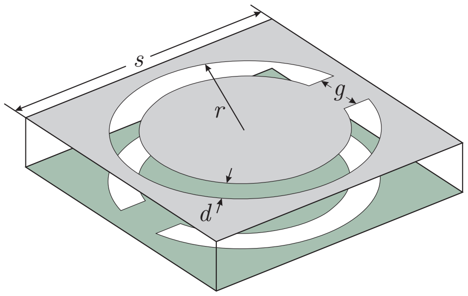

Fig. 2. The unit cell of the complementary split-ring resonator.

complementary resonators on both metallic sides of a substrate, as depicted in Fig. 1. The unit cell comprises two split-ring resonators etched on each side of the substrate, coupled via their broadside, as illustrated in Fig. 2. In this paper, the BC-CSRR SIW is designed for X-band operation, specifically from 8 to 11 GHz, with its optimal geometrical characteristics summarized in Table I. Note that the dielectric permittivity of the selected substrate is a typical $\varepsilon_r = 2.95$, while the loss tangent is $\tan\delta = 0.0018$. Moreover, a tapered microstrip line acts as the feeding network of our setup.

The functionality of the waveguide is validated through its transmission coefficient, sketched in Fig. 3. Here, the functionality of the device is exceptional at the desired frequency range, namely $8-11$ GHz, since the transmission mean value of the transmission is approximately -0.8 dB. Moreover, its value is maintained over -2 dB with an exception at 10.87 GHz where the lowest value of -2.2 dB is observed. The inset figure demonstrates the electric component that is normal to the propagation at 11 GHz. Interestingly, the desired virtual electric wall operates appropriately, since the electric field is well-confined inside the BC-CSRR SIW region.

TABLE I
OPTIMAL DIMENSIONS FOR THE BC-CSRR SIW AT THE X-BAND.

SIW width w [mm]	Substrate height h [mm]	Ring radius r [mm]	Ring width d [mm]	Ring gap g [mm]	Unit cell size s [mm]
13.5	1.5113	2.2	0.8	0.8	4.5

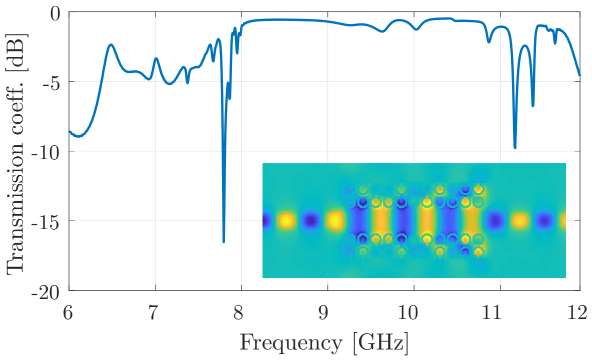

Fig. 3. Transmission coefficient of the BC-CSRR SIW at the X-band. The normal, to the substrate, electric component distribution at 11 GHz is illustrated in the inset.

B. Polynomial chaos expansion for sensitivity analysis

The most typical approach for sensitivity analysis in terms of small geometric fluctuations due to fabrication imperfections is the Monte Carlo scheme. Nevertheless, a large series of simulations are commonly required to acquire reliable statistical results, regarding the mean value and the standard deviation. For this reason, the polynomial chaos (PC) expansion methodology is launched in this paper [14], [15]. Explicitly, let us consider that the examined υ quantity depends on d independent random variables $\boldsymbol{\xi} = [\xi_1, \xi_2 \cdots \xi_d]$. The PC expansion is determined as

$$\upsilon(\boldsymbol{\xi}) = \sum_{l=0}^{P} c_l \Psi_l(\boldsymbol{\xi}), \tag{1}$$

for c_l the constant coefficients, $P+1$ the number of polynomial terms, defined by the desired polynomial order of expansion p and the selected truncation scheme, and $\Psi(\boldsymbol{\xi})$ the polynomial basis functions. The latter are constructed as:

$$\Psi_l(\boldsymbol{\xi}) = \prod_{i=1}^{d} \psi_{m_i^l}(\xi_i), \tag{2}$$

namely as products of univariate polynomials, where m_i^l is the i^{th} component of a multi-index that corresponds to l^{th} basis function. Moreover, the basis functions are selected appropriately bearing in mind the type of the random variable, e.g. Hermite polynomials for normal distribution as in our case. One significant property of the basis functions is their orthogonality, i.e.,

$$\langle \Psi_i(\boldsymbol{\xi}), \Psi_j(\boldsymbol{\xi}) \rangle = \begin{cases} 0, & i \neq j \\ \|\Psi_i(\boldsymbol{\xi})\|^2, & i = j \end{cases}, \tag{3}$$

with the inner product defined as

$$\langle x_1(\boldsymbol{\xi}), x_2(\boldsymbol{\xi}) \rangle = \int_{\Gamma} x_1(\boldsymbol{\xi}) x_2(\boldsymbol{\xi}) w(\boldsymbol{\xi}) \mathrm{d}\boldsymbol{\xi}, \tag{4}$$

and $w(\boldsymbol{\xi})$, Γ the probability function and the variable space, respectively. Then, the mean value and the standard deviation of υ are calculated via

$$E\{\upsilon\} = c_0, \quad \sigma\{\upsilon\} = \sqrt{\sum_{l=1}^{P} c_l^2 \|\Psi_l(\boldsymbol{\xi})\|^2}. \tag{5}$$

The task, now, is to calculate the unknown coefficients c_l. The non-intrusive nature of the approach we apply suggests that a conventional deterministic full-wave algorithm is multiply launched at specific samples of the random space. Next, the orthogonality of the basis functions is exploited and the unknown coefficients are, eventually, computed via the spectral projection of the quantity of interest υ on the polynomial functions, through

$$c_l = \frac{\langle y(\boldsymbol{\xi}), \Psi_l(\boldsymbol{\xi})\rangle}{\|\Psi_l(\boldsymbol{\xi})\|^2}, \tag{6}$$

where all numerical integrations are evaluated via the Gauss-Hermite quadrature technique

C. Details of the FDTD deterministic solver

All the numerical results in this paper are extracted via the efficient FDTD method. Note that the conventional staircase algorithm is enhanced via the numerically stable conformal modeling technique of [16] to accurately design the curved metallic regions of the resonators. The size of the computational domain for y the propagation axis and z the normal to the substrate is $40 \times 100 \times 20\,\text{mm}^3$ and it is divided into approximately $120 \times 330 \times 50$ mesh-cells, depending on the misalignment. The time-step is selected at $47.7\,\text{ps}$ to ensure the simulation stability, while a broadband pulse excitation is utilized at the frequency range $6 - 12\,\text{GHz}$. Finally, the open boundaries are truncated via an 8-cell thick Perfectly Matched Layer to effectively absorb the outgoing waves.

The polynomial expansion order for each univariate basis function is selected $p = 8$ for our sensitivity analysis. This requires a total of 5 or 25 deterministic simulations for misalignment investigation towards one or both directions, respectively. Note that the symmetry of the arrangement is exploited efficiently to reduce the total number of simulations. Finally, the transmission coefficient at the entire frequency range is set as the main value of interest υ. However, the electric field distribution at 11 GHz is, also, selected as a secondary value of interest to examine the electromagnetic effect on the propagation due to the misalignment.

III. RESULTS AND DISCUSSION

The statistical analysis is conducted concerning a specific tolerance level of the fabrication. In this work, this is defined as a percentage of the unit cell size, while the normal distribution is considered the most realistic approach. Consequently, the tolerance limits are determined via the values with a probability of 99.7 %, namely the $\pm 3\sigma$ of the normal density function. Moreover, the statistical results include the mean value and the three levels of the computed standard deviation, i.e. 1σ, 2σ, and 3σ, to provide a stronger perception of device functionality. Note that the closer the standard deviation levels to the mean value, the lower the influence of the misalignment.

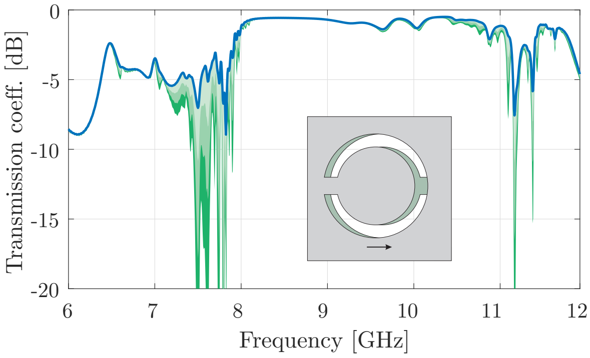

Fig. 4. Sensitivity analysis for misalignment towards the transverse, to the propagation, axis with 10 % fabrication tolerance.

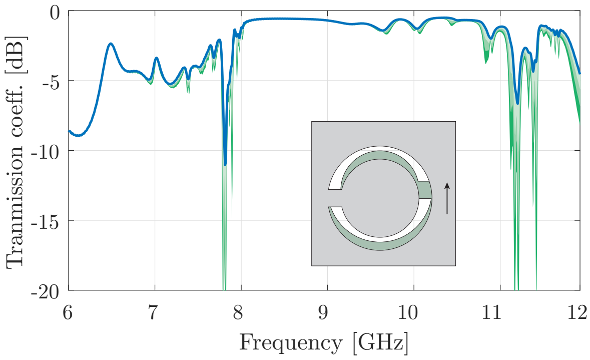

Fig. 5. Sensitivity analysis for misalignment towards the propagation axis with 10 % fabrication tolerance.

A. Statistical results for 10 % tolerance

Initially, the fabrication tolerance is set to 10 % of the unit cell, namely $3\sigma = 0.45\,\text{mm}$, and the effect towards one dimension is examined. Let us consider the fluctuation towards the transverse, to the propagation axis, direction, where the parametric analysis of [10] is available. Our results, in Fig. 4, lead to a similar remark that the BC-CSRR SIW is very stable within the desired frequency range for this moderate tolerance. In particular, the level of the transmission coefficient's mean value is at $-0.81\,\text{dB}$, while the lowest observation for the 3σ level, with probability 99.7 %, is $-2.7\,\text{dB}$ at 10.9 GHz.

The statistical results for the misalignment towards the

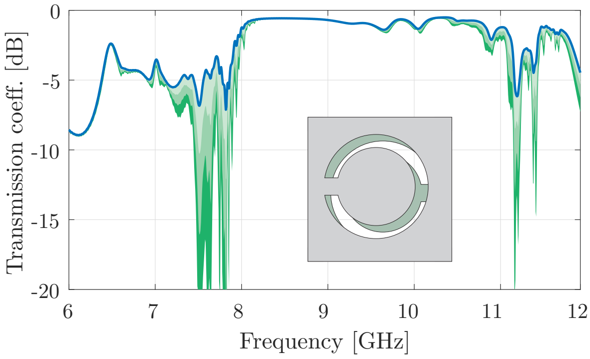

Fig. 6. Sensitivity analysis for the general case of misalignment with 10 % fabrication tolerance.

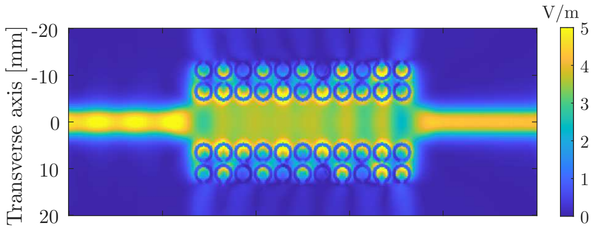

(a) Mean value

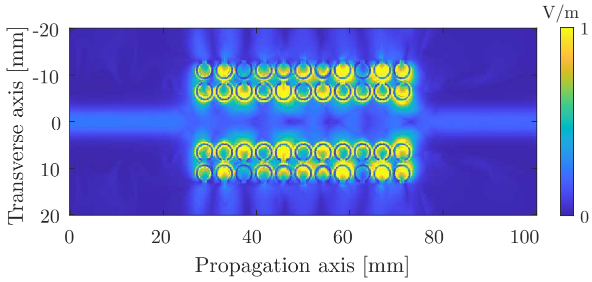

(b) Standard deviation

Fig. 7. Statistics of the normal, to the substrate, electric component at 11 GHz considering 10 % tolerance.

propagation axis are depicted in Fig. 5, where a similar behavior is noticed, since the mean value is almost identical at $8-11$ GHz range. Nevertheless, near 11 GHz a somewhat increased degradation is highlighted since the 3σ value falls to -3.8 dB at 10.8 GHz. Consequently, more attention should be drawn to the alignment towards the propagation axis direction.

Finally, we study the general case of misalignment, and the results are sketched in Fig. 6. Here, the remarkable stability of the BC-CSRR SIW for 10 % fabrication tolerance is highlighted, especially at the $8-10.4$ GHz range, where the 3σ level has an effect of less than 0.4 dB. However, near 11 GHz, particularly at 10.9 GHz, the misalignment can degrade the performance of the waveguide up to the reasonable -3.3 dB. Note that although the strongest fluctuations appear at lower frequencies, this effect is eliminated beyond 8 GHz for all the examined arrangements.

The statistics of the electric field at 11 GHz are also considered as an auxiliary investigation of the electromagnetic aspects of the waveguiding characteristics. Note that we select the frequency at the upper limit of the BC-CSRR SIW operational range since the misalignment effect is mainly located there. The mean value and the standard deviation of the normal, to the substrate, component are extracted and illustrated in Fig. 7 for 10 % fabrication tolerance. An interesting observation is that standing waves emerge due to the mismatch of the misaligned waveguide with the feeding network. Moreover, a moderate field leakage is, also, noticed since the weaker coupling of the misaligned resonators leads to the degradation of the desired virtual electric wall. Consequently, the transmission coefficient reduction near the upper limit is totally rational. Furthermore, the standard deviation indicates strong fluctuations at the resonators' region, as expected due to their misalignment. At the same time, both the input and the output of the tapered microstrip transmission line are affected at a lower level.

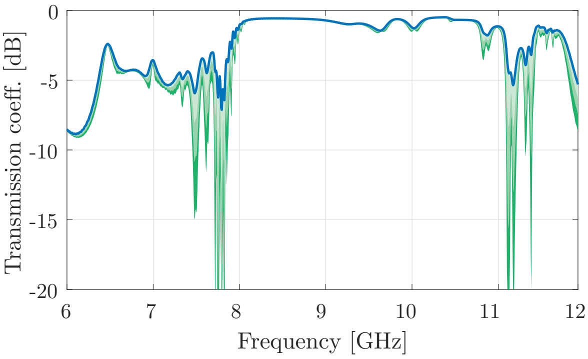

Fig. 8. Sensitivity analysis for the general case of misalignment with 5 % fabrication tolerance.

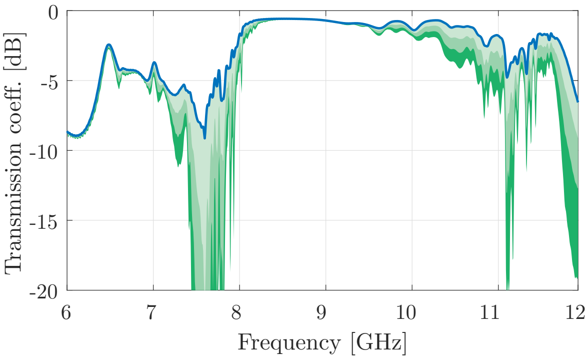

Fig. 9. Sensitivity analysis for the general case of misalignment with 20 % fabrication tolerance.

B. *Parametric analysis of tolerance*

The previous analysis highlighted that the moderate 10 % fabrication tolerance does not degrade significantly the performance of the BC-CSRR SIW. Now, two different tolerance values are, also, examined to investigate the fluctuations parametrically. Initially, a finer fabrication procedure is considered with a tolerance of 5 % and the statistical results demonstrated in Fig. 8. As a first observation, the misalignment effect seems weaker since the 3σ level is generally close to the mean value, as expected by the decreased tolerance. However, focusing on the waveguiding frequency range, i.e., $8-11$ GHz, the results are almost identical to Fig. 6. In particular, the deviation from the mean value is less than 0.4 dB from 8 GHz to 10.7 GHz, while the worst case is observed at 10.8 GHz with a -3.4 dB value for the 3σ level.

Moreover, a coarser fabrication process is investigated using a tolerance value of 20 %, while the statistics of the transmission coefficient are depicted in Fig. 9. The degradation is, now, obvious since both the mean value level is decreased to approximately -1 dB and the 3σ level is significantly dropped near the upper limit. Specifically, the stronger fluctuation is observed at

10.8 GHz with the lowest value the undesired -7.8 dB. Nevertheless, the deviation at the lower waveguiding range, namely $8-10$ GHz, is less than -0.5 dB indicating further the impressive stability of the BC-CSRR SIW even for the 20 % tolerance value. Indeed, a careful fabrication process is required to avoid degradation at the upper-frequency limit of the waveguide.

IV. CONCLUSION

The sensitivity of the BC-CSRR SIW has been examined in this paper in terms of the resonator misalignment due to fabrication imperfections. The concept of the metamaterial-inspired SIW has been presented as well as the non-intrusive polynomial chaos expansion methodology for efficient statistical study. The sensitivity analysis has been conducted for different misalignment types and tolerance values, while the FDTD scheme has been employed for the numerical result extraction, including, mainly, the transmission coefficient of the BC-CSRR SIW. The statistics proved the exceptional stability of the waveguide at its lower operational range and a potential degradation, especially for a coarse fabrication process.

ACKNOWLEDGEMENT

The research project was supported by the Hellenic Foundation for Research and Innovation (H.F.R.I.) under the “2nd Call for H.F.R.I. Research Projects to support Post-Doctoral Researchers” (Project Number: 756).

H.F.R.I.
Hellenic Foundation for
Research & Innovation

REFERENCES

[1] D. Deslandes and K. Wu, “Accurate modeling, wave mechanisms, and design considerations of a substrate integrated waveguide,” *IEEE Transactions on Microwave Theory and Techniques*, vol. 54, no. 6, pp. 2516–2526, 2006.

[2] F. Xu and K. Wu, “Guided-wave and leakage characteristics of substrate integrated waveguide,” *IEEE Transactions on Microwave Theory and Techniques*, vol. 53, no. 1, pp. 66–73, 2005.

[3] M. Bozzi, L. Perregrini, and K. Wu, “Modeling of conductor, dielectric, and radiation losses in substrate integrated waveguide by the boundary integral-resonant mode expansion method,” *IEEE Transactions on Microwave Theory and Techniques*, vol. 56, no. 12, pp. 3153–3161, 2008.

[4] X. F. Ye, S. Y. Zheng, and Y. M. Pan, “A compact millimeter-wave patch quadrature coupler with a wide range of coupling coefficients,” *IEEE Microwave and Wireless Components Letters*, vol. 26, no. 3, pp. 165–167, 2016.

[5] A. A. Khan and M. K. Mandal, “Miniaturized substrate integrated waveguide (SIW) power dividers,” *IEEE Microwave and Wireless Components Letters*, vol. 26, no. 11, pp. 888–890, 2016.

[6] S. Moscato, C. Tomassoni, M. Bozzi, and L. Perregrini, “Quarter-mode cavity filters in substrate integrated waveguide technology,” *IEEE Transactions on Microwave Theory and Techniques*, vol. 64, no. 8, pp. 2538–2547, 2016.

[7] M. Bozzi, A. Georgiadis, and K. Wu, “Review of substrate-integrated waveguide circuits and antennas,” *IET Microwaves, Antennas & Propagation*, vol. 5, no. 8, pp. 909–920, 2011.

[8] S. Mukherjee and A. Biswas, “Design of self-diplexing substrate integrated waveguide cavity-backed slot antenna,” *IEEE Antennas and Wireless Propagation Letters*, vol. 15, pp. 1775–1778, 2016.

[9] Q. Zhu, K. B. Ng, C. H. Chan, and K.-M. Luk, “Substrate-integrated-waveguide-fed array antenna covering 57–71 GHz band for 5G applications,” *IEEE Transactions on Antennas and Propagation*, vol. 65, no. 12, pp. 6298–6306, 2017.

[10] M. Nitas, M.-T. Passia, and T. V. Yioultsis, “Fully planar slow-wave substrate integrated waveguide based on broadside-coupled complementary split ring resonators for mmwave and 5G components,” *IET Microwaves, Antennas & Propagation*, vol. 14, no. 10, pp. 1096–1107, 2020.

[11] V. Salonikios, M. Nitas, S. Raptis, and T. V. Yioultsis, “Design of a fully planar BC-CSRR SIW-based H-plane sectoral horn with a printed transition,” in *2019 13th European Conference on Antennas and Propagation (EuCAP)*. IEEE, 2019, pp. 1–5.

[12] C. Feng, T. Shi, and L. Wang, “Novel broadband bow-tie antenna based on complementary split-ring resonators enhanced substrate-integrated waveguide,” *IEEE Access*, vol. 7, pp. 12 397–12 404, 2019.

[13] T. Crestaux, O. Le Maıtre, and J.-M. Martinez, “Polynomial chaos expansion for sensitivity analysis,” *Reliability Engineering & System Safety*, vol. 94, no. 7, pp. 1161–1172, 2009.

[14] D. Xiu and G. E. Karniadakis, “The wiener–askey polynomial chaos for stochastic differential equations,” *SIAM Journal on Scientific Computing*, vol. 24, no. 2, pp. 619–644, 2002.

[15] T. T. Zygiridis, “A short review of fdtd-based methods for uncertainty quantification in computational electromagnetics,” *Mathematical Problems in Engineering*, vol. 2017, 2017.

[16] S. Dey and R. Mittra, “A modified locally conformal finite-difference time-domain algorithm for modeling three-dimensional perfectly conducting objects,” *Microwave and Optical Technology Letters*, vol. 17, no. 6, pp. 349–352, 1998.

Non linear lumped parameter modelling of electro-thermal systems based on 3D-FEA

E. Spateri*, F. Ruiz* , G. Gruosso*

* Politecnico di Milano, Dipartimento di elettronica, informazione e bioingegneria, Piazza Leonardo da Vinci, 20133, Milano, Italy
E-mail: enrico.spateri@polimi.it, fredy.ruiz@polimi.it, giambattista.gruosso@polimi.it

***Abstract*—This article introduces the methodology for the extraction of equivalent nonlinear circuital lumped parameters based on a 3D FEM analysis for induction heating systems. An electromagnetic-thermal coupled case study for manufacturing purposes is analysed, and the necessary quantities for the description of equivalent circuit are extracted, interpolated and exploited for the converter simulation with nonlinear loads depending on the supplied current and frequency and the temperature of the workpiece. The behaviour of the coil-workpiece coupling, resulting in the series equivalent parameters, is compared to the measurements over a specimen of the accounted material for different temperatures. Moreover, the behaviour of the parameters is tracked in a coupled converter simulation.**

***Index Terms*—Lumped parameter modelling, Finite element method, Induction heating, Multiphysics coupling.**

INTRODUCTION

Induction heating (IH) systems are faster, more efficient, sustainable and cleaner than standard heating techniques.Starting from cookers, to welding, to crack detection thermography, the IH is emerging as a valid alternative to combustion heating. Due to the electromagnetic behaviour, the IH systems have a natural drawback: its highly dependent on the material parameters, the geometric parameters as coil-workpiece distance or workpiece defects, the time derivative of the magnetic flux, the skin depth of the induced field inside the ferromagnetic workpiece and the magnetic saturation. The actual research frontiers in IH systems mainly focus on increasing efficiency in already existing IH systems applications [1], optimal control [2], load and temperature estimation using indirect observers [3], [4], usage of data driven methods for parameter estimation [5] and converter design [6], [7].

This article takes a cue from [8] and proposes a methodology for the data extraction and interpolation of non linear equivalent circuit characteristics resulting from frequency stationary coupled thermal-electromagnetic 3D-FEM simulations. The aim of this investigation is to track the behaviour of the equivalent RL series parameters with respect to frequency, current and temperature for integration in simpler and faster electro-thermal lumped parameter models. In this paper the IH principles, the 3D FEM IH problem and settings and the data retrieving methodology are analysed with an application case study. The case study takes inspiration from an waterpipe IH system recently developed in [9]. It involves a curved pancaked coil of ten series windings around a constrained angular section of a steel ferromagnetic tube for the partial heating of a moving pipe during manufacturing process of a tube.

In the first section a bried description of the problem and different methodologies for the extraction of the RL lumped parameters are provided. In the second section a 3D coupled electromagnetic-thermal FEA with non linear magnetic B-H characteristics is exploited for the extraction of the inductance and resistance with integral numerical methods for some informative operating points at different frequencies and currents. Here, the thermal coupling is accounted both as linear thermal resistivity coefficient inferred by measurements performed on austenitic ferromagnetic steel AISI-410 and with BH curve-Temperature dependency. The equivalent circuital RL parameters are mapped with modified Akima's cubic interpolation method for piecewise polynomials with C^1 derivatives [11]. In the results section the behaviour of the nonlinear equivalent circuit on a quasi resonant single switch converter is shortly analysed. This research represents the starting point for the development of a coupled thermo-electric digital twin for the characterisation, modelling and control of induction heating system at wireless frequency power transfer.

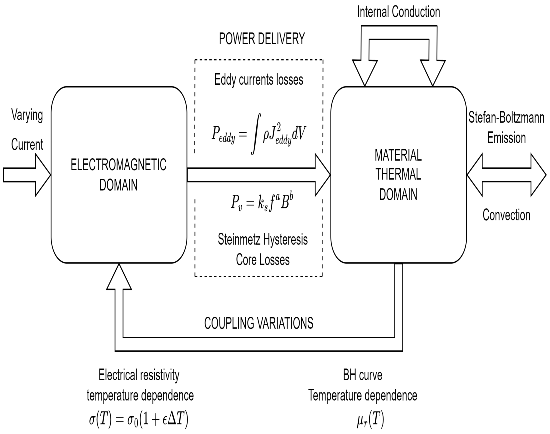

Figure 1: Coupling synthesis between the electromagnetic domain and the thermal domain.

I. Induction Heating Principles

According to the Faraday-Neumann law, a time variation of the magnetic field generates a curl rotating electric field concatenating the magnetic flux. If the magnetic flux passes in a conductive material, the electric field generates a rotational current called eddy current. Any material run by electrical currents is heated depending on its resistance. The resulting effect is known as induction heating. If the material properties enhance the induction field, the heating is amplified. In the Fig. 1 the flowchart represents in a schematic way the coupled physics. With the monodirectional coupling, no temperature dependence can be introduced in the electromagnetic weak form problem unless the introduction of iterative calculation process. The weak form problem introduces the necessary terms for the estimation of the derived quantities. The IH systems can be modelled as lumped equivalent parameters as a single pole RL series equivalent circuit. In the 2-parameters model the inductance can be calculated from the total energy stored as magnetic field. Indeed:

$$U_{mag} = \frac{1}{2} L I_{rms}^2 = \Re\left[\frac{1}{2}\int_{\Omega} \vec{\hat{B}} \cdot \vec{\hat{H}} \delta V\right] \tag{1}$$

For harmonic current forcing terms in FEA, the equivalent resistance is simply calculated from the imaginary part of the previous equation evaluated in the material domain Ω_m. Starting from the magnetic energy integral:

$$\frac{1}{2}\int_{\Omega_c} \vec{\hat{A}} \cdot \vec{\hat{J}}^{\star} \delta\Omega_c \tag{2}$$

From the Faraday equation, the potential vector field is:

$$\hat{A} = -\frac{j}{\omega}\vec{\nabla}\hat{V} \tag{3}$$

Thus, the integral can be divided into the three spatial coordinates:

$$\int -\frac{j}{\omega}\vec{\nabla}\hat{V} \cdot \vec{\hat{J}}^{\star}\delta V = -\int \frac{j}{\omega}\vec{\nabla}_x\hat{V}\delta x \cdot \int \vec{\hat{J}}_x^{\star}\delta S_{yz} - \int \frac{j}{\omega}\vec{\nabla}_y\hat{V}\delta y \cdot \int \vec{\hat{J}}_y^{\star}\delta S_{xz} - \int \frac{j}{\omega}\vec{\nabla}_z\hat{V}\delta z \cdot \int \vec{\hat{J}}_z^{\star}\delta S_{xy} \tag{4}$$

The resulting terms are the voltage inside the material and the currents in the three directions of the space. The current and voltage inside the material are related by the Ohms law for general impedances:

$$V_0 \exp(j\omega t) = (R + j\omega L) I_0 \exp(j\omega t + j\phi) \tag{5}$$

where ϕ is the phase displacement between the current and the voltage. The resistance referred to only eddy currents is obtained by the Ohms law:

$$R = -\omega\Im\left[\frac{\int_{\Omega_c} \vec{\hat{A}} \cdot \vec{\hat{J}}^{\star}\delta\Omega_c}{I_{rms}^2}\right] \tag{6}$$

II. Case study and material modeling

An applicative case study for manufacturing process (figure 3-b) is considered and simulated with COMSOL [12], a 3D-FEM commercial software for multiphsysics coupled analysis. It considers the heating of a moving tube made of AISI-410 ferromagnetic austenitic stainless steel with a geometrical constraint: the coil can not wrap up the tube as a solenoid. A pure copper curved pancake coil is designed to heat up only an angular section of the workpiece. A very fine boundary layer mesh is set in order to get finer mesh at the boundaries near the coil. The hysteresis losses are not considered for the modelling of this this case study. Indeed, for materials with very low resistivity, the dominant heating factor comes from the eddy currents. The BH curve dependency of the temperature is accounted in the stationary electromagnetic simulations. Generally, the temperature has a not negligible impact over the variation of the BH curve. The saturation in the BH curve changes mainly for temperatures in material transition phases, until the temperature reaches the Curie limit, in which the material loses its ferromagnetic properties. A linear decreasing BH curve saturation - Temperature dependence has been taken into account. The second thermal coupling is introduced by adding a linear modeling for the electrical resistivity temperature dependence that usually well represents the material behaviour for different temperatures in short ranges:

$$\rho(T) = \rho_{T_{room}}\left[1 + \epsilon(T - T_{room})\right] \tag{7}$$

The resistivity temperature coefficient is obtained by linear regression of equivalent resistance measurements between room temperature and 130 [C] over a testing material specimen. As a consequence of the increase of the electrical resistivity ρ, the skin depth should increase causing a variation in the coil-metal coupling:

$$\delta = \sqrt{\frac{\rho(T)}{\pi\mu_0\mu_r f}} \tag{8}$$

The negative part of the coupling term (second term in equation **??**) decreases for high temperatures, thus the total inductance should grow up. The BH curve has lower saturation of induction field for high temperatures. The coupling variation with respect to the temperature is less than $1\%/100[C]$, and it can be neglected for short temperature intervals 25-150 [C]. In order to assess the material behaviour, the thermal characteristics of a specimen of AISI 410 are tested with a commercial IH system. The material is warmed up with an industrial air heater and the equivalent resistance is measured for different temperatures. The figure 2 represents the points of the resistance (blue dots) and inductance (red dots) measured with respect to the temperature. The linear thermoresistive coefficient ϵ that best fit the data is $0.0017[K^{-1}]$, with RMS error of $0.0095[\Omega]$.

In the figure 3 the FEM simulation is used to extract

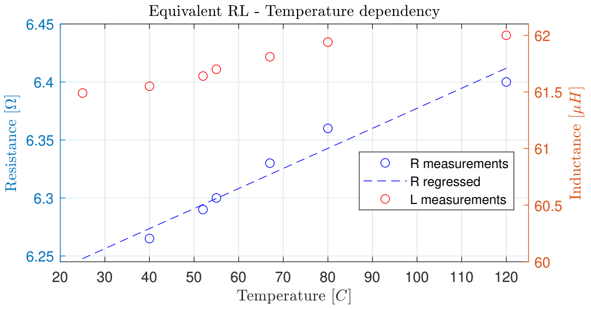

Figure 2: Measured equivalent resistance and inductance data and resistance linear regression.

the equivalent resistance and inductance for different currents (from 2.5[A] to 22.5[A]) and frequencies (from 80[kHz] to 100[kHz]). The maps highlight the nonlinear behaviour. A first observation concerns the equivalent resistance and optimal solution. The equivalent resistance for the data is higher at 120[Amps]. The efficiency of induction heating systems is based on the ratio between the energy delivered to the workpiece and all the losses including the coil and converter ones. The power ratio is equivalent to the ratio between of equivalent resistances. The second observation concerns the magnetic saturation of the steel. The inductance increases because the material can not manage all the magnetic field, and the induced current does not increase with the prescribed current.

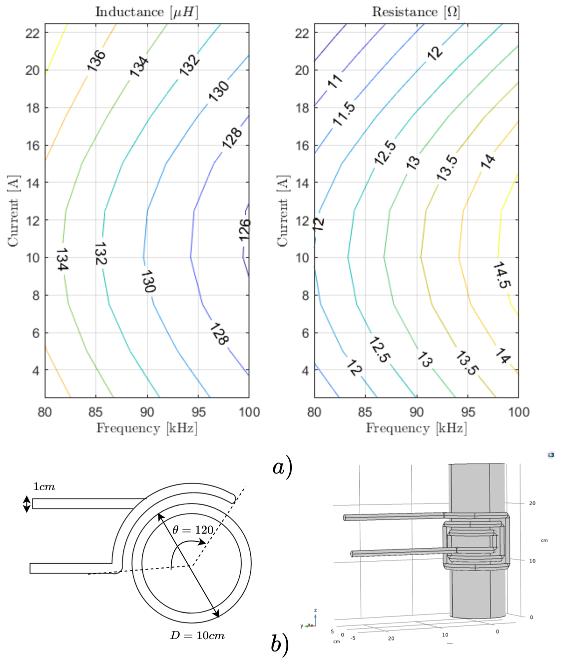

Figure 3: Data mapping of equivalent RL parameters from FEM analysis used for thermo-electrical coupled simulations for different current and frequencies (a) of the IH system case study geometry (b).

The m-Akima interpolation of data along the frequencies and currents is exploited to estimate the equivalent inductance and resistance values for different frequencies. This interpolation method is chosen because it is less aggressive and generates less high frequency undulations. The set of validation frequencies is set outside the data range $(60 - 80[kHz]$ and $100 - 120[kHz])$ and inside the data frequency interval. The figure 4 represents the data extracted by the FEA model (circles) over which the m-Akima interpolation is regressed (results in dotted lines). An out of the interval validation set (stars) is used to assess the validity of the interpolated model.

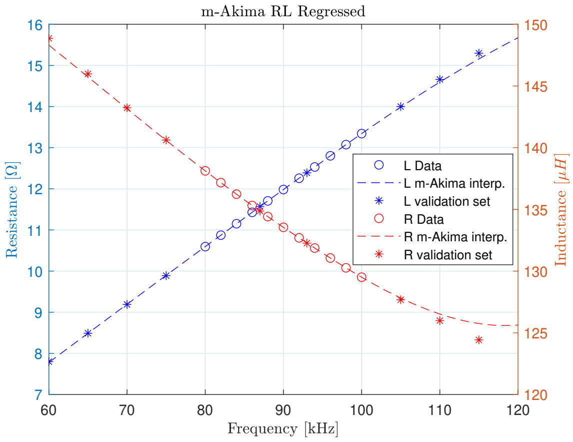

Figure 4: m-Akima interpolation (dotted lines) and data set extracted from COMSOL FEA (circles). The validation set (stars) assess the validity of m-Akima interpolation for inductance and resistance values outside and inside the frequency range with peak current of 20[A].

In order to reduce IH simulation complexity, the equivalent interpolated parameters are introduced in a circuital coupled lumped parameters electro-thermal simulation as in Fig. 6. The inverter quantities are fed to the RL series. The electrical power converter parameters are based on a commercial single IGBT switch parallel quasi resonant inverter. Despite single IGBT converter are cheaper, the main drawback of this converter is the single control variable. Indeed, the main difficulty deals with the design of the coil in order to get suitable values of inductance to manage the necessary current in the desired frequency interval. A power frequency modulation (PFM) regulation strategy with PI control is exploited to regulate the generated power to a reference of 150[W]. Its robustness to frequency $(80 - 85[kHz])$ and linear temperature $(T_{room} - 100[C])$ variation is tested in Fig. 5. In the first plot the resistance and inductance behaviour are represented in the time domain. The power prediction is not affected by this saturation due to low RMS currents. The second plot concerns the current in RL branch. After an initialization cycle the maximum current is controlled by PFM of IGBT to reach the generated power (third plot). The behaviour of the inverter for the nonlinear quantities is compared to fixed RL branch. The average peak to peak current difference between the fixed RL test and nonlinear RL at the maxima is 1.21[A]. The average power difference between the two cases in the control horizon is 7.59[W] with the maximum at the start of 32[W].

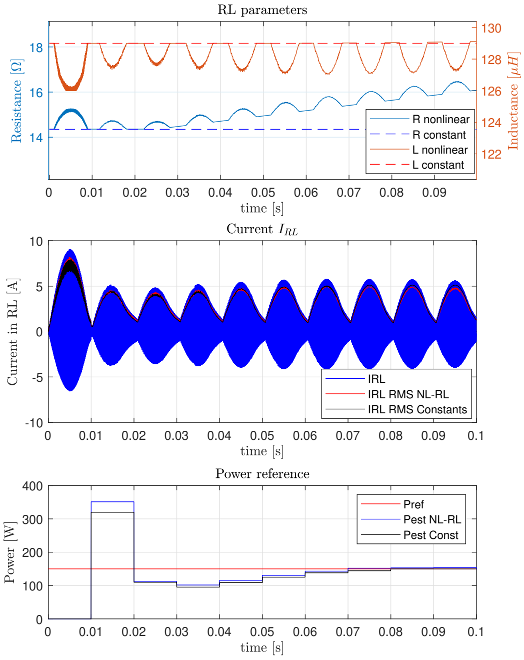

Figure 5: In the first plot are represented the $R(f, I, T)$ and $L(f, I, T)$ parameters behaviour in the coupled model and fixed parameters (dotted lines). The RMS currents passing in the equivalent nonlinear loads (red) are compared to the fixed RL case (black) in the second plot. The effectiveness and robustness of PI-PFM power control is proved by the convergence to 150[W] both for temperature rising workpiece with nonlinear parameters and fixed RL branch.

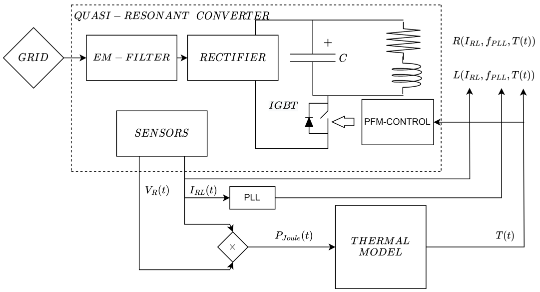

Figure 6: Coupled model and how the $R(f, I, T)$ and $L(f, I, T)$ interpolated equivalent parameters are integrated in the converter scheme.

CONCLUSIONS

The starting point for an accurate description of an IH digital twin is provided in this article. From a general mathematical analysis of the electromagnetic-thermal coupled problems with a description of how the physics is interpreted by FEM simulations, some methodologies about deriving RL series equivalent electrical parameters are presented. A working methodology to interpolate RL data with better resolution and augmented interval for both frequency and current is provided. The behaviour of a IH system when supplied to a parallel quasi resonant inverter with PFM power control is tracked also for temperature rising over the control horizon. Moreover, it is compared to fixed RL parameters case.

Future developments concern the test of variable capacitors to control RLC resonance tank, the design of a coupled thermal equivalent circuit for a moving billet heated on its radial section with finite difference technique for the coupling in Fig. 6. Moreover, the simulation of holes inside the sliding billet will be analysed from a nominal heating situation to the detection of holes through equivalent RLC impulse response.

REFERENCES

[1] E. Plumed, I. Lope and J. Acero, "Induction Heating Adaptation of a Different-Sized Load With Matching Secondary Inductor to Achieve Uniform Heating and Enhance Vertical Displacement," in IEEE Transactions on Power Electronics, vol. 36, no. 6, pp. 6929-6942, June 2021, doi: 10.1109/TPEL.2020.3033833.

[2] Rapoport, E., Pleshivtseva, Y. (2006). Optimal Control of Induction Heating Processes (1st ed.). CRC Press. https://doi.org/10.1201/9781420019490

[3] H. Sarnago, O. Lucía and J. M. Burdio, "A Versatile Resonant Tank Identification Methodology for Induction Heating Systems," in IEEE Transactions on Power Electronics, vol. 33, no. 3, pp. 1897-1901, March 2018, doi: 10.1109/TPEL.2017.2740998.

[4] Li, Z.-F., Hu, J.-C., Huang, M.-S., Lin, Y.-L., Lin, C.-W., Meng, Y.-M. (2022). Load Estimation for Induction Heating Cookers Based on Series RLC Natural Resonant Current. Energies. doi:10.3390/en15041294

[5] O. Lucia, D. Navarro, P. Guillén, H. Sarnago and S. Lucia, "Deep Learning-Based Magnetic Coupling Detection for Advanced Induction Heating Appliances," in IEEE Access, vol. 7, pp. 181668-181677, 2019, doi: 10.1109/ACCESS.2019.2960109.

[6] Vishnuram, P., Ramachandiran, G., Sudhakar Babu, T., and Nastasi, B. (2021). Induction Heating in Domestic Cooking and Industrial Melting Applications: A Systematic Review on Modelling, Converter Topologies and Control Schemes. Energies, T. 14. doi:10.3390/en14206634

[7] O. Lucía, P. Maussion, E. J. Dede and J. M. Burdío, "Induction Heating Technology and Its Applications: Past Developments, Current Technology, and Future Challenges," in IEEE Transactions on Industrial Electronics, vol. 61, no. 5, pp. 2509-2520, May 2014, doi: 10.1109/TIE.2013.2281162.

[8] Young-Sup Kwon, Sang-Bong Yoo and Dong-Seok Hyun, "Half-bridge series resonant inverter for induction heating applications with load-adaptive PFM control strategy," APEC '99. Fourteenth Annual Applied Power Electronics Conference and Exposition. 1999 Conference Proceedings (Cat. No.99CH36285), 1999, pp. 575-581 vol.1, doi: 10.1109/APEC.1999.749738.

[9] Aguilar-Peréz LA, Merino-García JA, Ramírez-Crescencio F, Villanueva-Fierro I, Torres-SanMiguel CR. Experimental design and numerical validation of a low-cost water heater by electromagnetic induction. Advances in Mechanical Engineering. October 2021. doi:10.1177/16878140211055251

[10] Emmanuel Creuse, Patrick Dular, Serge Nicaise, About the gauge conditions arising in Finite Element magnetostatic problems, Computers and Mathematics with Applications, Volume 77, Issue 6, 2019, Pages 1563-1582, ISSN 0898-1221, https://doi.org/10.1016/j.camwa.2018.06.030.

[11] Alexandru Mihai Bica, Optimizing at the end-points the Akima's interpolation method of smooth curve fitting, Computer Aided Geometric Design, Volume 31, Issue 5, 2014, Pages 245-257, ISSN 0167-8396, https://doi.org/10.1016/j.cagd.2014.03.001.

[12] COMSOL Multiphysics v. 6.0. www.comsol.com. COMSOL AB, Stockholm, Sweden.

Transient analysis of magnetic gear asynchronous operation with damping effects

Mattia Filippini[1], Piergiorgio Alotto[1],
[1]Department of Industrial Engineering, University of Padova, Via Gradenigo 6/a, 35131, Padova

This paper focuses on the transient analysis of magnetic gears when the synchronism is lost due to sudden torque variations. If the transmission input shaft is not speed-controlled or if the implemented control is slower than the mechanical dynamic response of the magnetic gear, the new equilibrium point can be at much higher rotational speed. In order to avoid damages due to the over-speed, damping windings can be adopted and their performances have to be evaluated through transient simulations. An efficient technique to address the problem based on a finite element/boundary element formulation is adopted in this paper for the cases without external circuit couplings and some manufacturing solutions for the damper windings are discussed.

***Index Terms*—Loss of synchronism, Magnetic gears, Damping windings, FEM/BEM**

I. INTRODUCTION

MAGNETIC gears offer some well known advantages if compared to mechanical gearboxes [1]. Among others, the possibility to operate in asynchronous operation offers an intrinsic advantage since mechanical frictions are no more required in the transmission chain. On the other hand, special care has to be taken if the synchronism is lost, since the rotors speed can become excessive [2], [3]. A common constructive practice is to fill the slots between the iron poles with epoxy resins or glass fibers and normally stainless-steel rods are adopted for enhancing the structure's stiffness. In this paper the iron poles rotor has a fixed position and the rods are connected together when the synchronism is lost through an external switch. Thus, in analogy with damping windings of synchronous machines, a damping effect is introduced to limit the rotor rotational speed. The switch could be commanded also to damp the oscillations due to rapid dynamics that normally arise because of mechanical load or speed variations. The effect is the same obtained in [3] without adding damper windings.

The well known 2D Finite Element-Boundary Element technique (FEM/BEM) is used to address the time domain problem; the algorithm is implemented in the Julia programming language [4] and validated by comparison with a commercial FEM code. The paper is organized as follows: Sec. II describes the test case geometry and the model adopted for the equivalent network. In Sec. III the formulation adopted is shown, and in Sec. IV the proposed strategy is validated. In Sec. V, the rods-cage damping effect is shown for the test case geometry and the computational time is compared to the commercial FEM one.

II. MAGNETIC GEAR GEOMETRY

The crucial component in magnetic gears is the flux modulator. Large forces are developed on the iron poles, thus glass fibres, epoxy resins and stainless rods are normally adopted to enhance the iron pole stiffness. A possible solution is shown in Fig. 1, where a magnetic gear with $Pi = 2$ inner pole pairs, $Po = 11$ outer pole pairs and $q = 13$ pole pieces is equipped with $2q$ stainless rods, and the assembly of rods and iron poles is encapsulated with glass fibres. The rods are practically solid conductors with a conductivity in the order of $\sigma \simeq 1\ MS/m$. Normally the induced eddy currents have a negligible effect, but if the bars are short circuited through conductive rings, a closed cage is built and currents are free to circulate. The lumped equivalent circuit is depicted in Fig. 2, where the model of the outer rings is constituted by a simple resistive network (since the end-ring self and mutual inductances calculation would require a 3D FEM calculation).

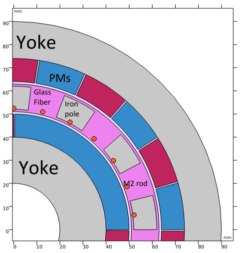

Parameter	Symbol	Value
Inner radius	R_{in}	0.02 m
Inner yoke	y_{in}	0.02 m
PMs thickness	t_{PM}	0.01 m
Airgaps size	t_{gap}	0.002 m
Poles thickness	t_{pole}	0.01 m
Outer yoke	y_{out}	0.014 m
Rods radius	r_{rods}	0.001 m
Axial length	L	0.1 m

Fig. 1. Test case geometry with M2 stainless steel rods (orange color) positioned close to the inner airgap. In this paper, the flux modulator is fixed, while inner and outer rotors can rotate.

III. PROBLEM FORMULATION

The standard 2D vector potential formulation without external circuit equations reads:

$$\sigma \frac{V_{PM}}{L} + \sigma \frac{\partial A_z}{\partial t} - \nabla \cdot \nu \nabla A_z = J_z + \nabla_{2D} \times \mathbf{M}(A_z) \quad (1)$$

where A_z is the z component of the vector potential, σ is the electrical conductivity, V_{PM} is the voltage between the permanent magnets (PMs) end faces, L is the machine length, ν is the reluctivity, $M(A_z)$ includes the nonlinear iron magnetization or the linear PMs magnetization and J_z is the source current density. In the case of non-magnetic solid conductors or single turn windings, (1) reads [5]:

$$\begin{cases} \sigma_i \frac{\partial A_z}{\partial t} - \nabla \cdot \nu \nabla A_z - \frac{\sigma_i}{S_i} \int_{\Omega_i} \frac{\partial A}{\partial t} d\Omega = \frac{i_i}{S_i} \\ \frac{L}{S_i} \int_{\Omega_i} \frac{\partial A}{\partial t} d\Omega + \frac{i_i}{\sigma_i S_i} = e_i + R_i \cdot i_i = u_i \end{cases} \quad (2)$$

Manuscript received December 1, 2018; revised August 26, 2018. Corresponding author: M. Filippini (email: mattia.filippini@studenti.unipd.it).

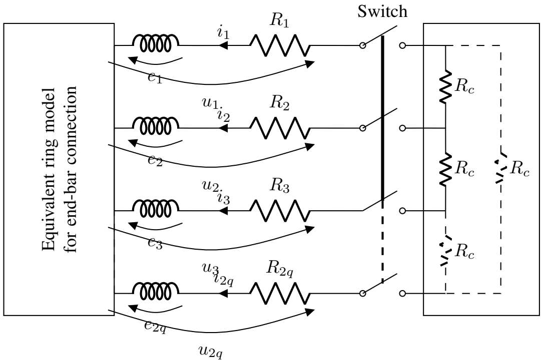

Fig. 2. Circuit scheme of the magnetic gear with bars: the two ring models are equal and constituted by purely resistive networks in this case. Inductances are used symbolically in the picture but are actually modelled by FEM.

where σ_i, S_i, Ω_i are the i^{th} bar conductivity, cross section and computational domain, i_i, u_i, E_i and R_i are the i^{th} bar net current, voltage, electromotive force and resistance respectively (see Fig. 2).

In the airgap domains, the standard boundary element (BEM) is adopted [6]: this method allows to easily deal with the rotor motion and to obtain highly accurate solutions.

Eqs. (1), (2) and the BEM equations are coupled with two mechanical ordinary differential equations (ODE) of the type:

$$J\frac{d^2\theta}{dt^2} + \left(b + k_{fan} \cdot \frac{d\theta}{dt}\right) \cdot \frac{d\theta}{dt} = T_{em}(\theta) + T_{mecc} \qquad (3)$$

where J is the rotor inertia, b and k_{fan} are the linear and quadratic damping factors due to bearings and air friction respectively, θ is the rotor angular position, T_{em} is the electromagnetic torque developed on the rotor and T_{mecc} is the external mechanical torque applied. When the switch closes, the resistance value in the circuit equations changes accordingly. In Eq. (1), considering the case of insulated and segmented PMs, $V_{PM} = \frac{L}{S_i}\int_{\Omega_i}\frac{\partial A}{\partial t}d\Omega$ and σ is taken as a fictitious value $\sigma' = \sigma_{PM}/k$ to consider the segmentation effect. In particular this reduction factor is $k = 10$ for the outer PMs and $k = 4.5$ for the inner ones; these values have been calculated through 3D FEM simulations that are omitted here for brevity.

To solve the magneto-quasi static problem, the FEM/BEM algorithm equipped with Anderson acceleration [7] has been implemented with Julia programming language [4]. The time domain problem is solved through an adaptive θ-method scheme, where the time step is doubled if the number of nonlinear iterations is below a fixed threshold (and viceversa).

IV. MODEL VALIDATION

In Fig. 3, the FEM/BEM code is validated by comparison with a commercial FEM code on a constant speed problem where the initial solution is the null vector: at $t = 0$ s the magnetic field starts to diffuse and the torque grows till the steady state value. Adopting the same discretization, the FEM/BEM results are closer to the quadratic order FEM case because of the higher accuracy of BEM. The same simulation is run in Fig. 4, with short-circuited rods and $R_c = 1\mu\Omega$ in Fig. 2. In order to obtain the same solution accuracy, the FEM degrees of freedom (DOFs) in the airgap have been increased by a factor 2. The bar current is reported in Fig. 5: the initial peak is due to the sudden magnetization step at $t = 0$ s. The electromagnetic torques on the inner and outer rotors required to keep the stationary-speed regime are higher in Fig. 2 than Fig. 3, because of the damping effect due to the rods cage.

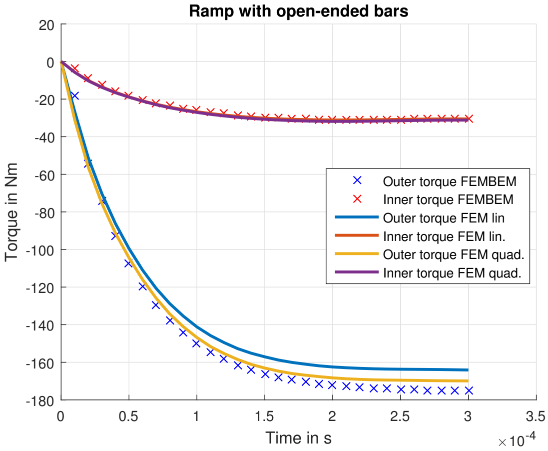

Fig. 3. Validation of the proposed algorithm with open-ended bars through the comparison with the commercial FEM Comsol. Inner and outer speeds are fixed according to the gear ratio $\omega_{in} = 5000$ rpm $\omega_{out} = -909$ rpm.

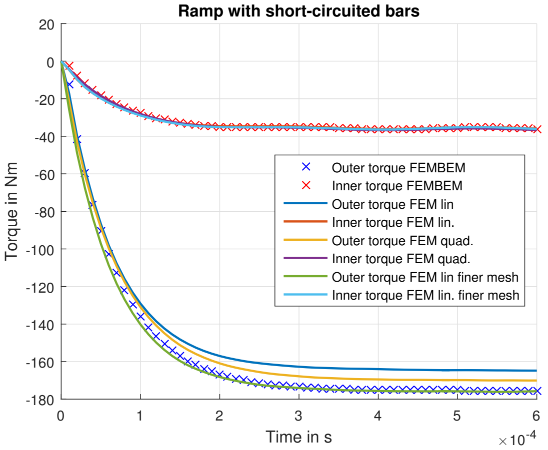

Fig. 4. Same simulation of Fig. 3 with short-circuited bars.

V. DAMPING EFFECT

The magnetic gear studied in this paper has the parameters shown in Tab. I. The rotors' inertias are lower than the real values for this test case in order to reduce the mechanical time constants and consequently the computational time required, but the steady state results are not affected. The power source connected to the inner shaft is supposed to deliver a constant torque T_{mecc} below the maximum power point and a constant power above the same point. When the synchronism in lost, in the hypothesis of no action from the source controller (because of slow operation or fault in detection systems), Eq. (3) for the inner rotor can be written as:

$$J_{in}\frac{d\omega_{in}}{dt} + (k_q + k_e) \cdot \omega_{in}^2 + b_{in}\omega_{in} = T_{mecc} = \frac{P_{max}}{\omega_{in}} \qquad (4)$$

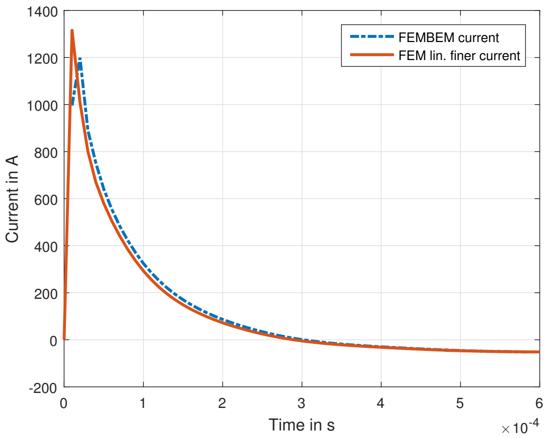

Fig. 5. Current comparison for one bar for the simulation in Fig. 4.

TABLE I

ELECTRO-MECHANICAL PARAMETERS: THE ROTOR INERTIAS ARE LOWER THAN THE REAL ONES ($\approx 1/10$)TO LIMIT THE COMPUTATIONAL TIME.

Quantity	Symbol	Value	Unit
Inner pole pairs	Pi	2	-
Outer pole pairs	Po	11	-
Modulator poles	q	13	-
Inner rotor inertia	J_{in}	$1E-4$	kgm^2
Outer rotor inertia	J_{out}	0.17	kgm^2
Inner rotor damping	b_{in}	$1E-3$	$Nm\cdot s/rad$
Outer rotor damping	b_{out}	1.7	$Nm\cdot s/rad$
Air friction + iron loss	k_q	$1E-6$	Nms^2/rad^2
Nominal inner speed	ω_{in}	5000	rpm
Failure speed	ω_{in}^{max}	15	$krpm$
Nominal torque	T_{mecc-n}	30	Nm
Max source power	P_{max}	18	kW
Rings resistance	R_c	1	$\mu\Omega$
Rod conductivity	σ_r	1.45	MS/m
PMs remanence	B_r	1.2	T

where k_q is the quadratic damping term that includes the air friction coefficient k_{fan} and the eddy current loss in yokes and iron poles, k_e is the electrical damping coefficient that includes eddy current losses in PMs and also the losses associated to the rods currents. Thus, the transmission electromagnetic loss due to iron sheets and PMs previously embedded in the term T_{em} of (3) have been incorporated into k_q and k_e respectively.

In order to show the rods-cage damping effect, two identical simulations have been used, one with open switch and the other with closed switch. The magnetic gear is in a zero-torque equilibrium as initial condition and a step torque $T_{mecc} = 30$ Nm is applied at $t = 0$, causing the asynchronous operation of the magnetic transmission.

Fig. 6 shows the steady state solutions varying k_q and k_e and the dynamic response of the nonlinear ODE (4). Magnetic gears with high mechanical and electromagnetic efficiency have small k_q coefficients and the reduction effect due to the electrical damping k_e is more visible. For the study case in this paper, the simulation time is in the range $[0-0.05]$ s, according to Fig. 6.

Fig. 7 shows the comparison between the inner and outer rotor torques for the cases with open and closed switch. When the rods are not connected, the torque components are

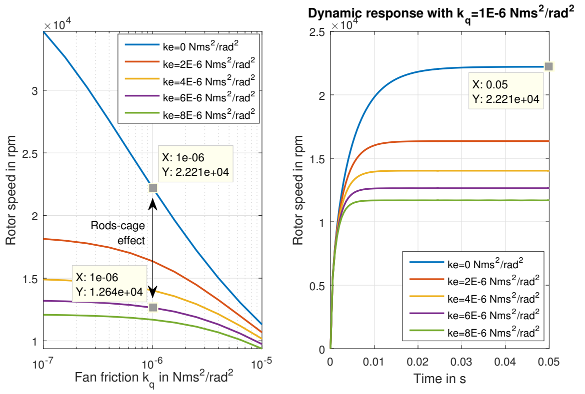

Fig. 6. Steady state solution of Eq. (4) varying k_q and k_e (left). Dynamic response of Eq. (4) with $k_q = 1e{-}6\ Nms^2/rad^2$ according to Tab I (right).

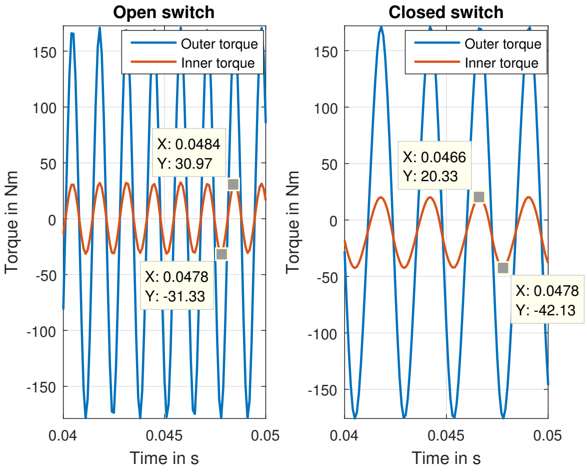

Fig. 7. Comparison between the electromagnetic torques of inner and outer rotor in steady state for the cases with open and closed switch. The PM eddy current loss and rods-induced currents generate a constant resistive torque. The steady state rods current density is $J \approx 50\ A/m^2$.

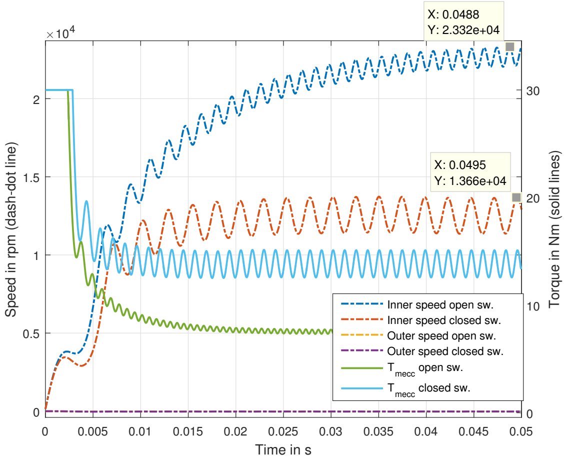

Fig. 8. Inner rotor speed and external torque for open and close switch cases. The rods-cage decreased the tip speed by a factor $k = 1.71$. Since the source is power-limited, the torque T_{mecc} is higher in the case with lower speed.

TABLE II
COMPUTATIONAL TIME FOR FEM/BEM AND COMMERCIAL CODE. BOTH METHODS ADOPTS LINEAR SHAPE FUNCTIONS.

Switch state	Tool	Method	Convergence	Time
Open	Comsol	BDF	Tol. factor $\tau < 0.1$	15148 s
Open	FEM/BEM	θ-method	Rel.Tol. $\gamma < 10^{-4}$	7057 s
Closed	FEM/BEM	θ-method	Rel.Tol. $\gamma < 10^{-4}$	8072 s

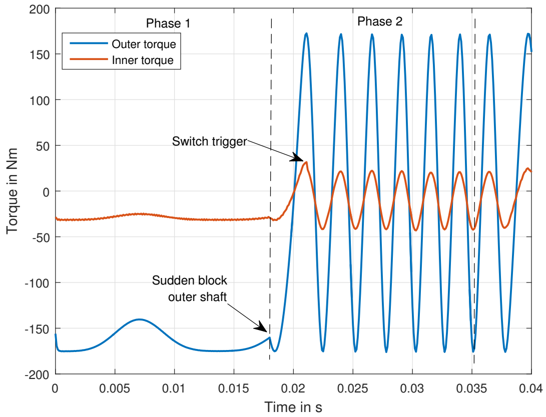

Fig. 9. Inner and outer torques (study case 2). In phase 1 the gear operates in steady state and at $t = 0.18$ the outer rotor is suddenly blocked. The rods switch is triggered when the inner rotor speed is $\omega_{in} > 10$ krpm.

sinusoidal and the inner torque has a small negative DC bias due to the PMs eddy current loss. In the closed-circuit case, the negative DC bias is bigger because of the additional damping contribute due to the rods. This DC bias allows to reduce the stationary speed, as visible in Fig. 8. The inner rotor tip speed is reduced from $\omega_{in} = 23.3$ krpm to $\omega_{in} = 13.7$ krpm, with a reduction factor $k = 1.71$. Therefore, the rods-cage damping effect can prevent mechanical failures in the fast transients during asynchronous operation. The bar current peak in steady state is $I^p = 150$ A and the closed-switch operation is limited by the rods over-temperature limit ΔT. According to the geometry and the material parameters, the limit operation time with closed switch has been estimated as $\Delta t = 1.9$ s in adiabatic conditions according to $c\rho V_b \Delta T = P_b \Delta t$, where $c = 500\ J/kgK$, $\rho = 7800\ kg/m^3$, $V_b = 314\ mm^3$ and $P_b \approx 500\ W$ are specific weight, heat capacity, volume and power loss of each bar ($\Delta T = 800\ K$).
In Tab. II the FEM/BEM code time is compared with the commercial software Comsol. The discretization in Comsol is based on linear shape functions and the time domain problem is solved through a backward difference method (BDF) with fixed time step $\Delta t = 1e-4$ s. The simulations are run on a workstation with two 6-core/12 thread processors (Intel Xeon E5645 @2.4 GHz) and 112 GB of RAM. For both cases, $DOF \approx 40k$ holds. Timings are not directly comparable due to differences in the linear and nonlinear solvers and are given to indicate the required simulation time.

The case study 2 is a gear initially operating in steady state with open switch. At $t = 0.18$ s, the outer rotor is suddenly blocked and the operation becomes asynchronous. Considering that the source controller takes $\Delta t = 15$ ms to detect the fault and nullify the source power, the inner rotor starts to accelerate and the switch closes when the rotor speed $\omega_{in} > 10$ krpm. Figs. 9 and 10 show the torques and speed for this test case. The rods damping is fundamental to reduce the rotor speed in phase 2 of Fig. 10.

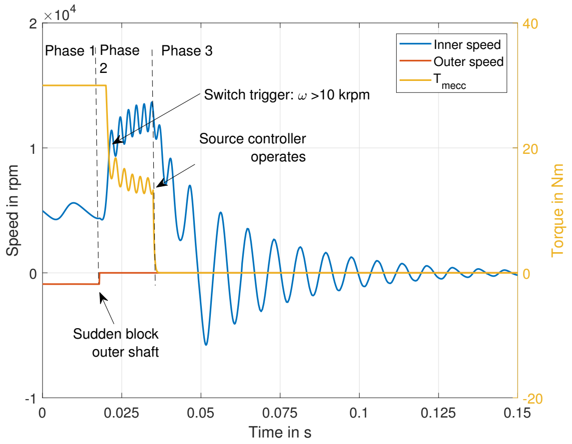

Fig. 10. Inner, outer rotors speed and external torque (study case 2). Phase 1 is the steady state operation, phase 2 is the accelerating fast inner transient and phase 3 is the damped transient till stop. The maximum inner speed in phase 2 is the same obtained in Fig. 8 with closed switch.

VI. CONCLUSION

In this paper an easy strategy to reduce the magnetic gear rotational speed in asynchronous conditions is proposed. The solution is based on the connection of structural rods to form a closed cage that provides a damping effect, thus only the multi-poles switch is requested and the conventional magnetic gear designs does not require major modifications. A complete simulation algorithm based on the finite element/boundary element method has been used to show the damping effect on a test case geometry. For the particular case analyzed in this paper, the rods-cage allowed to reduce the runaway speed by a factor $k = 1.7$. This reduction could avoid mechanical failure due to slow control dynamics of the power source. The switch could also be commanded in order to reduce the oscillatory performance when sudden load variations occur.

REFERENCES

[1] K. Atallah and D. Howe, *A novel high-performance magnetic gear*, IEEE Transactions on Magnetics, vol. 37, no. 4, pp. 2844-2846, Jul 2001.
[2] R. G. Montague, C. M. Bingham and K. Atallah, *Magnetic gear overload detection and remedial strategies for servo-drive systems*, SPEEDAM 2010, Pisa, 2010, pp. 523-528.
[3] S. Pakdelian, N. W. Frank and H. A. Toliyat *Damper windings for the magnetic gear* IEEE Energy Conversion Congress and Exposition, Phoenix, AZ, 2011, pp. 3974-3981.
[4] J. Bezanson et al. *"Julia: A Fresh Approach to Numerical Computing"* SIAM review, vol. 59, pp. 65-98, 2017.
[5] S. Niu, K. T. Chau, J. Li and W. Li, *Eddy-Current Analysis of Double-Stator Inset-Type Permanent Magnet Brushless Machines*, IEEE Transactions on Applied Superconductivity, vol. 20, no. 3, pp. 1097-1101, June 2010.
[6] D. Poljak, A. C. Brebbia, *"Boundary element methods for electrical engineers* Vol. 4. WIT Press, 2005.
[7] F. H. Walker, N. Peng, *"Anderson Acceleration for Fixed-Point Iterations"* SIAM Journal on Numerical Analysis, vol. 49, pp. 1715-1735, 2011.

Neural Surrogate for Optimization of Synchronous Reluctance motor

Francesco Moraglio, Gaetano Dilevrano, Paolo Ragazzo, Gianmario Pellegrino and Maurizio Repetto

Dipartimento Energia ”Galileo Ferraris”
Politecnico di Torino, Corso Duca degli Abruzzi 24, 10129 Torino, Italy
E-mail: maurizio.repetto@polito.it

***Abstract*—Optimization of electromagnetic devices often requires the evaluation of performance by means of numerical codes whose computational cost is non negligible. Surrogate functions, providing local or global interpolation of the objective function, can speed up the optimization process. The present work proposes first results of this approach to the optimization of synchronous reluctance motors: performance evaluation is performed by a procedure based on sizing rules and 2D finite element analysis, developed by some of the Authors, neural surrogate is applied and multi-objective optimization is then performed.**

***Index Terms*—multi-objective optimization, neural surrogate, synchronous reluctance motor**

I. INTRODUCTION

Over the last years, the raw materials cost has been strongly volatile. In particular, concerning the electric motors market, the permanent magnet price experienced a sharp increase. This inducts several manufacturers to evaluate magnet-less options, as induction machines (IMs) and synchronous reluctance (SyR) machines, shown in Fig. 1. SyR motors can achieve higher efficiency than IMs, thanks to the absence of rotor Joule loss. In addition, the rotor cage absence simplifies the manufacturing process. Besides these advantages, SyR machines have lower power factor, demanding a larger converter; also, they require an accurate magnetic identification to earn a stable speed control.

This work focuses on automatic design methodologies for SyR motor; some technical background on this type of machine can be found in Sec. II.

Currently, the most used design procedures for SyR machines are based on optimization algorithms, since any designer is somehow pursuing certain objectives. Sec. III explains how to formulate this problem in adequate mathematical terms and gives ideas on how it can be solved using algorithms.

Traditional optimization processes rely on a massive use of finite element analysis (FEA) simulations, resulting in time consuming procedures. The present work aims to preserve the capability of the optimization algorithms while shrinking the computational burden by replacing FEA with surrogate functions. The paper proposes two lightweight neural networks (NN) to act as surrogates: our experiments show that techniques drawn from Deep Learning (DL) allow the creation of efficient models, which achieving satisfying performance on a simplified test problem. Thus, details on surrogates are discussed in Sec. IV.

The analysis are based on the open-source design and simulation platform SyR-e [1]. The built-in optimizer in SyR-e uses a variation of the NGSA-II algorithm [2] [3] which runs FEA on FEMM [4], a tool for solving electromagnetic problems on two-dimensional domains. The present work demonstrates how the current SyR-e optimizer can benefit of a surrogate function in terms of computational time, turning hours of calculations into seconds preserving the results’ accuracy.

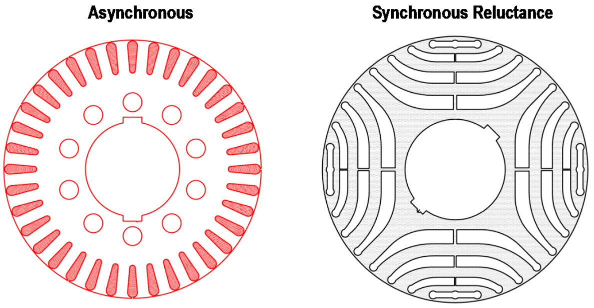

Fig. 1. Comparison of rotors for two types of machines: induction motor on the left and synchronous reluctance on the right.

Indeed, the computationally expensive procedure (i.e. training of each net) is executed only once, while we can employ the trained multi-layer perceptrons (MLPs) in an arbitrary number of optimizations for the fast evaluation of any design generated by the evolutionary routines. Notice this choice does not influence the precision of the design framework, since acceptable precision is reached with the regression nets. Also, well-defined Pareto fronts can be obtained with this workflow, as explained in Sec. V.

The built process uses the open-source scripting language `Python`, thus some technical details about it are reported in Sec. VI. Last, Sec. VII contains some ideas on how this work can be extended.

II. SYNCHRONOUS RELUCTANCE MOTORS

In SyR machines, torque is produced when the rotor attempts to align its most magnetically conductive axis with the stator rotating field in order to minimize the reluctance in the magnetic circuit. The reluctance discrepancy between the rotor axes is obtained by inserting

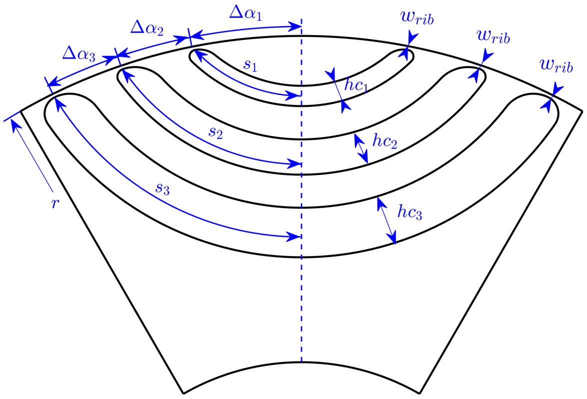

Fig. 2. Rotor parametrization of a SyR motors with optimization variables.

multiple pockets that however inflate the geometric complexity of the machine, Fig. 2. Indeed, to contemplate all the feasible geometries and detect the optimal one, numerous degrees of freedom have to be considered. Notably, optimization process have either a topological or parametric approaches. The first decompose the motor figure in tiny elements that are added or removed with an ON/OFF methods [5]; while, the latter parameterize the drawing with specific geometry parameters that allows to introduce certain degrees of freedom [2].

In SyR-e, the motor design is parameterized and the geometric feasibility assessed. Some of the rotor geometric parameters are displayed in Fig.2. In particular, the angular positions $\Delta\alpha$ and the thickness h_c of the flux barriers affect significantly the performance of the machines, as torque and torque ripple, which are usually calculated by time-consuming simulations. In the presented analysis, the barriers thickness (h_c) and positions ($\Delta\alpha$) are varied, however further degrees of freedom can be added and this will be object of future works. Since 3-barriers rotors are considered, 6 geometric variables are investigated. Moreover, each machine is evaluated in its optimal working point in terms of produced torque at a fixed current amplitude; this is defined as the maximum torque per ampere (MTPA) locus. The optimal operating point detection is implemented by introducing a 7^{th} variable, the phase current angle.

The most adopted method to assess a SyR motor is a FEA simulation. In SyR-e, magneto-static 2D FEA are launched in FEMM [4] with sequenced rotor positions, thus avoiding the even more time-consuming transient FEA. Moreover, the geometric symmetry is exploited by simulating one machine pole, while the electric symmetry is used by spanning a submultiple of the electric period. Then, the simulations provide representative quantities essential to assess the motor behavior such as the flux linkage, power factor, average torque and its ripple. Despite the computational time minimization, a standard FEA takes around 2 minutes with the reference workstation (Intel Xeon E5-2690 v4 CPU, 14 cores and 32GB RAM). Therefore, assuming a standard optimization process with 60 generations of 60 elements, the computational time is lengthy and takes around 10 hours. That said, introducing surrogate models in such a process can hugely shrink the computational time, as demonstrated in the following sections.

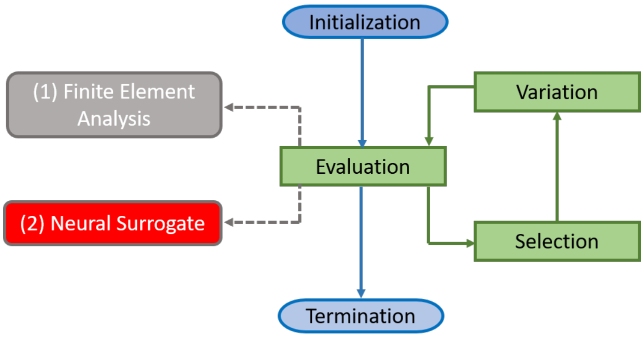

Fig. 3. Surrogate integration in general evolutionary schema.

III. OPTIMIZATION PROBLEM

In the optimization process, two-objectives are investigated: maximizing motor torque T and minimizing ripple ΔT.

$$\min_{x} \left(-T(x), \Delta T(x)\right); \tag{1}$$

where x is the 7-dimensional vector that defines the motor model:

$$x = [\Delta\alpha_1, \Delta\alpha_2, \Delta\alpha_3, h_{c_1}, h_{c_2}, h_{c_3}, \gamma], \tag{2}$$

where

- $\Delta\alpha_j$, $j = 1, 2, 3$, determine barrier positions;
- h_{c_i}, $i = 1, 2, 3$, represent thickness of each barrier;
- γ is the current angle.

See Fig. 2 for a graphical representation of the main variables which concurrently determine the geometry of a rotor. Note that this optimization setting is rather simplified: a limited number of variables is considered, while in principle many other d.o.f. determine the behavior of a SyR motor. Many of these variables are indeed considered in the SyR-e platform.

Also notice that the torque sign is swapped. This convention is chosen for the sake of the optimization process, because minimizing both objectives (in a bi-objective optimization problem) is equivalent to searching for points in the south-west region of the objective space.

In order to solve (1) the NSGA-II is adopted, consistently with what happens in the original optimization framework. This algorithm was proven effective in previous work on electrical machines [2], as well as in several other engineering applications [3] and thus no further tests were performed with other optimization methods. Having made this premise, the same surrogate models could be introduced in any evolutionary algorithm schema. As shown in Fig. 3, population-based optimizers feature a clear distinction between evaluation phase

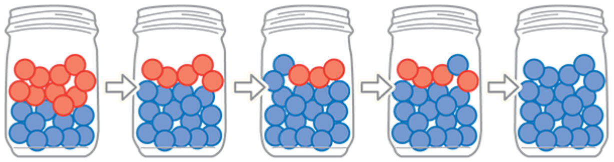

Fig. 4. Oversimplified visualization of genetic drift. From generation to generation, ”fake” near-optimal solution can suppress population diversity.

(where FEA can be replaced with surrogate models) and population transformation phases (typically, variation and selection for reproduction). A surrogate model can thus be embedded in any evolutionary algorithm by simply using the approximator as a fitness function. Despite this straightforward possibility, one should pay attention to an issue known as *drifting*. In general, strong selection pressure can prevent convergence to near-optimal solutions in a genetic algorithm (or other population-based methods); see Fig. 4 for a simple visual example. In particular, when using a Machine-Learning-based fitness function, this phenomenon can be more severe as model overfitting tends cause the generation of extreme-valued outputs [6]. Such outlying responses can drive evolution to unwanted areas, as the optimization algorithm is unaware of the likelihood of generated solutions.

This issue can indeed be tackled in surrogate setting by simply increasing population size: computational performance in only slightly affected in this case, as solution evaluation is always negligible when using statistical models. Obviously, also reducing selection pressure can reduce drifting. Weaker selection operators can be balanced with higher generation number.

More details on model fine-tuning are given in the following section.

IV. NEURAL SURROGATES

The proposed system uses what is known in literature as neuro-genetic optimization [7] to output the desired motor design. Letting aside the optimization modules, we employ Artificial Neural Networks (ANNs) to replace the 2D-FEM-based component evaluation. Our idea consists in adopting techniques from Deep Learning (DL) in order to implement an efficient and accurate interpolation model, that is two MLPs, one for each objective considered in optimization: torque T and torque ripple ΔT. Doing the math our objective is realizing neural surrogates that map the design space X to the performance space Y [7]:

$$T, \Delta T : X \longrightarrow Y. \tag{3}$$

Provable neural network theory shows that MLPs are universal approximators [8], which means MLPs, as long as enough neurons (i.e. computational units) are provided, have in principle enough learning capacity to approximate any given function. This classical result, however, gives us neither indications on how to build the model, nor on how to make the desired model computationally efficient. Luckily, DL from which we are drawing inspiration can be thought as a collection of techniques to address these issues and build effective neural networks.

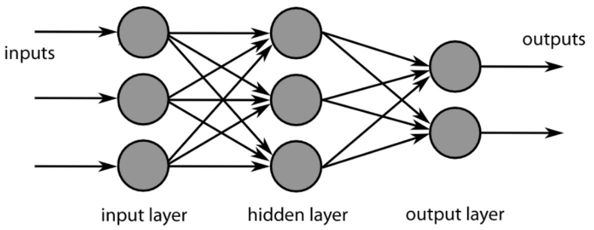

Fig. 5. Topology of a simple Multi-Layer Perceptron. This is a type of feed-forward neural network, in that information flows in a single direction from input to output. No feedback mechanism is present.

In fact, the deep MLP can be regarded as the contemporary version of this extremely classic neural architecture, which is extended to a many-layer topology. Recall that these models should be intended as function approximation machines designed to achieve statistical generalization by learning features from raw data, rather than abstractions of biological nervous systems. In fact, bio-inspired features like sigmoid activation functions are abandoned in favor of Rectified Linear Units (ReLU), as shown in Fig. 6.

With these design choices, deep MLPs results to be more sample efficient and faster to train if compared to shallow architectures. For a fixed number of neurons (i.e. non-linearities), a deep structure features a lower number of trainable weights and this is equivalent to decreasing the number of *degrees of freedom* (d.o.f.) in learning if we regard it as optimization problem. See Fig. 7 for a simple visual example of this fact. Furthermore, ReLU activations speed up computations and prevent saturation in gradient-based training: a ReLU is piecewise linear, its derivative is piecewise constant and hence it is faster (constant, $O(1)$) to compute. The constant derivative also prevents the vanishing gradient problem (saturation), that often affects sigmoidal activations.

Training data were generated using FEMM [4], the same software used in SyR-e. More precisely, the design matrix X, consisting of 5000 samples, was created using Latin Hypercube Sampling (LHS) over technically reasonable

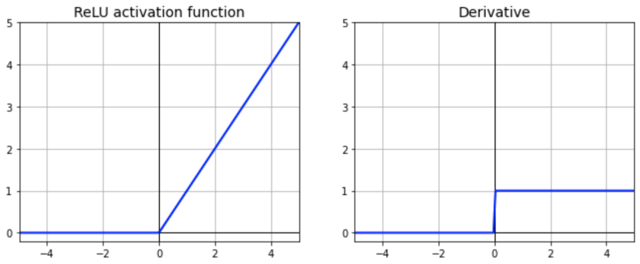

Fig. 6. ReLU activation (left) and its derivative (right).

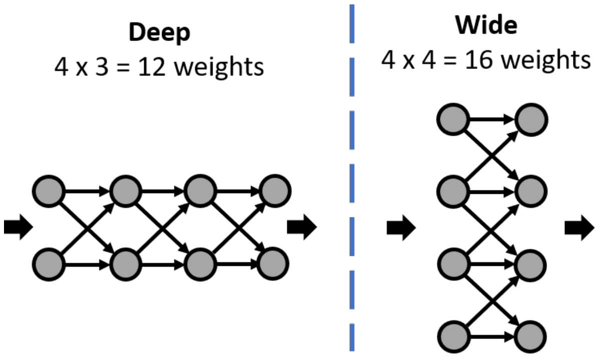

Fig. 7. Consider two neural networks with fixed number of neurons equal to 8. Th deep architecture (left) features 12 trainable weights against the 16 present in the "wide" topology (right).

Hyperparameter	Torque Model	Ripple Model
Number of hidden layers	12	7
Total number of neurons	139	78
Batch size	32	32
L^2-Regularization (α)	10^{-6}	10^{-6}

TABLE I
HYPERPARAMETERS USED IN SURROGATE MODELS.

ranges for each variable:

- $h_{c_i} \sim \mathcal{U}(0.1, 0.5)$;
- $\Delta\alpha_j \sim \mathcal{U}(0.1, 0.5)$;
- $\gamma \sim \mathcal{U}(55, 70)$.

FEMM software then produced the corresponding matrix of objectives Y, each row i of which gives (negative) torque and ripple:

$$Y_i = [-T(x_i), \Delta T(x_i)]\,, \tag{4}$$

where x_i denotes a vector of variables.

FEA-based techniques are nowadays very accurate and these values, despite not being real measurements, can be considered as a good reference for building surrogates. The whole process required around 8 hours using an 14-core Xeon workstation. 10% of the data were retained as test set.

For both neural networks, training was performed using Adam, a popular gradient-based optimizer, with default settings [9]. At each iteration, 10% of the (training) data were employed as validation set.

The two models also share the data preprocessing step, that simply consists in rescaling each feature linearly to the range $[0, 1]$.

After a preliminary exploration phase, for both objectives we performed *Grid Search* in order to find out the neural network topology (i.e. the number of hidden layers and the number of neurons in each layer) and the best combination of the following hyperparameters:

- Training batch size B;
- L^2-Regularization parameter α (greater is stronger).

Resulting topologies are different and Table I shows model details. Despite training was conventionally performed using the Mean Squared Error (MSE), we preferred using the Mean Absolute Percentage Error (MAPE) for the final evaluation of both models. MAPE is in fact easily interpretable, an highly desirable characteristic in any engineering application.

The MLP used to predict torque values showed excellent performance:

- $MAPE_{train} = 3.6\%$;
- $MAPE_{test} = 3.9\%$.

The low difference between train and test error, both very low, shows no significant improvement can be done (see Chap. 11 of [8] for an extensive discussion) with this architecture. Actually, further increase the learning capacity, e.g. by adding more layers, would probably reduce errors but that would be a symptom of overfitting, which could in turn cause drift during genetic optimization. An empirical threshold of 5% is typically considered in these applications [2], so there is no reason for pursuing an increase in performance. Error distributions confirm the previous considerations: Fig. 8 and Fig. 9 give (empirical) density and cumulative MAPE distributions, respectively.

Modeling the phenomenon of ripple was more difficult with respect to that of torque, having fixed the same dataset. In this case Grid Search led to an architecture whose performance can be summarized as follows:

- $MAPE_{train} = 12.1\%$;
- $MAPE_{test} = 12.3\%$.

Also in this case train and test error metrics are similar, but high. Notice here the automatic hyperparameter tuning procedure chose a topology with less layers (and neurons) w.r.t the MLP used for torque. This clearly indicates a tendency to overfit the data, that probably have poor distributional properties. Rebuilding a training dataset with Monte Carlo sampling techniques (e.g. Rejection Sampling) could help achieve better performance. The

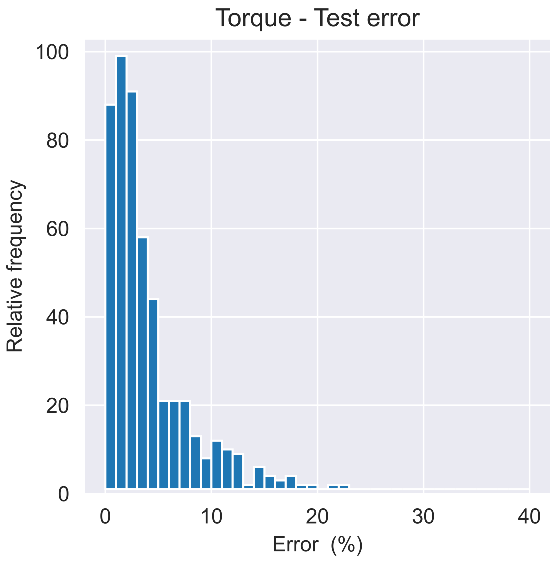

Fig. 8. Test error distribution over 500 samples. Performance of the model is good and compliant with empirical rule-of-thumbs.

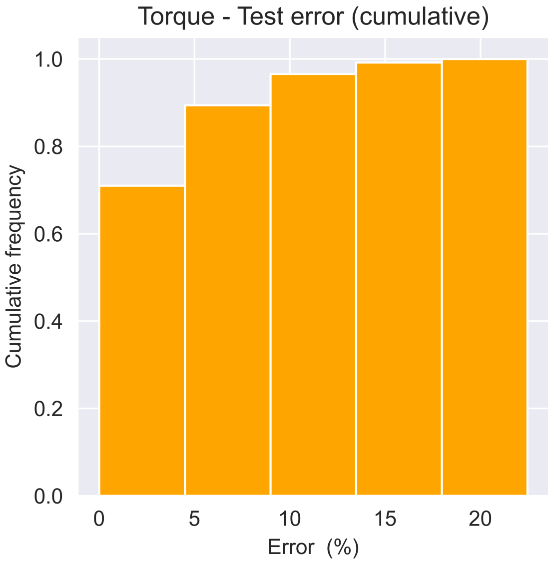

Fig. 9. Cumulative test error distribution over 500 samples. Roughly 90% of predictions show error below 10%.

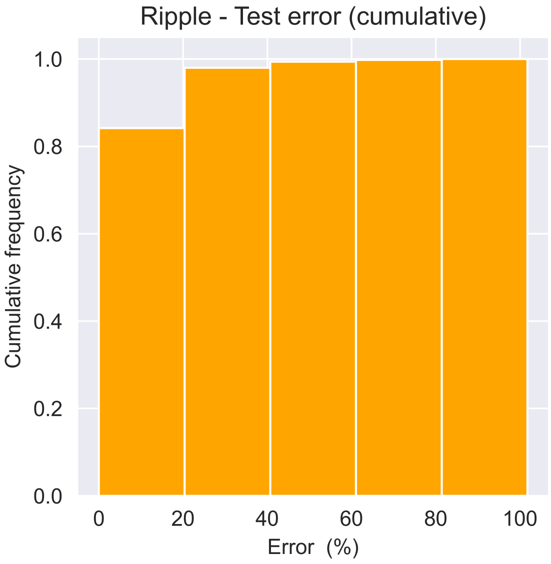

Fig. 11. Test error distribution over 500 samples. The presence of high-error observations confirms the presence of overfitting.

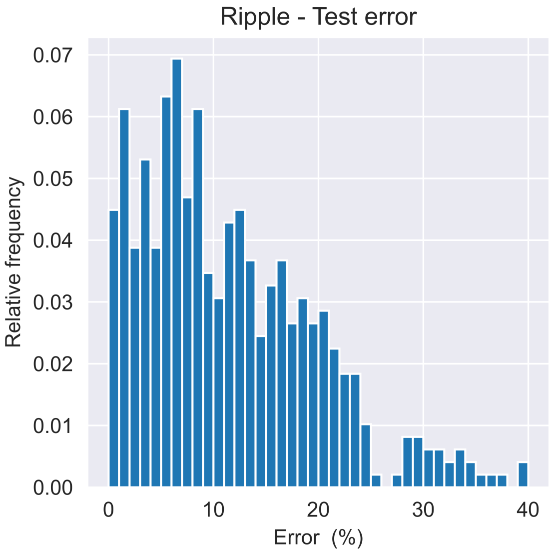

Fig. 10. Cumulative test error distribution over 500 samples. We can observe a tendency to generate outlying predictions.

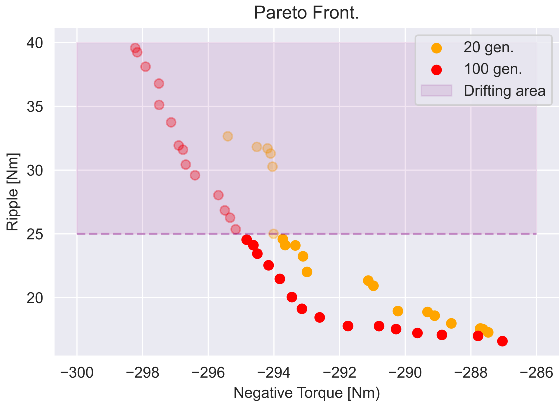

Fig. 12. Pareto front evolution after 20 and 100 generations.

presence of several outlying predictions, which can be observed graphically in both Fig. 10 and Fig. 11 confirms these concerns.

V. RESULTS

Here we discuss some preliminary optimization results. Consider Fig. 12: it shows the evolution of the Pareto front one can generate with the proposed solution. In particular, this figure shows the (near-)optimal solutions obtained after 20 and 100 generations for a population of 30 individuals.

When comparing our surrogate-based workflow to the simulation-based procedure of SyR-e, the most evident difference is execution time: an NSGA-II runs with FEMM evaluations requires around one minute for each function call. Doing elementary maths, this means that evaluating 30 different solutions for 20 generations roughly requires $30 \times 20 = 600$ minutes (i.e. 10 hours).

A surrogate-based fitness function call is so fast that greatly increasing the number of generations, as well as population size, does not really influence execution time: all simulations required less than one minute. This allows us to obtain better-defined Pareto fronts with essentially the same computation effort. Also, having negligible evaluation time allows us to reduce selection pressure in optimization algorithms, thus reducing the risk of premature convergence to local minima. On the contrary, we saw no reason to increase population size above 30 individuals, as this size ensures enough diversity and a well-defined Pareto front.

Also notice the violet area in the plot: it denotes areas of the objective space where drifting occurs with high probability. As stated in previous sections, this is probably due to (ripple) model overfitting, as values above 25 Nm can be considered unrealistic for the problem of interest, according to the domain-specific knowledge of experts in our research group. Having made this premise, classical multi-objective optimization theory states that best solutions are found around the "elbow" of the Pareto front, so that there is no need to worry about solutions in that area.

VI. TECHNICAL DETAILS

Despite SyR-e is Matlab-based, we preferred sticking to Python for developing the experimental software. Python is in fact more versatile when coming to non-numerical computations, as it offers all benefits of a scripting language plus a wide variety of ready-to-use, open-source quantitative tools. More precisely, we employed the following libraries:

- `sklearn`, a very popular Machine Learning library [9], to implement neural networks;
- `pymoo`, a recent multi-objective optimization suite [10] based on the template programming paradigm.

As expected, we managed to greatly increase computational performance. A single FEMM simulation takes around one minute on a 14-core Xeon workstation, while a complete, surrogate-based optimization procedure requires less than 10 seconds. Despite the surrogates give the main contribution, this also depends on the code quality of `pymoo`, whose units are optimized for parallel execution.

Letting aside the quantitative parts of the code, Python was found to be extremely handful in managing the serialization/deserialization of the objects representing the learning models we used. In fact. Python provides an extremely intuitive built-in library for this purpose: `pickle`.

VII. DISCUSSION AND FINAL REMARKS

This works should be intended as a work-in-progress contribution: our aims were assessing the feasibility of surrogate-based optimizers for SyR motors and understanding the technical guidelines developers should follow when creating approximators of this type.

We obtained encouraging preliminary results, especially if we consider the tradeoff between (limited) training data availability, accuracy and required execution time. We now aim at increasing model performance, by extending the training set, especially for the case of ripple. In particular, we firmly believe having a dataset with better distributional properties would significantly reduce prediction errors. Moreover, recent research [11] shows that ensemble methods perform particularly well in surrogate-assisted evolutionary algorithm. In other words, several surrogate submodels can be trained under different search subspaces to exploit the subarea, so as to reduce the presence of outlying predictions and increase global robustness of the model.

As for the technicalities involved in building effective neural surrogates, we understood that even simple models (i.e. with limited number of neurons), if properly tuned, can perform well in these applications, hence allowing the creation of software with low resource requirements. We also plan substituting the gradient based optimizer Adam with zeroth order optimization methods, as instability was observed by our group as well as by influential research institutions [7].

Finally, the goal is to extend this work to different SyR motor topologies (e.g. by including more optimization variables), as well as to different types of electrical machines.

REFERENCES

[1] F. Cupertino and G. Pellegrino, "SyR-e: Synchronous Reluctance (machines) - evolution." [Online]. Available: www.github.com/SyR-e

[2] F. Cupertino, G. Pellegrino, and C. Gerada, "Design of synchronous reluctance motors with multiobjective optimization algorithms," *IEEE Transactions on Industry Applications*, vol. 50, no. 6, pp. 3617–3627, 2014.

[3] K. Deb, A. Pratap, S. Agarwal, and T. Meyarivan, "A fast and elitist multiobjective genetic algorithm: Nsga-ii," *IEEE Transactions on Evolutionary Computation*, vol. 6, no. 2, pp. 182–197, 2002.

[4] D. Meeker, "FEMM: Finite Element Method Magnetics." [Online]. Available: www.femm.info

[5] S. Sato, T. Sato, and H. Igarashi, "Topology optimization of synchronous reluctance motor using normalized gaussian network," *IEEE Transactions on Magnetics*, vol. 51, no. 3, pp. 1–4, 2015.

[6] R. T. T. Hastie and J. Friedman., "Springer series in statistics springer new york inc." 2001.

[7] T. Guillod, P. Papamanolis, and J. W. Kolar, "Artificial neural network (ann) based fast and accurate inductor modeling and design," *IEEE Open Journal of Power Electronics*, vol. 1, pp. 284–299, 2020.

[8] B. Y. Goodfellow, I. and A. Courville, "Deep learning." 2016.

[9] "Scikit-learn: Machine learning in python." [Online]. Available: https://scikit-learn.org/

[10] "Pymoo: Multi-objective optimization in python." [Online]. Available: https://pymoo.org/

[11] Q. Lin, X. Wu, L. Ma, J. Li, M. Gong, and C. A. C. Coello, "An ensemble surrogate-based framework for expensive multiobjective evolutionary optimization," *IEEE Transactions on Evolutionary Computation*, vol. 26, no. 4, pp. 631–645, 2022.

Influence of Earthing Systems on ERT Measurements

Benjamin Jauk*, Robert Schürhuber*, and Katrin Friedl*

*Institute of Electrical Power Systems, Inffeldgasse 18/1, A-8010 Graz
E-mail: Benjamin.Jauk@TUGraz.at

***Abstract*—Soil resistivity measurements need to be taken without any electrically conductive material nearby, e.g. fences, pipelines or earthing systems, otherwise the measurement would be affected by this conductive material. With this work we demonstrate the usage of the applied geophysical method ‘ERT’ (Earth Resistivity Tomography) for measurement and an inversion algorithm to create the inversion soil model in the vicinity of an earthing system.**

By using an appropriate geophysical inversion algorithm it is also possible to isolate the conductive structure and provide a good soil model for further earthing system design. It can be also seen that the orientation of the survey line to measure the apparent soil resistivity has a significantly influence on the measurement results.

***Index Terms*—Earthing Systems, Soil Resistivity Measurement, Applied Geophysics, Earth Resistivity Tomography**

I. INTRODUCTION

Earthing systems need to be properly designed to ensure personal safety. To ensure that, the knowledge of the soil resistivity is mandatory. [1] In electrical engineering soil resistivity measurements are often performed with a series of single 4-point measurements technique. This technique is called VES (Vertical Electrical Sounding). In those measurements the midpoint of the measurement is always at the same location, whereas the electrodes spacing will be increased. This measurement setup is also used for deep soil soundings in applied geophysics. A second electrical sounding method is ‘ERT’ (Earth Resistivity Tomography), which uses several electrodes, which are switched in a way, so that every possible configuration is used. [2]

In both cases the result of the measurement is the so called ‘apparent resistivity’. The apparent resistivity is used as an input parameter for the inversion procedure to get the soil resistivity to build the soil model for the earthing system design.

Using single 4-point measurements (VES) near metallic structures is shown in [3], [4]. However, in this work we further investigate the behaviour of such measurements, by using ERT (Earth Resistivity Tomography) technique in “Wenner Array” configuration, as depicted in Fig. 3. Which provides, due to the switching of the electrodes more data for the inversion procedure, since 2D data is available.

II. METHODOLOGY

To show the behaviour of an ERT measurement near a earthing system, the following tasks are done, as shown in Fig. 1.

First, four synthetic soil model, with a size of $800 \times 800 \times 400\,\mathrm{m}$ are built:

- homogeneous soil without an earthing system
- homogeneous soil with an earthing system
- layered soil without an earthing system
- layered soil with an earthing system

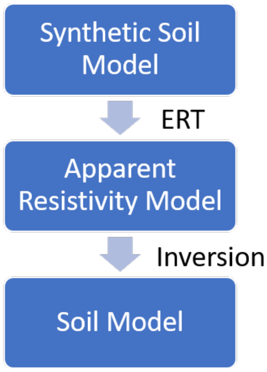

Fig. 1. Methodology

The electrodes (stainless steel rods), which are used for the ERT measurement are pushed into ground. To perform the ERT measurement 24 electrodes with $3\,\mathrm{m}$ spacing are used. The electrodes are switched in a way, so that every possible configuration of a Wenner Array (Fig. 3) out of this 24 electrodes can be generated. Therefore, the distance a, which is used in (1), will change its value, which is an integer multiple of $3\,\mathrm{m}$.

Further, the orientation of the survey line is changed as well, survey line ① (pointing away from the earthing system (parallel to the y-axis)) and survey line ② (parallel to the x-axis) as depicted in Fig. 2.

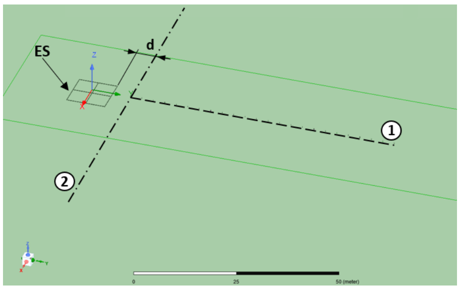

Fig. 2. FEM Model in ANSYS with the survey line: pointing away (1, dashed line) and parallel (2, dash-dotted line) to the earthing system (ES)

To analyze the influence on the measurement procedure, the distance ‘d’ between the earthing system and the survey line is varied from $0.1\,\mathrm{m}$ to $10\,\mathrm{m}$. The simulation is carried out in commercial FEM (Finite Element Method) software ANSYS Maxwell 3D in DC conduction mode.

The simulation result is the voltage at each electrode, since the current is the source. The apparent resistivity ρ_a is calculated, using ‘Wenner’s’ equation [1]; neglecting the depth of the electrodes, since the depth of the electrodes is less than $10\,\%$ of the distance a.

$$\rho_\mathrm{a} = 2\pi \cdot a \cdot \frac{U}{I} \tag{1}$$

Where ρ_a is the soil resistivity, a the distance between the electrodes, U the voltage between the inner electrodes P1-P2 and I the injected current C1-C2.

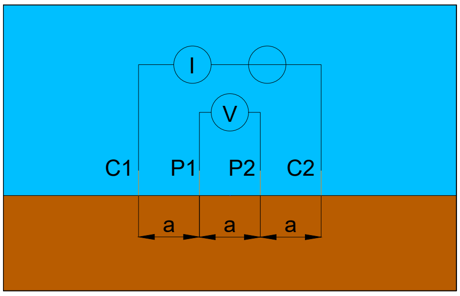

Fig. 3. Wenner Array

To show the influence of the earthing system in the apparent resistivity plots, the difference between both simulations is plotted as “delta apparent resistivity”. The calculation of the difference is basically the absolute error between both results:

$$\rho_{\Delta,\mathrm{a}} = \rho_{\mathrm{ES,a}} - \rho_\mathrm{a} \tag{2}$$

Where $\rho_{\Delta,\mathrm{a}}$ is the delta apparent resistivity, $\rho_{\mathrm{ES,a}}$ is the apparent resistivity with the earthing system, ρ_a is the apparent resistivity without the earthing system.

To create the soil model, the apparent resistivities are passed to the inversion software “pyGIMLI” (Python Geophysical Inversion and Modelling Library) to create the soil model. The inversion is a minimization problem consisting of data misfit and model constraints, solved with a Gauss-Newton algorithm [6]:

$$||\mathbf{W}_\mathrm{d}(\mathcal{F}(\mathbf{m}) - \mathbf{d})||_2^2 + \lambda||\mathbf{W}_\mathrm{m}(\mathbf{m} - \mathbf{m}_0)||_2^2 \rightarrow \min \tag{3}$$

Where $\mathbf{W}_\mathrm{d}$ is the data weighthing matrix, $\mathbf{W}_\mathrm{m}$ is the model constraint matrix, $\mathbf{m}_0$ is the reference model, λ is the scale of the regularization.

Since the place and size of the earthing system is known, this information can be provided to the inversion algorithm. In all cases the earthing system is represented as a line geometry.

III. RESULTS

Fig 4 depicts both survey lines at a distance of $0.1\,\mathrm{m}$ to the earthing system. The results for the closest distance ($d = 0.1\,\mathrm{m}$) show for both survey lines the biggest deviation. The deviation decreases for greater distances. If the earthing system is present, the values for the apparent resistivity are in general lower than without the earthing system.

The inversion result of survey line ① as shown in Fig. 5 has a better match with the synthetic model compared to the survey line ② in Fig. 6.

Heading forward now to the inversion result for survey line ② (dash-dotted line in Fig. 2), the result (Fig. 6, middle) shows a large deviation compared to the synthetic model (Fig. 6, top). However, when adding the line, the inversion result shows a better match with the synthetic model than without, as depicted in Fig. 6, bottom.

IV. CONCLUSION

With both survey lines it is possible to create a good soil model under these circumstances. However, survey line ① (pointing away from the earthing system), is less influenced than survey line ②. This means that more inversion effort is required for survey line ② to obtain a high quality soil model.

In addition, each result can be considered as a whole cross-section of the investigated area, as the ERT method provides data for 2D diagrams, in contrast to VES, which has only one resistivity value at a certain depth and therefore only provides a 1D diagram.

However, the soil resistivity values do not correspond to the actual values. This means that for correct values, as far as they can be found during this process, further information has to be passed to the inversion software, e.g. dimension and resistivity value of the disturbance. This has been done, represented by the line geometry, at least for its thickness. But as already mentioned, this requires knowledge and dimension of the disturbance zone, otherwise the measurement will be affected accordingly. On the other hand, the designer must be aware that a natural disturbance zone (e.g. local rock alteration) must also be taken into account according to its thickness, as it has an influence on the final earthing system.

With geophysical methods such as this ERT method and the inversion algorithm, it is possible to create a robust inversion model. This inversion model can then be used to create the soil model for the design of the earthing system. It is then at the discretion of the user whether a homogeneous, layered or even an inhomogeneous model is used for the design phase.

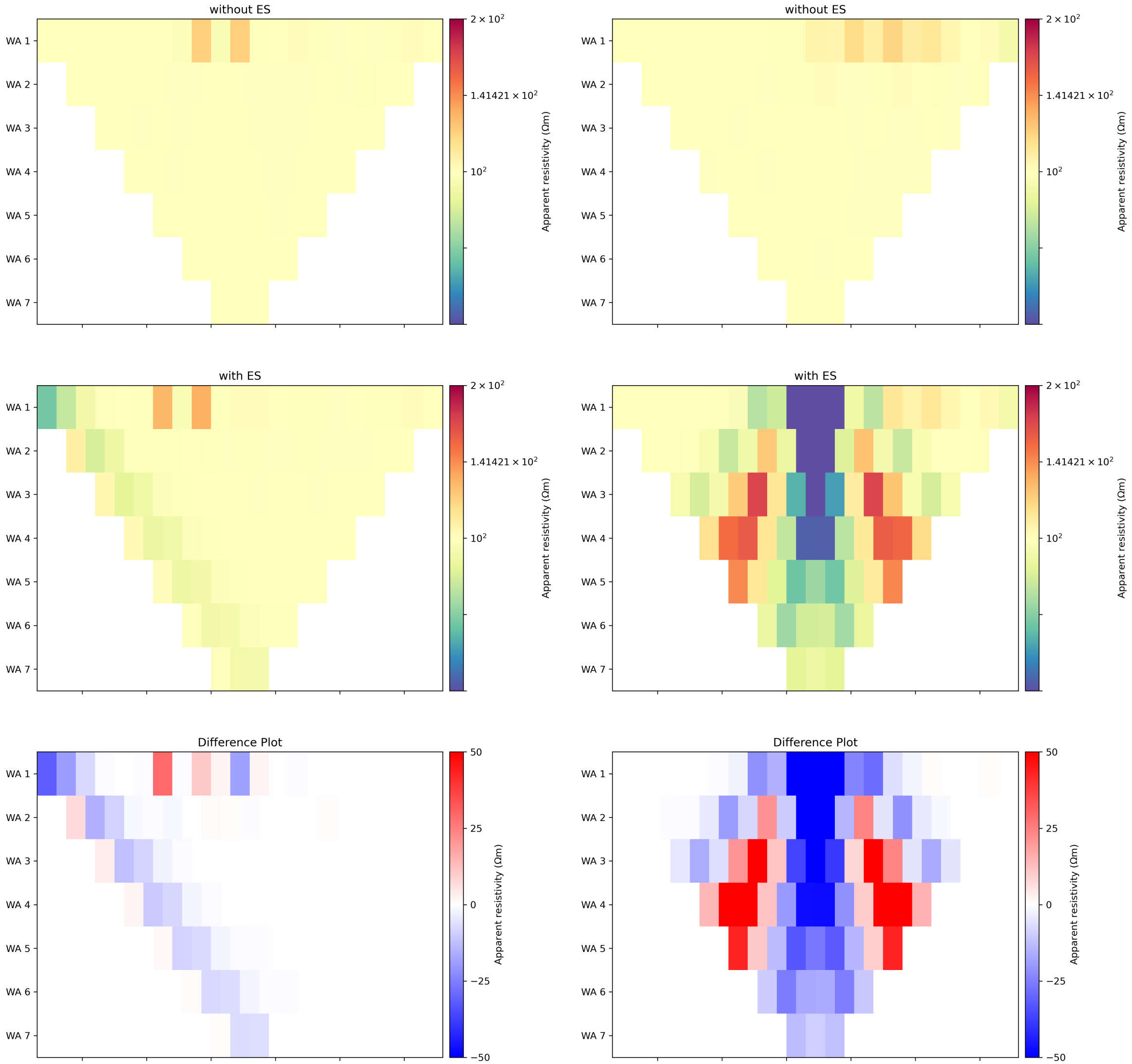

without ES

without ES

with ES

with ES

Difference Plot

Difference Plot

Fig. 4. Plots for distance $d = 0.1\,\mathrm{m}$
Left: Survey line ① (pointing away) without earthing system (top), with earthing system (middle) and the difference plot (bottom)
Right: Survey line ② (parallel) without earthing system (top), with earthing system (middle) and the difference plot (bottom)

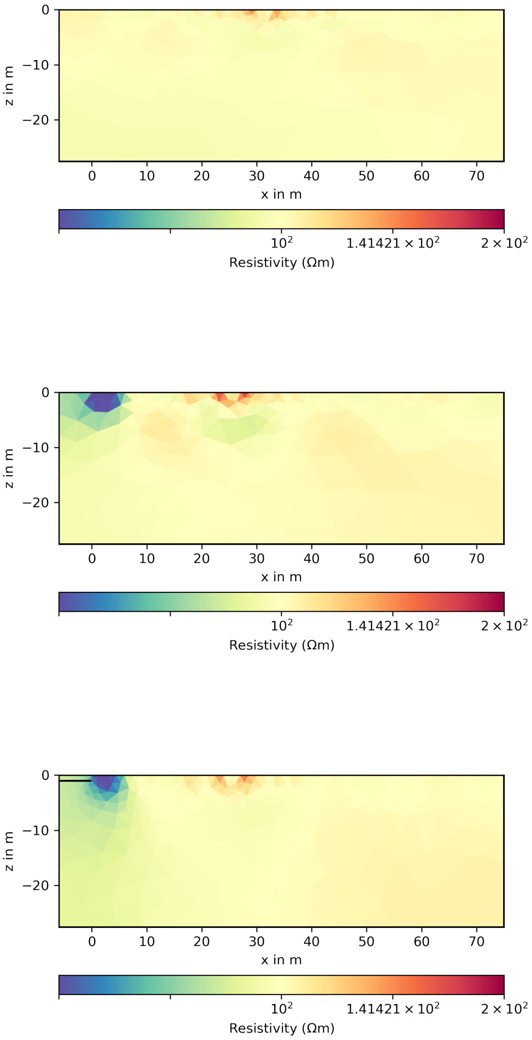

Fig. 5. Inversion result of the apparent resistivity distribution of survey line ① at a distance of $0.1\,\mathrm{m}$ - without the earthing system (top), with the earthing system (middle), with earthing system and line geometry (bottom)

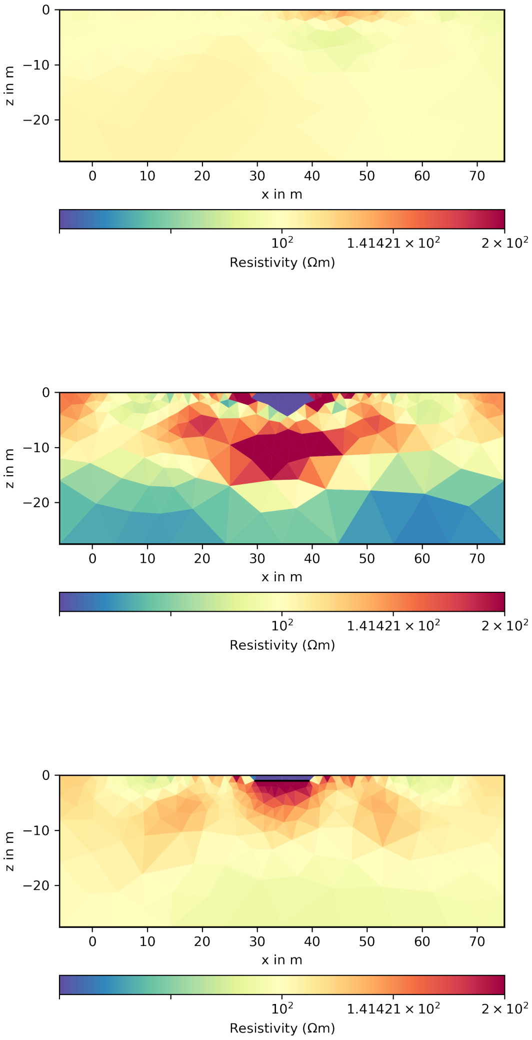

Fig. 6. Inversion result of the apparent resistivity distribution of survey line ② at a distance of $0.1\,\mathrm{m}$ - without the earthing system (top), with the earthing system (middle), with earthing system and line geometry (bottom)

REFERENCES

[1] “IEEE Guide for Measuring Earth Resistivity, Ground Impedance, and Earth Surface Potentials of a Grounding System”, IEEE 2012

[2] A. Eriksen and J. Milsom, “Field Geophysics, Fourth Edition”, John Wiley and Sons Ltd. 2011

[3] J. Ma and F. P. Dawalibi, “Study of influence of buried metallic structures on soil resistivity measurements”, IEEE Trans. on Power Delivery, pp. 356-365, Vol. 13, N. 2, 1998

[4] A. M. Silva and Mandar D. Kavimandan, “Analytical Method for Eliminating the Impact of External Interference on Soil Resistivity Measurements”, IEEE PES General Meeting, pp. 1-5, 2020

[5] M. H. Loke, “Tutorial: 2-D and 3-D electrical imaging surveys”, Loke Oct. 2019

[6] Rücker, C., Günther, T., Wagner, F.M., 2017. pyGIMLi: An open-source library for modelling and inversion in geophysics, Computers and Geosciences, 109, 106-123, doi: 10.1016/j .cageo.2017.07.011.

Symmetric LF-Stable Electromagnetic Quasistatic A-V Formulation for Eddy-Current Problems

*† Zsolt Badics and *József Pávó
*Department of Broadband Infocommunications and Electromagnetic Theory, Budapest University of Technology and Economics, 1111 Budapest, Műegyetem Rkp. 3., Hungary
†Tensor Research, LLC, 100 Wildwood Rd., Andover, MA, U.S.A.
E-mail: zbadics@tensorresearch.com

***Abstract*—A finite-element EMQS (electromagnetic quasistatic), aka Darwin, A-V formulation is developed for solving eddy-current problems in which the computation of the capacitive effects is required. To obtain a symmetric system, the formulation incorporates an additional scalar variable in the conducting regions. An important further advantage of the formulation is that it is low-frequency stable – i.e., the solution is stable and correct when approaching the zero-frequency limit. Furthermore, the system matrix is regular so either a direct or iterative solver can be utilized for the solution of the discretized Galerkin system. The new EMQS solver is validated by solving two benchmark problems where the results are compared to computations by eddy-current and full-wave solvers. Run-time data is presented to illustrate the nature of the potential increase in the run-time costs compared to eddy-current solutions.**

***Index Terms*—Capacitive Effect, Darwin Approximation, Finite-Element Formulation, Low-Frequency Stability.**

I. INTRODUCTION

In modern LF (low-frequency) CEM (computational electromagnetics), design engineers often face numerical simulation problems in which the capacitive effects are essential part of the operation of high-technology magnetic devices. FE (finite element) eddy-current solvers are very efficient in analyzing LF components and systems with high-conductivity ($\sigma \gg \omega\varepsilon$) regions but they do not simultaneously calculate the capacitive effects [1]. It is possible to extract the resistive, inductive and capacitive effects by eddy current and electrostatic solvers separately, and utilize circuit simulation to solve such problems. This process, however, may become cumbersome and/or inaccurate. Thus, there are lots of merits in using only one field solver that incorporates all three aspects of a computational problem simultaneously while neglecting the radiation effect.

EMQS (electromagnetic quasistatic), a.k.a. Darwin, solvers carry such features. In the last decade, several EMQS formulations - including FE (finite element), FIT (finite integration) and IE (integral equation) techniques – have been published to solve EMQS models in the time and the frequency domains [2]-[13]. An excellent survey has been published recently in [14]. These solvers are needed more and more in analyzing some components in transformers, inductive wireless-power and other power electronic systems. The low-frequency stability can be important for EMQS time-harmonic solvers when performing frequency sweeps in order to identify resonances. Additionally, a symmetric discretized system is desirable to increase numerical efficiency.

We have previously developed a time-harmonic FE EMQS A-V formulation that has an unsymmetric LF-stable system matrix [4][8]. In this work, we develop a symmetric version of the formulation by utilizing a technique inspired by the idea developed for full-wave problems in [15]. We also show how the formulation can efficiently be adjusted to solve eddy-current problems.

In the next section, we describe the computational model that we base our equations on. Then, in *Section III*, we recall the basic features of some formulations that our discussion is built on and relates to. For that purpose, we show how to implement the current terminal in the eddy current formulation in *Subsection III.A.1)* but omit such discussion for the subsequent formulations. Next, we introduce our new formulation in *Section IV*. Then, we validate the formulation in *Section V* by solving two benchmark problems with comparisons of outputs and run-time performances to established solution technologies. We draw some conclusions in *Section VI.*

II. COMPUTATIONAL MODEL

A. Model Problem

In Figure 1, we depict a model problem that is simple but adequate enough to support the explanation of all major aspects of our new formulation. On the other hand, the model is generic enough to allow the application of the formulation to any consistent excitations and BCs (boundary conditions). We consider only linear reciprocal material tensors, but ε and μ may be complex in general, which means that Ω_N can also contain dielectrics that have frequency-proportional losses. To simplify the equations, we set the boundary condition to PMC (perfect magnetic conductor) on Γ_H. We assume that the EM field is generated by a solenoidal impressed current desnity $\vec{J}_S$ located in Ω_N, and a terminal current source I_T exiting Ω_C through the terminals Σ^+ and Σ^-.

B. EMQS Approximation

In most EMQS computational models, the EMQS approximation means that only the irrotational part of the electric field is contributing to the displacement current in the Ampère's law [16][17]. Hence, the electric field is split as

$$\vec{E} = \vec{E}^g + \vec{E}^c \tag{1}$$

where the irrotational part $\vec{E}^g$ satisfies

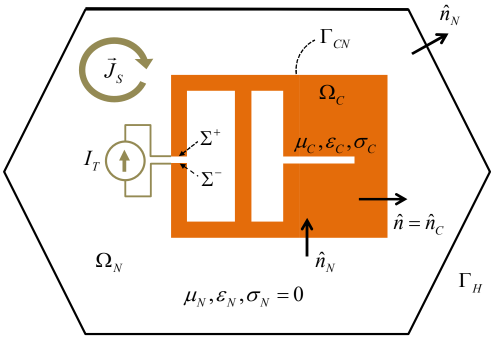

Fig. 1. Schematic arrangement of the model problem. The computational region Ω is divided into two non-overlapping regions: Ω_C with $\sigma \neq 0$, and $\Omega_N = \Omega \setminus \Omega_C$ with $\sigma = 0$. Interface Γ_{CN} separates Ω_C and Ω_N, while the closed outer boundary is $\partial\Omega = \Gamma_H$.

$$\nabla \times \vec{E}^g = \vec{0} \tag{2}$$

$$\rho - \nabla \cdot \vec{D}^g = 0 \tag{3}$$

$\vec{E}^c$ is the complementary part of the electric field, and ρ denotes the free volume charge density due to the spatial variation of electric conductivity σ. The irrotational part can be represented by the gradient of the electric scalar potential $\vec{E}^g = -\nabla V$ due to the requirement (2).

With (1), the EMQS Ampère's law takes the form

$$\nabla \times \vec{H} - \vec{J}_C - j\omega\vec{D}^g = \vec{J}_S \tag{4}$$

where $\vec{J}_C = \sigma\vec{E}$. The remaining Maxwell's equations are unchanged but we list them here for completeness:

$$\nabla \times \vec{E} + j\omega\vec{B} = 0 \tag{5}$$

$$\nabla \cdot \vec{B} = 0 \tag{6}$$

$$j\omega\rho + \nabla \cdot \vec{J}_C = 0 \tag{7}$$

$$\rho - \nabla \cdot \vec{D} = 0 \tag{8}$$

Summing up, the full set of the EMQS Maxwell's equations is (2)-(8), which means that the equations for the irrational part (2) and (3) have to be incorporated – explicitly or implicitly – into any EMQS formulation.

III. PRELIMINARIES

In this section, we introduce several concepts that are involved in deriving the symmetric EMQS formulation in *Section IV*, and in comparing it to eddy-current solvers.

A. Eddy-Current A-V Formulations

A large repository of technical articles on different eddy-current formulations have been published in the last several decades. A splendid summary of some of the most efficient formulations can be found in [1]. Here, we discuss only the unsymmetric and symmetric version of the A-V,A formulation. The name implies that the fundamental variable in Ω is the magnetic vector potential $\vec{A}$, while the electric scalar potential V is utilized only in Ω_C.

Let us gather first the governing Maxwell's equations for typical eddy current arrangements [1]. Since the conductors in eddy-current problems are high-conductivity metal regions, the displacement currents are completely negligible. Therefore, (4) in Ω_C becomes

$$\nabla \times \vec{H} - \vec{J}_C = 0 \tag{9}$$

and the free charges in (7) and (8) can be omitted so only

$$\nabla \cdot \vec{J}_C = 0 \tag{10}$$

is relevant. Hence, the governing equations in the conductors are (9), (5), (6) and (10).

In Ω_N, we only interested in the magnetic field so (4) is simplified further as

$$\nabla \times \vec{H} = \vec{J}_S \tag{11}$$

Thus, the governing equations in Ω_N are (11) and (6).

1) Unsymmetric LF-Stable Formulation

The standard way to introduce the vector potential in the whole domain is to satisfy (6) exactly by

$$\vec{B} = \nabla \times \vec{A} \tag{12}$$

The electric scalar potential is introduced only in Ω_C as

$$\vec{E} = -j\omega\vec{A} - \nabla V \tag{13}$$

In order to consider the current terminal excitation, we write the scalar potential in the form of

$$V = \Phi + U_T\varphi \tag{14}$$

where U_T is the terminal voltage, and φ is the so-called geometrical basis function that is the solution of the Laplace equation with zero normal derivative on Γ_{CN}, and with $\varphi = 1$ and $\varphi = 0$ prescribed on Σ^+ and on Σ^-, respectively [18][19].

We substitute (12) and (13) into (9)-(11) in order to obtain the governing equations whose weak forms are

$$\begin{aligned}\int_{\Omega} \nu\nabla \times \vec{A} \cdot \nabla \times \vec{A}' dv + \int_{\Omega_C} \left(j\omega\sigma\vec{A} \cdot \vec{A}' + \sigma\nabla V \cdot \vec{A}' \right) dv \\ = \int_{\Omega_N} \vec{J}_S \cdot \vec{A}' dv\end{aligned} \tag{15}$$

$$\int_{\Omega_C} j\omega\sigma\vec{A} \cdot \nabla\Phi' dv + \int_{\Omega_C} \sigma\nabla V \cdot \nabla\Phi' dv = 0 \tag{16}$$

$$\int_{\Omega_C} j\omega\sigma\vec{A} \cdot \nabla\varphi' dv + \int_{\Omega_C} \sigma\nabla V \cdot \nabla\varphi' dv = -I_T \tag{17}$$

where $\vec{A}'$ and Φ' are admissible weighting functions, and φ' is a weighting function satisfying the same conditions as φ in (14). In the weak forms, we weakly satisfy the PMC BC on Γ_H in (15), and $\vec{J}_C \cdot \hat{n} = 0$ on Γ_{CN} in (16) and (17). We also incorporate the current terminal excitations on Σ^+ and Σ^- by adding φ to the scalar potential. Note, that the tangential component of $\vec{E}$ and the normal component of $\vec{B}$ are satisfied strongly due to the fact that $\vec{A}$ is tangentially continuous in Ω.

The next step in the Galerkin discretization process is to choose approximation functions for $\vec{A}$ and V in a tetrahedral tessellation:

$$\vec{A} \approx \vec{A}^h = \sum_{k=1}^{N_A} A_k \vec{\alpha}_k \tag{18}$$

$$V \approx V_C^h = \sum_{m=1}^{N_C} V_m \beta_m + U_T \varphi^h = \sum_{m=1}^{\tilde{N}_C} V_m \beta_m \tag{19}$$

where $\vec{\alpha}_k$ denote hierarchical TVFEs (tangential vector finite elements) [20]; $\{\beta_m | m = 1,...,N_C\}$ are consistent hierarchical scalar finite elements; and $\beta_{\tilde{N}_C} = \varphi^h$ (a discretized form of φ) with $\tilde{N}_C = N_C + 1$. Note, that φ^h can be constructed in advance by solving the Laplace problem with approximation functions β_m's. N_A is the number of TVFEs on Ω, while N_C is the number of scalar FE approximation functions β_m whose supports are nonzero only in Ω_C and on Γ_{CN}. Further, A_k and $\{V_m | m = 1,...,N_C\}$ are unknown complex coefficients, and $V_{\tilde{N}_C} = U_T$ is the unknown terminal voltage.

After substituting (18) and (19) into (15)-(17), and using $\vec{\alpha}_i$'s and β_m's as the set of weighting functions in (15)-(17), we arrive at a linear system

$$\begin{bmatrix} \mathbf{S}_\nu^{AA} + j\omega \mathbf{T}_\sigma^{AA} & \mathbf{M}_\sigma^{AC} \\ j\omega \left(\mathbf{M}_\sigma^{AC}\right)^T & \mathbf{K}_\sigma^{CC} \end{bmatrix} \begin{bmatrix} \mathbf{x}_A \\ \mathbf{x}_V^C \end{bmatrix} = \begin{bmatrix} \mathbf{b}_S^A \\ \mathbf{b}_T^C \end{bmatrix} \tag{20}$$

where $\mathbf{x}_A$ is column vector of A_k, while $\mathbf{x}_V^C$ is the column vector of $\{V_m | m = 1,...,\tilde{N}_C\}$. Hence, for $i,k = 1,2,...,N_A$ and $n,m = 1,2,...,\tilde{N}_C$, the elements of the linear system are

$$\left[\mathbf{S}_\nu^{AA}\right]_{ik} = \int_\Omega \nu \nabla \times \vec{\alpha}_k \cdot \nabla \times \vec{\alpha}_i dv \tag{21}$$

$$\left[\mathbf{T}_\sigma^{AA}\right]_{ik} = \int_\Omega \sigma \vec{\alpha}_k \cdot \vec{\alpha}_i dv \tag{22}$$

$$\left[\mathbf{M}_\sigma^{AC}\right]_{im} = \int_{\Omega_c} \sigma \nabla \beta_m \cdot \vec{\alpha}_i dv \tag{23}$$

$$\left[\mathbf{K}_\sigma^{CC}\right]_{nm} = \int_{\Omega_\tau} \sigma \nabla \beta_m \cdot \nabla \beta_n dv \tag{24}$$

$$\left[\mathbf{b}_S^A\right]_i = \int_\Omega \vec{J}_S \cdot \vec{\alpha}_i dv \tag{25}$$

$$\left[\mathbf{b}_T^C\right]_n = \begin{cases} 0 & \text{if } n = 1,...,N_C \\ -I_T & \text{if } n = \tilde{N}_C \end{cases} \tag{26}$$

If we write down (20) for $\omega \to 0$ as

$$\begin{bmatrix} \mathbf{S}_\nu^{AA} & \mathbf{M}_\sigma^{AC} \\ \mathbf{0} & \mathbf{K}_\sigma^{CC} \end{bmatrix} \begin{bmatrix} \mathbf{x}_A \\ \mathbf{x}_V^C \end{bmatrix} = \begin{bmatrix} \mathbf{b}_S^A \\ \mathbf{b}_T^C \end{bmatrix} \tag{27}$$

we can easily see that the system matrix is LF-stable. The magnetostatic and the steady conduction problems decouple completely, so row 2 provides the steady conduction solution in Ω_C, and that solution serves as a current density excitation for the magnetostatic field in row 1 together with the solenoidal current density $\vec{J}_S$. Note, that the system matrix in (20) is unsymmetric.

2) Symmetric Formulation

We can make the system symmetric by modifying the definition of the scalar potential in (13) as

$$\vec{E} = -j\omega \vec{A} - j\omega \nabla V \tag{28}$$

which is the preferred choice in practice [1]. Using the potential definitions (12) and (28), we can obtain a symmetric linear system by following the procedure described in the previous subsection:

$$\begin{bmatrix} \mathbf{S}_\nu^{AA} + j\omega \mathbf{T}_\sigma^{AA} & j\omega \mathbf{M}_\sigma^{AC} \\ j\omega \left(\mathbf{M}_\sigma^{AC}\right)^T & j\omega \mathbf{K}_\sigma^{CC} \end{bmatrix} \begin{bmatrix} \mathbf{x}_A \\ \mathbf{x}_V^C \end{bmatrix} = \begin{bmatrix} \mathbf{b}_S^A \\ \mathbf{b}_T^C \end{bmatrix} \tag{29}$$

The blocks of the system are the same as defined for (20). As an advantage, the system is symmetric but we lose the LF stability: if $\omega \to 0$, row 2 in (29) approaches zero, which means that we lose control of *V* and cannot recover the steady conduction solution. Therefore, the magnetostatic solution becomes polluted too.

B. Unsymmetric EMQS A-V Formulation

Our main goal in this work is to develop a symmetric EMQS A-V formulation, and discuss its potential usefulness when applying it to eddy-current problems. A further constructive step in that direction is to recap an unsymmetric EMQS A-V formulation [4][8]. Remember that the system of the governing EMQS Maxwell's equations are (2)-(8). The potentials are defined as (12) and (13) again with an addition of having the scalar potential in the whole computational domain.

After substituting (12) and (13) into the EMQS Maxwell's equations (4), (7) and (8) in Ω_C, we obtain

$$\nabla \times \left(\nu \nabla \times \vec{A}\right) + j\omega\sigma \vec{A} + \sigma \nabla V + j\omega\varepsilon \nabla V = 0 \tag{30}$$

$$j\omega\rho + \nabla \cdot \left(-j\omega\sigma \vec{A} - \sigma \nabla V\right) = 0 \tag{31}$$

$$\rho - \nabla \cdot \left(-j\omega\varepsilon \vec{A} - \varepsilon \nabla V\right) = 0 \tag{32}$$

If we take the divergence of equation (30) and subtract it from (31), we obtain (3) for $\omega \neq 0$. If $\omega = 0$, (32) provides (3). This means that we implicitly satisfy (3) as it is required in an EMQS formulation.

Since we need only one auxiliary equation in addition to the Ampère's law (30), we could get rid of ρ from (31) and (32) by simply combining the two equations. However, it is more productive to eliminate ρ at the Galerkin discretization stage in the form of nodal charges. The reason of keeping ρ in the derivation is that its involvement provides the proper recipe for correctly implementing the continuity conditions on Γ_{CN}. We omit those details here and refer to [21] and [8] for details.

In Ω_N, we substitute (12) and (13) into the EMQS Maxwell's equations (4) and (8), and obtain

$$\nabla \times \left(\nu \nabla \times \vec{A}\right) + j\omega\varepsilon \nabla V = \vec{J}_S \tag{33}$$

$$-\nabla \cdot \left(-j\omega\varepsilon \vec{A} - \varepsilon \nabla V\right) = 0 \tag{34}$$

If we take the divergence of (33) we obtain (3) for $\omega \neq 0$, and (34) provides (3) for $\omega = 0$, thereby implicitly satisfying (3).

Then, we follow the Galerkin discretization procedure for systems (30)-(34), detailed in *Subsection III.A.1)* for eddy-current problems. As a result, the proper continuity conditions on Γ_{CN} for $\vec{E}$ and $\vec{B}$ are enforced in strong form by the FE basis function for $\vec{A}$ and *V*; while the continuity conditions for $\vec{H}$, $\vec{D}$ and $\vec{J}_C$ are retained in weak form. In summary, the linear system is

$$\begin{bmatrix} \mathbf{S}_\nu^{AA} + j\omega\mathbf{T}_\sigma^{AA} & \mathbf{M}_\sigma^{AC} + j\omega\mathbf{M}_\varepsilon^{AC} & j\omega\mathbf{M}_\varepsilon^{AN} \\ j\omega\left(\mathbf{M}_\sigma^{AC}\right)^T + (j\omega)^2\left(\mathbf{M}_\varepsilon^{AC}\right)^T & \mathbf{K}_\sigma^{CC} + j\omega\mathbf{K}_\varepsilon^{CC} & j\omega\mathbf{K}_\varepsilon^{CN} \\ j\omega\left(\mathbf{M}_\varepsilon^{AN}\right)^T & \left(\mathbf{K}_\varepsilon^{CN}\right)^T & \mathbf{K}_\varepsilon^{NN} \end{bmatrix} \begin{bmatrix} \mathbf{x}_A \\ \mathbf{x}_V^C \\ \mathbf{x}_V^N \end{bmatrix} = \begin{bmatrix} \mathbf{b}_S^A \\ \mathbf{b}_T^C \\ \mathbf{0} \end{bmatrix} \quad (35)$$

which can be considered as an extension of the eddy-current equations (20). It is obvious to compute the blocks of the system matrix and the RHS (right-hand side) in (35) based on the discussion in *Subsection III.A.1)*. The additional unknown block $\mathbf{x}_V^N$ is the column vector of the unknown V_m's in the approximation of the scalar potential in Ω_N

$$V_N^h = \sum_{m=1}^{N_N} V_m \beta_m \quad (36)$$

where N_N is the number of β_m's whose supports are nonzero in Ω_N but zero on Γ_{CN} and in Ω_C.

It is easy to prove that (35) is LF-stable by applying $\omega \to 0$. We can observe, similarly to (27), that the static regimes decouple correctly. The steady conduction problem in row 2 can be solved independently in Ω_C. Then, the steady-conduction current density acts as an additional source for the magnetostatic field in row 1, while the steady-conduction scalar potential serves as a Dirichlet BC for the electrostatic problem in row 3. However, the system matrix is unsymmetric so we are provoked to come up with a way to symmetrize the formulation, but keep the LF-stability.

IV. SYMMETRIC EMQS A-V FORMULATION

In order to arrive at a symmetric formulation, we pursue a similar strategy to the one that has been published for full-wave problems in [15]. We describe the strategy adjusted to EMQS problems in this section. Consider the standard definition of potentials (12) and (13) again. Let us apply an inexact Helmholtz decomposition to $\vec{A}$

$$\vec{A} = \vec{A}^{\#} + \nabla\psi \quad (37)$$

where $\nabla\psi$ is a gradient field and $\vec{A}^{\#}$ has nonzero curl and not necessarily zero divergence. In our FE environment (18), such decomposition can be generated by tree-cotree splitting of the lowest order vector basis functions. Then, (13) becomes

$$\vec{E} = -j\omega\left(\vec{A}^{\#} + \nabla\psi\right) - \nabla V \quad (38)$$

Since we have two scalar variables in (38), we need two additional auxiliary equations besides the Ampère's law. Thus, the governing equations we prefer in Ω_C are

$$\nabla\times\left(\nu\nabla\times\vec{A}^{\#}\right) + j\omega\sigma\vec{A}^{\#} + j\omega\sigma\nabla\psi + (\sigma + j\omega\varepsilon)\nabla V = 0 \quad (39)$$

$$j\omega\rho + \nabla\cdot\left(-j\omega\sigma\vec{A}^{\#} - j\omega\sigma\nabla\psi - \sigma\nabla V\right) = 0 \quad (40)$$

$$\rho - \nabla\cdot(-\varepsilon\nabla V) = 0 \quad (41)$$

$$\nabla\cdot\left((\sigma + j\omega\varepsilon)\vec{A}^{\#} + (\sigma + j\omega\varepsilon)\nabla\psi + \varepsilon\nabla V\right) = 0 \quad (42)$$

where (39) is the Ampère's law, (40) is the continuity equation (7), (41) is the Gauss's law (3) for the irrotational component $\vec{E}^g$, and (42) is a variant of the Coulomb gauge that is designed to make the system symmetric. The choice of (42) is similar but not identical to a corresponding choice in [15]. We have seemingly one extra auxiliary equation as in the unsymmetric case in *Subsection III.B*, but in this case too, it is more advantageous to eliminate ρ at the Galerkin discretization stage in the form of nodal charges.

In Ω_N, we choose (8) and (3) as auxiliary equations. Therefore, the set of governing equations are

$$\nabla\times\left(\nu\nabla\times\vec{A}^{\#}\right) + j\omega\varepsilon\nabla V = \vec{J}_S \quad (43)$$

$$-\nabla\cdot\left(-j\omega\varepsilon\vec{A}^{\#} - j\omega\varepsilon\nabla\psi - \varepsilon\nabla V\right) = 0 \quad (44)$$

$$-\nabla\cdot(-\varepsilon\nabla V) = 0 \quad (45)$$

We can employ the same Galerkin discretization process as in *Subsection III.B.*, and arrive at the following linear system:

$$\begin{bmatrix} \mathbf{S}_\nu^{AA} + j\omega\mathbf{T}_\sigma^{AA} & j\omega\mathbf{M}_\sigma^{AC} & \mathbf{M}_\sigma^{AC} + j\omega\mathbf{M}_\varepsilon^{AC} & j\omega\mathbf{M}_\varepsilon^{AN} \\ j\omega\left(\mathbf{M}_\sigma^{AC}\right)^T & j\omega\mathbf{K}_\sigma^{CC} & \mathbf{K}_\sigma^{CC} + j\omega\mathbf{K}_\varepsilon^{CC} & j\omega\mathbf{K}_\varepsilon^{CN} \\ \left(\mathbf{M}_\sigma^{AC}\right)^T + j\omega\left(\mathbf{M}_\varepsilon^{AC}\right)^T & \mathbf{K}_\sigma^{CC} + j\omega\mathbf{K}_\varepsilon^{CC} & \mathbf{K}_\varepsilon^{CC} & \mathbf{K}_\varepsilon^{CN} \\ j\omega\left(\mathbf{M}_\varepsilon^{AN}\right)^T & j\omega\left(\mathbf{K}_\varepsilon^{CN}\right)^T & \left(\mathbf{K}_\varepsilon^{CN}\right)^T & \mathbf{K}_\varepsilon^{NN} \end{bmatrix} \begin{bmatrix} \mathbf{x}_A \\ \mathbf{x}_\psi^C \\ \mathbf{x}_V^C \\ \mathbf{x}_V^N \end{bmatrix} = \begin{bmatrix} \mathbf{b}_S^A \\ \mathbf{b}_T^C \\ \mathbf{0} \\ \mathbf{0} \end{bmatrix} \quad (46)$$

where the blocks in the system matrix and the RHS can be computed as shown in *Subsection III.A.1)*. The additional unknown block $\mathbf{x}_\psi^C$ is the column vector of the unknown ψ_m in Ω_C with respect to the approximation

$$\psi \approx \psi_C^h = \sum_{m=1}^{N_C} \psi_m \beta_m \quad (47)$$

where N_C is the number of β_m's whose supports are nonzero in Ω_N and on Γ_{CN}, and zero elsewhere.

We can immediately observe that the system matrix in (46) is symmetric. As an extra advantage, the matrix is regular because $\nabla\times\vec{A}^{\#}$ has a trivial nullspace. Moreover, the system is LF-stable, which is evident if we write the system at $\omega \to 0$

$$\begin{bmatrix} \mathbf{S}_\nu^{AA} & \mathbf{0} & \mathbf{M}_\sigma^{AC} & \mathbf{0} \\ \mathbf{0} & \mathbf{0} & \mathbf{K}_\sigma^{CC} & \mathbf{0} \\ \left(\mathbf{M}_\sigma^{AC}\right)^T & \mathbf{K}_\sigma^{CC} & \mathbf{K}_\varepsilon^{CC} & \mathbf{K}_\varepsilon^{CN} \\ \mathbf{0} & \mathbf{0} & \left(\mathbf{K}_\varepsilon^{CN}\right)^T & \mathbf{K}_\varepsilon^{NN} \end{bmatrix} \begin{bmatrix} \mathbf{x}_A \\ \mathbf{x}_\psi^C \\ \mathbf{x}_V^C \\ \mathbf{x}_V^N \end{bmatrix} = \begin{bmatrix} \mathbf{b}_S^A \\ \mathbf{b}_T^C \\ \mathbf{0} \\ \mathbf{0} \end{bmatrix} \quad (48)$$

We can observe again – the same way as in the unsymmetric case – that the steady conduction field in Ω_C, the electrostatic field in Ω_N, and the magnetostatic field in the whole computational region are decoupled correctly and can be computed sequentially.

Note, that the extra scalar variable in Ω_C seemingly increases the number of unknowns significantly. However, that is not entirely the case because the extra variable is introduced by a tree-cotree decomposition of the lowest order vector basis functions. This means, that if we use only the lowest order basis functions, aka edge elements, the number of DoFs does not increase. There is only an increase in the number of unknowns if we switch to higher order elements.

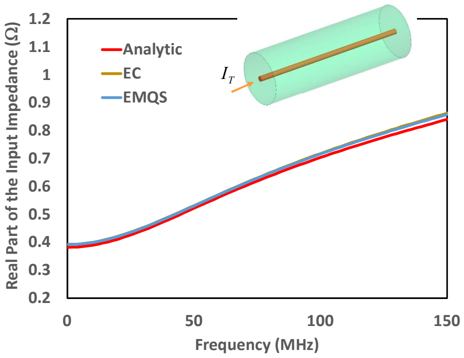

Fig. 2. Frequency sweep of the real part of the input impedance for the coaxial cable benchmark. The coaxial cable (see inset!) is short-circuited at the right end, and excited by a field pattern that an infinite long coaxial cable has at the left end. The outer shield is assumed to be PEC. The length of the cable is 100mm and the radius of the cylindrical conductor is 0.5mm. $\varepsilon_r = \mu_r = 1$ everywhere and $\sigma = 10^5\,\mathrm{S/m}$ in the conductor. The computation was performed by the new EMQS solver and the unsymmetric eddy-current (EC) solver discussed in *Subsection III.A.1)*. The calculated results are compared to an analytic solution.

V. VALIDATION

A. Coaxial Cable

The benchmark problem is depicted in the inset of Figure 2 and the setup is described in the figure caption. The figure plots the frequency sweep of the input conductance, which has a very accurate analytic approximation, the conductance of a cylindrical conductor in free space [22]. The error at any frequency point is under 1% so the agreement is excellent. When the frequency approaches zero, all three curves converge to the correct DC solution, which demonstrates the LF stability of the two formulations.

TABLE I lists some relative run-time data for the solution at 100MHz by the symmetric eddy-current solver discussed in *Subsection III.A.2)* and the symmetric EMQS solvers. The numbers of tetrahedrons are 19,019 and 12,060 in the conductor and the dielectric regions, respectively. The table shows that when we utilize the H0(curl) TVFEs, that is, the edge elements, the run time increases only by 21%. This increase is due to only the extension of the scalar potential V to the nonconducting region and not due to the extra scalar ψ in the conducting region. The extension of V to the nonconducting region provides access to the electrostatic field, which is a must if the capacitive effect is needed. When we utilize higher order TVFEs, the run time increases by a significantly larger rate, which is partially due to the extra scalar variable in the conductor.

TABLE I
RUN-TIME DATA FOR THE COAXIAL CABLE AT 100MHZ

TVFEs	**RELATIVE RUN TIME**		**RUN TIME**
	EC	**EMQS**	**EMQS/EC (%)**
H0(curl)	1.00	1.21	121
H1(curl)	2.82	4.05	144
H2(curl)	10.45	16.94	162

B. Serial RLC Benchmark

The other benchmark problem we make use of is a serial RLC arrangement with strong resistive, capacitive and inductive effects depicted in Figure 3 [15][4]. This “eddy-current problem” cannot be solved by an eddy-current solver because the capacitive effect is an essential factor in the current flow. Therefore, we compare computed input impedances generated by the symmetric EMQS solver and a full-wave solver in Figure 4.a). Both solvers can recover the resonances, and the agreement between the two calculations is excellent. This is understandable because the length of the structure is smaller than the vacuum wavelength of the highest frequency so the EMQS solver is as accurate as the full-wave solver.

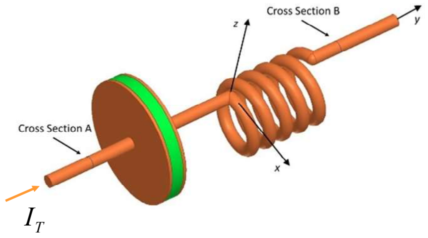

Fig. 3. Serial RLC arrangement where the conducting wire and capacitor are in vacuum. The geometrical dimensions can be found in [15] and [8]. The material properties of the wire are $\varepsilon_r = \mu_r = 1$ and $\sigma = 10^5\,\mathrm{S/m}$, and the capacitor is lossless with $\varepsilon_r = 2$ and $\mu_r = 1$. The RLC unit is short-circuited at the right end of the wire, and the excitation is the same as in the case of the coaxial cable in Figure 2.

Figure 4.b) demonstrates the LF stability of the symmetric EMQS solver by plotting the input conductance which correctly converges to zero as the frequency is decreasing. To illustrate the spatial accuracy of the EMQS solver, we plot various field quantities at 100MHz in Figure 5. The results picture well how the electric and magnetic field energies correctly alternate.

VI. CONCLUSIONS

We have developed a time-harmonic EMQS A-V formulation with complex symmetric and LF-stable system matrix. Advantageously, we can employ either a direct or an iterative equation solver because the system matrix is regular. We have verified the formulation by comparing results to computations by eddy-current and full-wave solvers. Through the solution of the benchmark problems, we have also illustrated the merits of the new formulation, and demonstrated and interpreted the nature of the potential increase of the run-time costs.

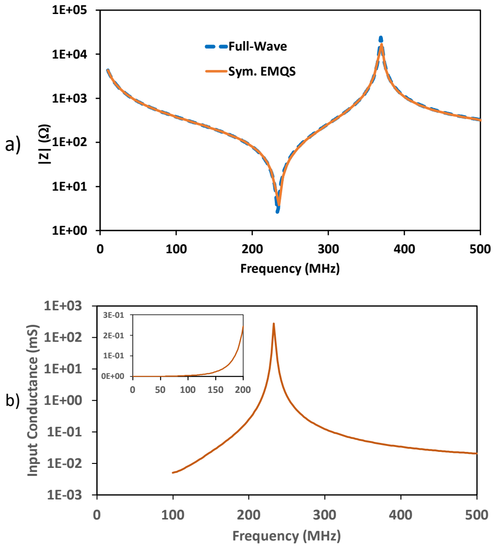

Fig. 4. Frequency sweeps: a) modulus of the input impedance compared to a full-wave solver; b) input conductance computed by the symmetric EMQS solver demonstrating the LF stability in the inset

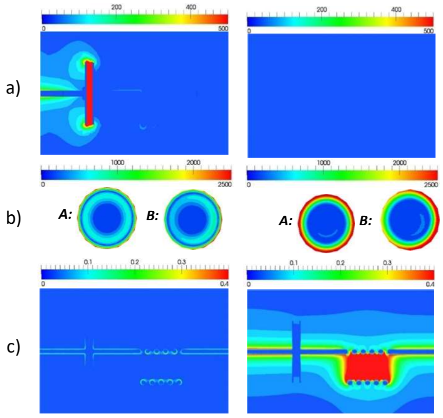

100 MHz, real

100 MHz, imag.

Fig. 5. Field plots at 100MHz by the symmetric EMQS solver: a) electric field in V/m; b) eddy current density in A/m^2 on the conductor cross sections **A** and **B** in Figure 3; c) magnetic field intensity in A/m.

We have pointed out that the symmetric EMQS solver is a great tool to solve eddy-current problems where we need to consider the capacitive effects, or the LF stability is important. Such cases involve situations where a frequency sweep is required and/or resonances needed to be identified. Another class of eddy-current problems that can be treated efficiently with the EMQS solver is where lossy dielectrics are included in the problem and their presence affects the computational results considerably.

VII. ACKNOWLEDGEMENT

This work was supported by the Hungarian Scientific Research Fund under grant K-135307.

REFERENCES

[1] O. Bíró, "Edge element formulations of eddy current problems," *Comput. Methods Appl. Mech. Engrg.* **169**, pp. 391-405, 1999.

[2] S. Koch, H. Schneider, T. Weiland, "A Low-Frequency Approximation to the Maxwell Equations Simultaneously Considering Inductive and Capacitive Phenomena," *IEEE Trans. Magn.*, vol. 48, no. 2, pp. 511-514, 2012.

[3] S. L. Ho, Y. Zhao, W. N. Fu, P. Zhou, "Application of edge elements to 3-D electromagnetic field analysis accounting for both inductive and capacitive effects," *IEEE Trans. Magn.*, vol. 52, no. 3, DOI: 10.1109/ TMAG.2015.2483620, 2016.

[4] Z. Badics, S. Bilicz, J. Pávó, S. Gyimóthy, "Finite-element A-V formulation for quasistatic Darwin models," in *Proc. 18th Biennial IEEE CEFC Conference*, Hangzhou, China, Oct. 2018.

[5] I. C. Garcia, S. Schöps, H. De Gersem, and S. Baumanns, "Chapter 1: Systems of differential algebraic equations in computational electromagnetics," in Applications of DAEs: Examples and Benchmarks, (S. Cambell, A. Ilchmann, V. Mehrmann, and T. Reis, eds.) pp. 123-169, Springer Verlag, 2018.

[6] M. Clemens, B. Khäne, and S. Schöps, "A Darwin time domain scheme for the simulation of transient quasistatic EM fields including resistive, capacitive and inductive effects," in *2019 Kleinheubach Conference*, *Miltenberg, Germany*, pp. 1-4, 2019.

[7] Y. Zhao, Z. Tang, "A novel gauged potential formulation for 3d electromagnetic field analysis including both inductive and capacitive effects," *IEEE Trans. Magn*, vol. 55, no. 6, DOI: 10.1109/ TMAG.2019.2899288, 2019.

[8] Z. Badics, J. Pávó, S. Bilicz S. Gyimóthy, "Subdomain perturbation finite-element method for quasi-static Darwin approximation," *IEEE Trans. Magn.*, vol. 56, no. 1, DOI:10.1109/ TMAG.2019.2951066, 2020.

[9] H. Kaimori, T. Mufune, A. Kameari, "Novel application of Coulomb gauge condition in electromagnetic fem computation for Darwin approximation," *in Proc. IEEE CEFC 2020 Conference*, Pisa, Italy, p. 497, 2020.

[10] M. Clemens, F. Kasolis, M.-L. Henkel, B. Kähne, M. Günther, "A two-step Darwin model time domain formulation for quasistatic electromagnetic field calculations," *IEEE Trans. Magn.*, vol. 57, no. 6, DOI: 10.1109/ TMAG.2021.3057828, 2021.

[11] A. Bingler, S. Bilicz, M. Csörnyei, Z. Badics, "Thin-wire Integral Equation Formulation with Quasistatic Darwin Approximation," *IEEE Trans. Magn.*, vol. 57, no. 6, DOI: 10.1109/ TMAG.2021.3064912, 2021.

[12] H. Taha, Z. Tang, T. Henneron, Y. Le Menach, F. Salomez, J.-P. Ducreux, "Numerical Simulation-Based Investigation of the Limits of Different Quasistatic Models," *Applied Sciences*, vol. 11, https://doi.org/10.3390/app112311218, 2021.

[13] J. Ostrowski, and C. Winkelmann, "Limitations of the Two-Step Darwin Model in Frequency Domain," *IEEE Trans. Magn.*, vol. 58, no. 9, https://doi.org/10.1109/TMAG.2022.3163611, 2022.

[14] M. Clemens, *et al*, "Electromagnetic Quasistatic Field Formulations of Darwin Type," *International Compumag Society Newsletter*, vol. 29, no. 1, ISSN 1026-0854, 1 March 2022.

[15] M. Jochum, O. Farle, R. Dyczij-Edlinger, "A new low-frequency stable potential formulation for the finite-element simulation of electromagnetic fields," *IEEE Trans. Magn.*, vol. 51, no. 3, DOI: 10.1109/TMAG.2014.2360080,2015.

[16] J. Larson, "Electromagnetics from quasistatic perspective," *Am. J. Phys.*, vol. 75, no. 3, pp. 230-239, 1995.

[17] S.E. Kruger, "The Three Quasistatic Limits of the Maxwell Equations," arXiv:1909.11264v1 [physics.class-ph] 25 Sep. 2019.

[18] Z. Badics, "Transient Eddy Current Field of Current Forced Three-Dimensional Conductors," *IEEE Trans. Magn.*, vol. 28, no. 2, pp. 1232-1234, 1992.

[19] R. Hiptmair, and O. Sterz, "Current and Voltage Excitations for the Eddy Current Model," *Int. J. of Numerical Modeling, Electronic Networks, Devices and Fields*, vol. 18, issue 1, pp. 1-21, 2005.

[20] R.D. Graglia, A.F. Peterson, and F.P. Andruilli, "Curl-Conforming Hierarchical Vector Bases for Triangles and Tetrahedra," *IEEE Trans. on Antennas and Propagation*, vol. 59,

[21] Z. Badics, J. Pávó, "Full wave potential formulation with low-frequency stability," *IEEE Trans. Magn.,* vol. 51, no. 3, DOI: 10.1109/TMAG.2014.2362114, 2015.

[22] J.A. Stratton, *Electromagnetic Theory*, Hoboken, NJ:IEEE Press, John Wiley & Sons, 2007

GPU-Accelerated Body-Internal Electric Field Exposure Simulation Using Low-Frequency Magnetic Field Sampling Points

Haussmann Norman (1),Stroka Steven (1),Schmuelling Benedikt (2),Clemens Markus (1)

(1)Chair of Electromagnetic Theory, University of Wuppertal, Wuppertal, Germany;
(2)Institute of Electric Mobility and Energy Storage Systems, University of Wuppertal, Wuppertal, Germany

Purpose:

High resolution simulations of body-internal electric field strengths induced by magneto-quasistatic fields from wireless power transfer systems are computationally expensive. The exposure simulation can be split into two separate simulation steps allowing the calculation of the magnetic flux density distribution, which serves as input into the second simulation step to calculate the body-internal electric fields. In this work, the magnetic flux density is interpolated from in situ measurements in combination with the scalar-potential finite difference scheme to calculate the resulting body-internal field. These calculations are supposed to take less than 5 s to achieve a near real-time visualization of these fields on mobile devices. The purpose of this work is to present an implementation of the simulation on graphics processing units (GPUs), allowing for the calculation of the body-internal field strength in about 3s.

Design/methodology/approach:

This work uses the co-simulation scalar-potential finite difference scheme to determine the body-internal electric field strength of human models with a voxel resolution of 2×2 × 2mm3. The scheme is implemented on GPUs. This simulation scheme requires the magnetic flux density distribution as input, determined from radial basis functions.

Findings:

Using NVIDIA A100 GPUs, the body-internal electric field strength with high-resolution models and 8.9 million degrees of freedom can be determined in about 2.3s.

Originality/value:

This paper describes in detail the used scheme and its implementation to make use of the computational performance of modern GPUs.

Keywords:

Augmentedreality, Graphics processing unit, Real-time, Scalar-potential finite difference, Wireless power transfer

Published in COMPEL - The international journal for computation and mathematics in electrical and electronic engineering, Vol. 42 No. 5, 2023, ISSN 0332-1649, page 982 - 992

Micromagnetics and multiscale hysteresis simulations of permanent magnets

Yang Yangyiwei,Kühn Patrick,Fathidoost Mozhdeh,Xu Bai-Xiang
Mechanics of Functional Materials Division, Technische Universität Darmstadt, Darmstadt, Germany

Purpose:

Confronting the unveiled sophisticated structural and physical characteristics of permanent magnets, notably the samarium–cobalt (Sm-Co) alloy, This work aims to introduce a simulation scheme that can link physics-based micromagnetics on the nanostructures and magnetostatic homogenization on the mesoscale polycrystalline structures.

Design/methodology/approach:

The simulation scheme is arranged in a multiscale fashion. The magnetization behaviors on the nanostructures examined with various orientations are surrogated as the micromagnetic-informed hysterons. The hysteresis behavior of the mesoscale polycrystalline structures with micromagnetic-informed hysterons is then evaluated by computational magnetostatic homogenization.

Findings:

The micromagnetic-informed hysterons can emulate the magnetization reversal of the parameterized Sm-Co nanostructures as the local hysteresis behavior on the mesostructures. The simulation results of the mesoscale polycrystal demonstrate that the demagnetization process starts from the grain with the largest orientation angle (a) and then propagates to the surrounding grains.

Originality/value:

This work provides a novel multiscale scheme for simulating the polycrystalline permanent magnets' hysteresis while recapitulating the nanoscale mechanisms, such as the nucleation of domains, and domain wall migration and pinning. This scheme can be further extended to simulate the part-level hysteresis considering the mesoscale features.

Keywords:

Micromagnetics, Magnetostatic homogenization, Permanent magnets, Polycrystal

Published in COMPEL - The international journal for computation and mathematics in electrical and electronic engineering, Vol. 42 No. 5, 2023, ISSN 0332-1649, page 993 - 1006

Pyrit: A finite element based field simulation software written in Python

Bundschuh Jonas,Ruppert M. Greta,Späck-Leigsnering Yvonne
Institut für Teilchenbeschleunigung und Elektromagnetische Felder (TEMF), TU Darmstadt, Germany;

Purpose:

The purpose of this paper is to present the freely available finite element simulation software Pyrit.

Design/methodology/approach:

In a first step, the design principles and the objective of the software project are defined. Then, the software's structure is established: The software is organized in packages for which an overview is given. The structure is based on the typical steps of a simulation workflow, i.e., problem definition, problem-solving and post-processing. State-of-the-art software engineering principles are applied to ensure a high code quality at all times. Finally, the modeling and simulation workflow of Pyrit is demonstrated by three examples.

Findings:

Pyrit is a field simulation software based on the finite element method written in Python to solve coupled systems of partial differential equations. It is designed as a modular software that is easily modifiable and extendable. The framework can, therefore, be adapted to various activities, i.e., research, education and industry collaboration.

Originality/value:

In research, problem-specific modifications and direct access to the source code of simulation tools are essential. With Pyrit, the authors present a computationally efficient and platform-independent simulation software for various electromagnetic and thermal field problems.

Keywords:

Finite element method, Computational electromagnetics, Coupled systems, Field-circuit coupling, Circuit models

Published in COMPEL - The international journal for computation and mathematics in electrical and electronic engineering, Vol. 42 No. 5, 2023, ISSN 0332-1649, page 1007 - 1020

The system for distributed energy resources testing according to the IEEE 1547-2018 standard

Dimitrijević Marko A.,Petronijević Milutin
Department of Electronics, Faculty of Electronic Engineering, University of Niš, Niš, Serbia

Purpose:

This paper aims to propose a new approach to testing distributed energy resources (DERs) in compliance with the IEEE 1547-2018 standard and describes a new, integrated testing and validation system.

Design/methodology/approach:

The system is built on the virtual instrumentation paradigm, using acquisition modules to measure physical quantities, while signal processing, including intensive calculations of required parameters, data processing, manipulation and reporting are performed on a computing device.

Findings:

Intensive laboratory measurements were performed on a laboratory prototype of a microgrid that emulates DERs. The results obtained using the system described were compared with the measurements obtained by the reference instruments. As all the results match, the usability of the system was verified.

Originality/value:

This paper emphasizes the advantages of the proposed approach over classical testing. The value of the paper is reflected in the applicability and practical implications of the proposed and described hardware and software technical solutions.

Keywords:

Distributed energy resources, Power quality, Virtual instrumentation

Published in COMPEL - The international journal for computation and mathematics in electrical and electronic engineering, Vol. 42 No. 5, 2023, ISSN 0332-1649, page 1021 - 1038

Eddy current losses in power voltage transformer open-type cores

Frljić Stjepan,Trkulja Bojan,Drandić Ana
Faculty of Electrical Engineering and Computing, University of Zagreb, Zagreb, Croatia

Purpose:

The purpose of this paper is to present a methodology for calculating eddy current losses in the core of a single-phase power voltage transformer, which, unlike a standard power transformer, has an open-type core (I-type core). In those apparatus, reduction of core losses is achieved by using a multipart open-type core that is created by merging a larger number of leaner cores.

Design/methodology/approach:

3D FEM approach for calculation of eddy current losses in open-type cores based on a weak AA formulation is presented. Method in which redundant degrees of freedom are eliminated is shown. This enables faster convergence of the simulation. The results are benchmarked using simulations with standard AVA formulation.

Findings:

Results using weak AA formulation with elimination of redundant degrees of freedom are in agreement with both simulation using only weak AA formulation and with simulation based on AVA formulation.

Originality/value:

The presented method is specifically adapted for calculating eddy currents in the open-type core. The method is based on a weak formulation for the magnetic vector potential A and the current vector potential , incorporating numerical homogenization and a straightforward elimination of redundant degrees of freedom, resulting in faster convergence of the simulation.

Keywords:

Eddycurrents, FEM, Transformers, Finite element method

Published in COMPEL - The international journal for computation and mathematics in electrical and electronic engineering, Vol. 42 No. 5, 2023, ISSN 0332-1649, page 1039 - 1051

Electric field and SAR distribution in the vicinity of dental implants exposed to the cell phone electromagnetic radiation

Jovanovic Dejan (1),Krasic Dragan (2),Cvetkovic Nenad N. (1),Vuckovic Dragan (3),Stankovic Vladimir (4)

(1) Department of Theoretical Electrical Engineering, Faculty of Electronic Engineering, University of Nis, Nis, Serbia;
(2) Faculty of Medicine, University of Nis, Nis, Serbia;
(3) Department of Power Engineering, Faculty of Electronic Engineering, University of Nis, Nis, Serbia
(4) Faculty of Occupational Safety, University of Nis, Nis, Serbia

Purpose:

The purpose of this paper is to determine the electric field and specific absorption rate (SAR) distribution within biological tissues in the vicinity of dental implants, exposed to the mobile phone radiation.

Design/methodology/approach:

This research was performed for the frequency of 2.6GHz, which corresponds to 4G mobile network. The adequate 3D realistic numerical models of the mobile phone user's head, dental implants and actual smartphone model are created using packages based on the finite integral technique numerical method.

Findings:

The obtained results yield to a conclusion that the presence of dental implants affects the increase in electric field intensity and SAR values within biological tissues in its vicinity.

Originality/value:

The accurate determination of the electric field and SAR values within different biological tissues and organs in the vicinity of dental implants exposed to mobile phone electromagnetic radiation, demands highly realistic model of observed biological structures. For purposes of the current study, the procedure for modeling of highly nonhomogeneous structure with finite number of homogenous domains having known electromagnetic parameters is described in the paper. As a result, the 3D complex users' head model formed of 16 homogeneous domains of different electromagnetic parameters is created.

Keywords:

Dentalamalgam, Electromagnetic radiation, Mobile communication, Specific absorption rate

Published in COMPEL - The international journal for computation and mathematics in electrical and electronic engineering, Vol. 42 No. 5, 2023, ISSN 0332-1649, page 1052 - 1067

On the field uniformity of reverberation chambers – a global sensitivity analysis study

Kenderes Anett (1,2),Gyimóthy Szabolcs (1),Benkő Péter Tamás (2)

(1) Budapest University of Technology and Economics, Budapest, Hungary;
(2) Department of Automotive Electronics– Electromagnetic Compatibility (AE/EMC-HU), Robert Bosch Kft, Budapest, Hungary

Purpose:

Global sensitivity analysis (SA) by means of Sobol' indices enhanced with different surrogate modeling techniques is performed in this work. The purpose is to investigate the influence of measurement uncertainties and the environment characteristics themselves on the desired field uniformity in reverberation chambers (RCs). This yields an efficient apparatus for the stirring and chamber design process.

Design/methodology/approach:

The technique of Sobol' indices, as a candidate of global SA methods, is suitable for high fluctuations due to its robustness, which can be addressed to the stochastic nature of the RC environment. The aim of using surrogate modeling techniques is to compute the indices efficiently with a moderate number of required simulations. The powerfulness of this approach is introduced in a simple numerical example in which the physical phenomena can be identified more straightforwardly.

Findings:

This method can provide useful knowledge in the lower frequency range, where the ideal properties of the electromagnetic field in RCs cannot be established, and the importance of the setup parameters can vary from configuration to configuration. In addition, it can serve as a basis for setup adaptation during parallelized electromagnetic compatibility tests, which would result in a more time- and cost-saving option in industrial applications in the future.

Originality/value:

Despite the previous attempts, a profound investigation of multiple setup parameters is still a hot topic. The main contribution of this work is the extension of the application area of the method of Sobol' indices to RCs, which has not been done so far.

Keywords:

Sensitivity analysis, Electromagnetic compatibility, Computational electromagnetics, Surrogate optimization, Reverberation chambers, Surrogate modeling, Electromagnetic simulation

Published in COMPEL - The international journal for computation and mathematics in electrical and electronic engineering, Vol. 42 No. 5, 2023, ISSN 0332-1649, page 1068 - 1080

Comparison of damping techniques in non-linear spring-mass systems for power transformers under short-circuit condition

Koczka Gergely,Leber Gerald
GT PRM BRE MM,SiemensEnergyAG, Weiz,Austria

Purpose:

The simplified modeling of many physical processes results in a second-order ordinary differential equation (ODE) system. Often the damping of these resonating systems cannot be defined in the same simplified way as the other parameters due to the complexity of the physical effects. The purpose of this paper is to develop a mathematically stable approach for damping resonances in nonlinear ODE systems.

Design/methodology/approach:

Modifying the original ODE using the eigenvalues and eigenvectors of a linearized state leads to satisfying results.

Findings:

An iterative approach is presented, how to modify the original ODE, to achieve a well-damped solution.

Originality/value:

The iterative algorithm to modify the original ODE is novel. It can be used on different fields of the physics, where a second-order ODE is describing the problem, which has only measured or empirical damping.

Keywords:

Transformers, Force calculation

Published in COMPEL - The international journal for computation and mathematics in electrical and electronic engineering, Vol. 42 No. 5, 2023, ISSN 0332-1649, page 1081 - 1091

Modelling stranded wires using homogenization and the Cauer ladder method

Koester Niels (1,2),Pichler Franz (1),Biro Oszkar (2)

(1)Department E: Electrics/Electronics and Software, Virtual Vehicle Research Center, Graz, Austria;
(2) Institute of Fundamentals and Theory in Electrical Engineering, Austria

Purpose:

The purpose of this paper is to introduce a new method to model a stranded wire efficiently in 3D finite element simulations.

Design/methodology/approach:

In this method, the stranded wires are numerically approximated with the Cauer ladder network (CLN) model order reduction method in 2D. This approximates the eddy current effect such as the skin and proximity effect for the whole wire. This is then projected to a mesh which does not include each strand. The 3D fields are efficiently calculated with the CLN method and are projected in the 3D geometry to be used in simulations of electrical components with a current vector potential and a homogenized conductivity at each time step.

Findings:

In applications where the stranded wire geometry is known and does not change, this homogenization approach is an efficient and accurate method, which can be used with any stranded wire configuration, homogenized stranded wire mesh and any input signal dependent on time steps or frequencies.

Originality/value:

In comparison to other methods, this method has no direct frequency dependency, which makes the method usable in the time domain for an arbitrary input signal. The CLN can also be used to interconnected stranded cables arbitrarily in electrical components.

Keywords:

Eddycurrent problems, Finite element method, Homogenization, Model order reduction, Eddy current

Published in COMPEL - The international journal for computation and mathematics in electrical and electronic engineering, Vol. 42 No. 5, 2023, ISSN 0332-1649, page 1092 - 1102

Fast numerical techniques for FE simulations in electrical capacitance tomography

Neumayer Markus (1),Suppan Thomas (1),Bretterklieber Thomas (1),Wegleiter Hannes (1),Fox Colin (2)

(1)Christian Doppler Laboratory for Measurement Systems for Harsh Operating Conditions, Institute of Electrical Measurement and Sensor Systems, Graz University of Technology, Graz, Austria;
(2) Department of Physics, University of Otago, Dunedin, New Zealand

Purpose:

Nonlinear solution approaches for inverse problems require fast simulation techniques for the underlying sensing problem. In this work, the authors investigate finite element (FE) based sensor simulations for the inverse problem of electrical capacitance tomography. Two known computational bottlenecks are the assembly of the FE equation system as well as the computation of the Jacobian. Here, existing computation techniques like adjoint field approaches require additional simulations. This paper aims to present fast numerical techniques for the sensor simulation and computations with the Jacobian matrix.

Design/methodology/approach:

For the FE equation system, a solution strategy based on Green's functions is derived. Its relation to the solution of a standard FE formulation is discussed. A fast stiffness matrix assembly based on an eigenvector decomposition is shown. Based on the properties of the Green's functions, Jacobian operations are derived, which allow the computation of matrix vector products with the Jacobian for free, i.e. no additional solves are required. This is demonstrated by a Broyden–Fletcher–Goldfarb–Shanno-based image reconstruction algorithm.

Findings:

MATLAB-based time measurements of the new methods show a significant acceleration for all calculation steps compared to reference implementations with standard methods. E.g. for the Jacobian operations, improvement factors of well over 100 could be found.

Originality/value:

The paper shows new methods for solving known computational tasks for solving inverse problems. A particular advantage is the coherent derivation and elaboration of the results. The approaches can also be applicable to other inverse problems.

Keywords:

ECT,FEsimulation, Green's function, Jacobian operations

Published in COMPEL - The international journal for computation and mathematics in electrical and electronic engineering, Vol. 42 No. 5, 2023, ISSN 0332-1649, page 1103 - 1114

Evaluating magnetic fields using deep learning

Rahman Mohammad, Mushfiqur Khan Arbaaz,Lowther David,Giannacopoulos Dennis
Computational Electromagnetics Lab, McGill University, Montreal, Canada

Purpose:

The purpose of this paper is to develop surrogate models, using deep learning (DL), that can facilitate the application of EM analysis software. In the current status quo, electrical systems can be found in an ever-increasing range of products that are part of everyone's daily live. With the advances in technology, industries such as the automotive, communications and medical devices have been disrupted with new electrical and electronic systems. The innovation and development of such systems with increasing complexity over time has been supported by the increased use of electromagnetic (EM) analysis software. Such software enables engineers to virtually design, analyze and optimize EM systems without the need for building physical prototypes, thus helping to shorten the development cycles and consequently cut costs.

Design/methodology/approach:

The industry standard for simulating EM problems is using either the finite difference method or the finite element method (FEM). Optimization of the design process using such methods requires significant computational resources and time. With the emergence of artificial intelligence, along with specialized tools for automatic differentiation, the use of DL has become computationally much more efficient and cheaper. These advances in machine learning have ushered in a new era in EM simulations where engineers can compute results much faster while maintaining a certain level of accuracy.

Findings:

This paper proposed two different models that can compute the magnetic field distribution in EM systems. The first model is based on a recurrent neural network, which is trained through a data-driven supervised learning method. The second model is an extension to the first with the incorporation of additional physics-based information to the authors' model. Such a DL model, which is constrained by the laws of physics, is known as a physics-informed neural network. The solutions when compared with the ground truth, computed using FEM, show promising accuracy for the authors' DL models while reducing the computation time and resources required, as compared to previous implementations in the literature.

Originality/value:

The paper proposes a neural network architecture and is trained with two different learning methodologies, namely, supervised and physics-based. The working of the network along with the different learning methodologies is validated over several EM problems with varying levels of complexity. Furthermore, a comparative study is performed regarding performance accuracy and computational cost to establish the efficacy of different architectures and learning methodologies.

Keywords:

Finite element analysis (FEA), Field analysis, Partial differential equations (PDEs), Magnetic device, Recurrent neural network (RNN), Physics-informed neural network (PINN), Gated recurrent unit (GRU), Physics-informed recurrent neural network (PI-RNN), Deep learning (DL), Finite elements (FE), Finite element method (FEM), Electromagnetics (EM), Magnetic flux density

Published in COMPEL - The international journal for computation and mathematics in electrical and electronic engineering, Vol. 42 No. 5, 2023, ISSN 0332-1649, page 1115 - 1132

Topology optimization and parameter optimization hybridized by mesh smoothing for IPMSM design

Sun Zhen,Sato Takahiro,Watanabe Kota

Graduate School of Engineering, Muroran Institute of Technology, Muroran, Japan

Purpose:

Topology optimization (TO) methods have shown their unique advantage in the innovative design of electric machines. However, when introducing the TO method to the rotor design of interior permanent magnet (PM) synchronous machines (IPMSMs), the layout parameters of the magnet cannot be synchronously optimized with the topology of the air barrier; the full design potential, thus, cannot be unlocked. The purpose of this paper is to develop a novel method in which the layout parameters PMs and the topology of air barriers can be optimized simultaneously for aiding the innovative design of IPMSMs.

Design/methodology/approach:

This paper presents a simultaneous TO and parameter optimization (PO) method that is applicable to the innovative design of IPMSMs. In this method, the mesh deformation technique is introduced to make it possible to make a connection between the TO and PO, and the multimodal optimization problem can thereby be solved more efficiently because good topological features are inherited during iterative optimization.

Findings:

The numerical results of two case studies show that the proposed method can find better Pareto fronts than the traditional TO method within comparable time-consuming. As the optimal design result, novel rotor structures with better torque profiles and higher reluctance torque are respectively found.

Originality/value:

A method that can simultaneously optimize the topology and parameter variables for the design of IPMSMs is proposed. The numerical results show that the proposed method is useful and practical for the conceptual and innovative design of IPMSMs because it can automatically explore optimal rotor structures from the full design space without relying on the experience and knowledge of the engineer.

Keywords:

Finite element analysis, Optimal design, Permanent magnet machine, Topology optimization

Published in COMPEL - The international journal for computation and mathematics in electrical and electronic engineering, Vol. 42 No. 5, 2023, ISSN 0332-1649, page 1133 - 1147

An improved on/off method with a two-step surface smoother for topology optimization of electromagnetic devices

Sun Zhen (1),Watanabe Kota (2)

(1) Division of Engineering, Muroran Institute of Technology, Muroran, Japan;
(2) Department of Information and Electronic Engineering, Muroran Institute of Technology, Muroran, Japan

Purpose:

Topology optimization is a state-of-the-art technique for the innovative design of electromagnetic devices. The ON/OFF method is a typical approach for this purpose. However, the drawbacks of long iteration time and poor ability to express curved surfaces make the industry not shown their due interest so far in the ON/OFF method. The purpose of this paper is to study a novel ON/OFF method for topology optimization, which can bring feasible optimized shapes that are more friendly for industrial realization in a shorter time.

Design/methodology/approach:

The proposed improved ON/OFF method uses structured triangular elements for finite element modeling because the triangular elements can more freely express shape features. Every four triangular elements are pieced together to form a square cell, each quadrilateral cell is associated with a binary value indicating the material state of the four triangular elements. The binary metaheuristic algorithms are used to optimize the material distribution. After the material filling for the elements based on the output of the metaheuristic algorithm, a two-step surface smoother will be performed as the postprocess to make the shapes more friendly for manufacturing.

Findings:

The comparative numerical results on a benchmark topology optimization problem show that the proposed method can bring feasible optimized shapes that are more friendly for industrial realization in a shorter time. In addition, the speed and robustness of convergence, especially in the case of multiobjective topology optimization problem, are significantly improved.

Originality/value:

A novel ON/OFF method for topology optimization is proposed. Compared with the traditional ON/OFF method, the proposed method is better in terms of searching efficiency and robustness. Moreover, the proposed method can provide feasible optimized shapes that are more friendly for industrial realization.

Keywords:

Evolution strategies, Finite element method, ON/OFF method, Topology optimization

Published in COMPEL - The international journal for computation and mathematics in electrical and electronic engineering, Vol. 42 No. 5, 2023, ISSN 0332-1649, page 1148 - 1162

Toward a simple topological model of a three-phase transformer including deep saturation conditions

Zirka Sergey E. (1),Albert Dennis (2),Moroz Yuri I. (2),Domenig Lukas (3),Schürhuber Robert (2)

(1) Department of Physics and Technology, Dnipro National University, Dnipro, Ukraine;
(2)Institute of Electrical Power Systems, Graz University of Technology, Graz, Austria;
(3) Institute of Fundamentals and Theory of Electrical Engineering, Graz University of Technology, Graz, Austria

Purpose:

This paper aims to propose a method of parametrizing topological transformer model at high flux densities in the core.

Design/methodology/approach:

The approach proposed is based on terminal voltages and currents measured in a special purpose saturation test whose data are combined with typical saturation curves of grain-oriented electrical steels; the modeling is carried out in the ATPDraw program.

Findings:

The authors corroborate experimentally the necessity of dividing the zero sequence impedance between all transformer phases and propose a method of the individual representation of the legs and yokes. This eliminates the use of nonexistent leakage inductances of primary and secondary windings.

Originality/value:

The proposed approach is completely original and will contribute to a better understanding of the transients occurring in a transformer under abnormal conditions, such as inrush current events and GICs.

Keywords:

Transformermodel, Core saturation, Zero sequence representation

Published in COMPEL - The international journal for computation and mathematics in electrical and electronic engineering, Vol. 42 No. 5, 2023, ISSN 0332-1649, page 1163 - 1174

Asymmetric air gap fault detection in linear permanent magnet Vernier machines

Arianborna Mohammadhossein,Faiz Jawad,Ghods Meharage,Erfani-Nik Amirhossein

School of Electrical and Computer Engineering, College of Engineering, University of Tehran, Tehran, Iran

Purpose:

The aim of this paper is to introduce an accurate asymmetric fault index for the diagnosis of the faulty linear permanent magnet Vernier machine (LPMVM).

Design/methodology/approach:

Three-dimensional finite element method is applied to model the LPMVM. The geometrical and physical properties of the machine, the effect of stator and translator teeth, magnetic saturation of core and nonuniform air gap due to asymmetric fault are taken into account in the simulation. The air gap asymmetric fault is proposed. This analytical method estimates the air gap flux density of an LPMVM.

Findings:

This paper presents an analytical method to predict the performance of a healthy and faulty LPMVM. The introduced index is based on the frequency patterns of the stator current. Besides, the robustness of the index in different loads and fault severity is addressed.

Originality/value:

Introducing index for air gap asymmetry fault diagnosis of LPMVM.

Keywords:

LinearVernier machine, Dynamic asymmetric air gap fault (DAAGF), Linear permanent magnet Vernier generator (LPMVG)

Published in COMPEL - The international journal for computation and mathematics in electrical and electronic engineering, Vol. 42 No. 5, 2023, ISSN 0332-1649, page 1175 - 1186

Thermal analysis for foreign objects in high-power wireless power transfer systems

Tiemann Myrel (1),Clemens Markus (2),Schmuelling Benedikt (1)

(1) Department of Electric Mobility and Energy Storage Systems, School of Electrical, Information and Media Engineering, University of Wuppertal, Wuppertal, Germany;
(2)Chair of Electromagnetic Theory, School of Electrical, Information and Media Engineering, University of Wuppertal, Wuppertal, Germany

Purpose:

This paper aims to present a fast and modular framework implementation for the thermal analyses of foreign metal objects in the context of wireless power transfer (WPT) to evaluate whether they pose a hazard to the system. This framework serves as a decision-making tool for determining the necessity of foreign object detection in certain applications and at certain transmitted power levels.

Design/methodology/approach:

To assess the necessity of implementing foreign object detection, the considered WPT system is modeled, and Arnoldi-Krylov-based model order reduction is applied to generate separate reduced models of the ground and vehicle modules of the WPT system. This enables interoperable evaluations to be conducted. Further discussion on the implementation details of the system-level simulations used to evaluate the electrical and thermal characteristics is provided. The resulting modular implementation allows for efficient evaluation of the thermal behavior of the wireless charging system at various transferred power levels and under various boundary conditions.

Findings:

Based on the transferred power level, the WPT model, the relative positioning between the vehicle and the charging pad and the charging time, it may be necessary to divide the area of the charging pad into multiple regions for the purpose of implementing foreign object detection.

Originality/value:

While the tools and fundamentals of thermal analysis are widely known and used, their application to high-power WPT systems for electric vehicles has not yet been thoroughly discussed in this form in the literature. The approach presented in this paper is not limited to the specific WPT model discussed but rather is directly applicable to other WPT models as well.

Keywords:

Coupledproblems, Foreign object detection, Model order reduction, Thermal analysis, Wireless power transfer

Published in COMPEL - The international journal for computation and mathematics in electrical and electronic engineering, Vol. 42 No. 5, 2023, ISSN 0332-1649, page 1187 - 1198

Target classification using radar cross-section statistics of millimeter-wave scattering

Coskun Aysu,Bilicz Sándor

Department of Broadband Infocommunications and Electromagnetic Theory, Faculty of Electrical Engineering and Informatics, Budapest University of Technology and Economics, Budapest, Hungary

Purpose:

This paper aims to discuss the classification of targets based on their radar cross-section (RCS). The wavelength, the dimensions of the targets and the distance from the antenna are in the order of 1mm, 1m and 10m, respectively.

Design/methodology/approach:

The near-field RCS is considered, and the physical optics approximation is used for its numerical calculation. To model real scenarios, the authors assume that the incident angle is a random variable within a narrow interval, and repeated observations of the RCS are made for its random realizations. Then, the histogram of the RCS is calculated from the samples. The authors use a nearest neighbor rule to classify conducting plates with different shapes based on their RCS histogram.

Findings:

This setup is considered as a simple model of traffic road sign classification by millimeter-wavelength radar. The performance and limitations of the algorithm are demonstrated through a set of representative numerical examples.

Originality/value:

The proposed method extends the existing tools by using near-field RCS histograms as target features to achieve a classification algorithm.

Keywords:

Classification, Histogram, Machine learning, Radar cross-section, Physical optics

Published in COMPEL - The international journal for computation and mathematics in electrical and electronic engineering, Vol. 42 No. 5, 2023, ISSN 0332-1649, page 1199 - 1211

Feasibility study of eigenmode propagation through 2D models of vegetation

Csernyava Olivér (1),Pávó József (1),Badics Zsolt (1,2)

(1) Department of Broadband Infocommunications and Electromagnetic Theory (HVT), Faculty of Electrical Engineering and Informatics, Budapest University of Technology and Economics, Budapest, Hungary;
(2)Tensor Research LLC, Andover, Massachusetts, USA

Purpose:

This study aims to model and investigate low-loss wave-propagation modes across random media. The objective is to achieve better channel properties for applying radio links through random vegetation (e.g. forest) using a beamforming approach. Thus, obtaining the link between the statistical parameters of the media and the channel properties.

Design/methodology/approach:

A beamforming approach is used to obtain low-loss propagation across random media constructed of long cylinders, i.e. a simplified two dimensional (2D) model of agroforests. The statistical properties of the eigenmode radio wave propagation are studied following a Monte Carlo method. An error quantity is defined to represent the robustness of an eigenmode, and it is shown that it follows a known Lognormal statistical distribution, thereby providing a base for further statistical investigations.

Findings:

In this study, it is shown that radio wave propagation eigenmodes exist based on a mathematical model. The algorithm presented can find such modes of propagation that are less affected by the statistical variation of the media than the regular beams used in radio wave communication techniques. It is illustrated that a sufficiently chosen eigenmode waveform is not significantly perturbed by the natural variation of the tree trunk diameters.

Originality/value:

As a new approach to obtain low-loss propagation in random media at microwave frequencies, the presented mathematical model can calculate scattering-free wave-propagation eigenmodes. A robustness quantity is defined for a specific eigenmode, considering a 2D simplified statistical forest example. This new robustness quantity is useful for performing computationally low-cost optimization problems to find eigenmodes for more complex vegetation models.

Keywords:

Erroranalysis, Electromagnetic fields, Wave propagation, Electromagnetic waves, Field analysis, Computational electromagnetics

Published in COMPEL - The international journal for computation and mathematics in electrical and electronic engineering, Vol. 42 No. 5, 2023, ISSN 0332-1649, page 1212 - 1224

Index of Authors